METHODS FOR MONITORING AND FORECASTING VOLCANIC HAZARDS AND ERUPTIONS USING SEISMOLOGY AND OTHER GEOPHYSICAL DATA

A

THESIS

Presented to the Faculty

of the University of Alaska Fairbanks

in Partial Fulfillment of the Requirements

for the Degree of

DOCTOR OF PHILOSOPHY

By

Nicole DeRoin, B.S.

Fairbanks, Alaska

December 2012

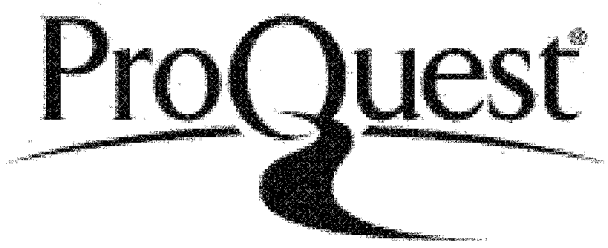

ProQuest LLC
789 East Eisenhower Parkway
P.O. Box 1346
Ann Arbor, MI 48106-1346

METHODS FOR MONITORING AND FORECASTING VOLCANIC HAZARDS AND ERUPTIONS USING SEISMOLOGY AND OTHER GEOPHYSICAL DATA

By

Nicole DeRoin

RECOMMENDED:

Advisory Committee Chair

Chair, Department of Geology and Geophysics

APPROVED:

Dean, College of Natural Science and Mathematics

Dean of the Graduate School

11/29/2012

Date

Abstract

Recent eruptions of three Alaskan volcanoes have provided the opportunity to study the relationships between seismicity and volcanic hazards and other phenomena. The ability to forecast or track volcanic activity through seismicity is important because seismic monitoring can be done in real time, 24 hours a day, regardless of weather, dangerous conditions or distance. To this end, the eruptions of Veniaminof in 2005, Augustine Volcano in 2006, and Redoubt Volcano in 2009, have been studied with the focus on understanding how seismic recordings and measurements are related to physical characteristics of eruption phenomena. Positive correlations were seen in relationships between ash plume heights at Veniaminof and their accompanying seismic magnitudes, and sizes and directions of rockfalls and block-and-ash flows at Augustine with seismic amplitude ratios and magnitudes. The relationship of rockfall occurrences in background years was also correlated with seasons and weather patterns, making easier the identification of rockfall increases that may be eruption precursors. Volcanic tremor, which frequently occurs accompanying volcanic eruptions, is studied during the Redoubt eruption, through the generation of duration-amplitude plots, and the potential for a new forecasting or monitoring tool is discussed.

Table of Contents

Page

List of Figures

Page

List of Tables

Page

List of Appendices

Page

Acknowledgments

I would first like to thank my advisor, Steve McNutt, for all the guidance he has given me in my time at UAF. I would also like to thank my committee members, Jeff Freymueller, Doug Christensen, and Mike West for their comments and advice on my thesis and my co-authors for their reviews and comments that helped shaped the papers in this thesis. I would also like to thank GI/UAF stuff, especially Scott Stihler for all the help with earthquake locating and X-pick and Mitch Robinson for the computer help, and Ed Clark for all the encouragement and support he has given over the years in the office and in the field. I would also like to thank my fellow students for all the help and encouragement they have given me over the years, and of course my family for all the support they have given. This work would not have been possible without financial support from the Alaska Volcano Observatory and the University of Alaska Fairbanks.

Chapter 1

Introduction

Volcanoes and volcano-related hazards pose numerous threats to people, property, and aircraft. Currently there are 1500 active volcanoes around the world, 222 of which are in densely populated areas (Small and Naumann, 2001). Volcanic hazards include eruption columns, landslides and rockfalls, pyroclastic flows, lahars, lava flows, ash clouds, gases, and acid rain. Although nothing can be done to prevent eruptions and other volcanic hazards from occurring, monitoring volcanoes can help to provide warnings, allowing people to evacuate or avoid dangerous areas. Volcano observatories around the world exist to monitor and study volcanoes in order to provide warnings and notifications of volcanic activity and to further the understanding of volcanic processes and mechanisms. Volcanology is a multi-disciplinary field that makes use of seismic, geodetic, radar, infrasonic, geologic, gas, meteorological, hydrological, satellite, and other data. By providing insight into a volcano's activity patterns (such as earthquake, rockfall or tremor occurrence, steaming, inflation, etc.) before, during and after an eruption, long term monitoring of volcanoes helps to establish activity patterns of the volcanoes, improving the accuracy of eruption forecasting.

The primary subject of this thesis is volcano seismology, and its use in forecasting and tracking volcanic phenomena and activity. Volcano seismology is the study of earthquakes, or other seismic phenomena, occurring at or near

volcanoes. Many eruptions are preceded by an increase in the number of earthquakes or earthquake swarms. While sometimes the earthquakes are large enough in magnitude to be felt by people nearby, in most cases they are very small magnitude earthquakes. One type of volcanic earthquake is high-frequency, or volcano-tectonic earthquakes, which are thought to be caused by shear failure similar to tectonic earthquakes (e.g. Latter, 1980), and which also usually occur at volcanoes in swarms (Benoit and McNutt, 1996). Low-frequency earthquakes also occur frequently at volcanoes and hydrothermal areas, have dominant frequencies between 1-5 Hz, and are thought to be caused by processes including bubble growth and collapse or vibration of fluid-filled cracks (Chouet, 1996). Volcanic tremor is another low-frequency seismic signal, that may be caused by movement of magma or fluids through pipes (Chouet, 1985) or cracks (Aki et al. 1997, Chouet 1986, 1992). Other seismic signals are also caused by volcanic phenomena such as eruptions, explosions, rockfalls, lahars, pyroclastic flows, and phreatic eruptions.

This thesis is concerned with volcanic hazard monitoring and tracking volcanic eruptions through seismicity. Several types of seismic signals, including low-frequency explosion earthquakes, rockfall-related seismicity and volcanic tremor, are considered along with their relation to volcanic phenomena. Because seismic data obtained from a remote volcano can be telemetered to observatories, volcanoes can be distantly monitored in real and near-real time. This is an advantage when visual observations are not possible, due to distance or poor visibility conditions. However, utilizing data and observations from multiple disciplines is

often more useful than relying on only one type of observation. A seismic recording of an earthquake swarm at a volcano may not necessarily signal an imminent eruption. Detection of a thermal anomaly at the surface of that same volcano, combined with geodetic measurements that show inflation at the summit, in addition to the same earthquake swarm is more telling. When visual observations of a volcano can be made in conjunction with seismic data, opportunities to improve seismic tracking of volcanoes also improve. If measurements of volcanic hazards such as rockfalls or ash explosions can be measured independently and correlated with seismicity, then more accurate assessments of these phenomena through seismicity can be made in times when no visual observations are possible. To this end, two chapters of this thesis are on the topic of comparing seismic measurements with visual observations of volcanic activity. Chapter 2 discusses the 2005 eruption of Veniaminof Volcano, during which numerous ash explosions occurred. The ash plumes were all accompanied by low-frequency earthquakes which were recorded on seismic stations. The heights of the ash plumes were compared with seismic amplitudes and magnitudes and a positive correlation was shown to exist. In Chapters 3 and 4, the 2006 eruption of Augustine Volcano is discussed. Numerous rockfalls and block-and-ash flows occurred during this eruption and were recorded on seismic stations. Precursory rockfalls and the effect of weather and seasons on their occurrence are discussed in Chapter 3. In Chapter 4, the seismicity of block-and-ash flows that occurred during the eruption, and were recorded on a low-light camera, are discussed. The direction of travel of the block-and-ash flows is

compared with seismic amplitude ratios and estimated sizes of the flows are compared with the amplitudes of the seismic signals they produced.

In Chapters 5 and 6, volcanic tremor and reduced displacement measurements are discussed. Chapter 5 is a short discussion on reduced displacement measurements and the effect that station distance to the vent can have within a volcanic network. In Chapter 6 the 2009 eruption of Redoubt is studied. The duration-amplitude distribution of the volcanic tremor that Redoubt exhibited during this eruption was analyzed and found to obey an exponential law, while periods of non-activity are better fit using a power law. This result has potential for volcano monitoring. Characteristic amplitudes of the various tremor episodes were analyzed and compared with volcanic activity and compared with ash column heights (measured by others independently during eruption response) and showed a positive correlation. The conclusions drawn from the chapters in this thesis add to previous observations in the field of volcano seismology, including those of seismic measurements of rockfalls and pyroclastic flows, and duration-amplitudes of volcanic tremor.

1.1. References

Aki, K., Fehler, M., Das, S., 1977. Source mechanism of volcanic tremor: Fluid driven crack models and their application to the 1963 Kilauea eruption. Journal of Volcanology and Geothermal Research, 2, p. 259-287.

Benoit, J.P., McNutt, S.R., 1996. Global volcanic earthquake swarm database and prelimary analysis of volcanic earthquake swarm duration. Annali Di Geofisica, 39, p. 221-229.

Chouet, B., 1985. Excitation of a buried magmatic pipe: A seismic source model for volcanic tremor. Journal of Geophysical Research, 90, p. 1881-1893.

Chouet, B., 1986. Dynamics of a fluid-driven crack in three dimensions by the finite difference method. Journal of Geophysical Research, 91, p. 13,967-13,992.

Chouet, B., 1992. A seismic model for the source of long-period events and harmonic tremor. In: P. Gasparini, R. Scarpa and K. Aki (Editors), Volcanic Seismology. IAVCEI Proc. In Volcanology, Springer-Verlag, Berlin, 3, p. 133-156.

Chouet, B., 1996. Long-period seismicity: its source and use in eruption forecasting. Nature, 380, p. 309-316.

Latter, J.H., 1980. Volcanic earthquakes, and their relationship to eruptions at Ruapehu and Ngauruhoe volcanoes. Journal of Volcanology and Geothermal Research, 9, p. 293-309.

Small, C., Naumann, T., 2001. The global distribution of human population and recent volcanism. Global Environmental Change Part B: Environmental Hazards, 3, p. 93-109.

Chapter 2

Ash Plumes and Accompanying Seismicity at Veniaminof Volcano, Alaska, 2005[1]

Abstract

Mount Veniaminof, Alaska, erupted from January-February 2005. During the eruption, the volcano was monitored by a seismic network and a web camera. The early phase of the eruption was characterized seismically by the occurrence of many low frequency (LF) earthquakes. These LF events were almost always accompanied by frequent small ash bursts. Comparison of seismic event magnitude and plume height, estimated from webcam images, shows that the heights of the ash plumes correlate with event magnitude. Theoretical plume heights are also calculated for comparison, using the seismic energies obtained from the magnitudes of the discrete LF events and compared with observed heights. The seismic energy release for the seismic events is calculated, and from this, the kinetic energy of the erupted ash is estimated. Heights of the plumes were then estimated using the calculated energies, and assuming a constant energy ratio. The estimated values show a general agreement with the observed plume heights. Estimated velocities for the ejected ash range from 93 m/s to 209 m/s.

---

[1] DeRoin, N. and McNutt, S.R. 2012. Ash Plumes and Accompanying Seismicity at Veniaminof Volcano, Alaska, 2005. Prepared for submission.

2.1. Introduction

2.1.1. Ash plumes and VEI

Ash clouds or columns typically accompany volcanic eruptions at stratovolcanoes. These clouds, which can pose a danger to aircraft, are composed of rock fragments, glass, gases and ash. Webcam monitoring is helpful in observing ash eruptions, but ash plumes may not always be visible due to poor weather or darkness. Because ash clouds are usually accompanied by some type of seismic activity, such as explosion earthquakes or tremor, seismic monitoring can be useful for monitoring ash eruptions, even when webcam monitoring is not, by detecting when seismic events that are likely to produce ash bursts are occurring. Hazard monitoring of volcanoes can be improved if ash cloud heights can be correlated with seismic data. Heights of volcanic ash plumes have already been correlated with the intensity of volcanic eruption. For example, volcanic explosivity index (VEI) rankings are often determined by plume heights. VEI is a rating of the intensity of volcanic eruptions, and takes into account ash column heights, erupted tephra volume, and other factors in assigning a number of 0 – 8 to volcanic eruptions (Newhall and Self, 1982). Eruption columns and ash plumes are usually accompanied by some type of seismic signal, such as tremor or explosion earthquakes. McNutt (1994) showed a linear correlation between maximum tremor reduced displacements (D_R) and VEI. Reduced displacement is a measure of tremor amplitude that has been corrected for geometrical spreading, for comparison between different volcanoes. These studies, however, only compared the maximum D_R of the

entire eruption with the maximum plume heights or VEI, using one data pair per eruption. In this study of the 2005 eruption of Veniaminof, heights of numerous individual ash plumes as seen on a webcam are compared with the seismic magnitudes of the explosion earthquakes that produced/ directly preceded them. The high number of events provides a useful demonstration of the variance inherent in such data sets.

2.1.2. Activity and monitoring

Mt. Veniaminof (56.1979°N, 159.3931°W) is a 2507 m stratovolcano in the Alaska Peninsula (fig. 2.1). Veniaminof typically demonstrates Strombolian volcanic activity. It has erupted several times since 2000, the most recent periods of eruptive activity occurring during January to February 2005, September to November 2005, March to September 2006, and February 22, 2008. The eruption occurring from January to February 2005 is the focus of this study. During the 2005 eruption, Veniaminof was monitored by 8 short period (T=1s) vertical component seismic stations. Seismograms recorded continuous volcanic tremor, beginning January 1, 2005 and lasting until the end of February 2005, (McGimsey et al., 2007; DeAngelis and McNutt, 2007). A web camera located in Perryville (35 km southeast from the summit; fig. 2.1) also monitored the volcano during the eruption. Low-level ash bursts were seen frequently in the web camera. Discrete seismic events virtually always accompanied the ash explosions.

An eruption timeline with the associated AVO color codes is shown in Figure

2.2. The color code was first raised from green (background) to yellow after ash bursts were observed on January 4, 2005, and corresponding continuous tremor was noted in the seismic data. On January 10 the color code was upgraded to orange after two days of continuous ash emissions occurred. Ash emissions and low-amplitude tremor continued through the rest of January (McGimsey et al., 2007). The seismicity decreased in the week of February 25, and the color code was returned to yellow. By the following week, in March, the seismic activity had returned to background levels (McGimsey et al., 2007), and the color code was changed to green.

2.2. Data, methods and results

2.2.1. Ash plume heights and seismic magnitudes

Along with continuous volcanic tremor that lasted throughout most of the eruption, numerous discrete earthquakes occurred as well. Figure 2.3 is an example of the types of events that accompanied the ash bursts. The events have small magnitudes, short durations, and low frequencies (LF). At peak times, up to ~100 events occurred per hour (fig. 2.3). Seismic amplitudes of the low-frequency events were measured at the closest station VNSS. Magnitudes were then calculated using the program HYPOELLIPSE (Lahr, 1999), by fixing the location at the active vent. Daily plots of the earthquakes' maximum peak-to-peak (p-p) amplitude, the maximum tremor duration for that day, the number of events with zero-to-peak amplitude of 2.5 mm or higher (measured from paper helicorder records), and the

maximum reduced displacement in cm^2 are shown in figure 2.4. These were determined from standard scale plots used for routine monitoring. Conversion to physical units was accomplished separately. Note the increase in both the maximum tremor duration and number of larger events (figs. 2.4B and C) that occurred on the 41^{st} day of the eruption.

The webcam in Perryville recorded images of Veniaminof's summit every five minutes. Figure 2.5 shows examples of web camera images and spectra of the accompanying earthquakes. Dominant frequencies of the seismic signals were usually between 1 and 3 Hz, with some exceptions. Hundreds of plumes were recorded on the web camera images. However, cloudy weather also obscured many views of the summit and likely ash plumes. Windy conditions also frequently made measurements of plume heights difficult or impossible (see fig. 2.6, for example). Enough clear and calm days occurred, however, that a sufficient number of plume heights could be estimated. Plume heights were measured from the images using a ruler and triangulation (using height of volcano and its measurement on the image at a given distance from the camera.) A web camera image of a plume with an independently measured height was also used for comparison. Figure 2.7 shows a plot of the plume heights and magnitudes. Although some scatter exists, the plume heights show positive correlation with seismic magnitudes. The r^2 value of 0.3 is within the 5% significance level for a sample size of 109 data points.

2.2.2. Calculated energies

Theoretical plume heights based on the seismic events were also calculated and compared with the observed plume heights, using seismic energies. Seismic energies are obtained using the Gutenberg-Richter equation (Richter, 1958) for local magnitudes (M_L).

$$(1) \quad \text{Log } E = 9.9+1.9M_L-0.0024M_L^2$$

Only a fraction of the energy released by the earthquake goes into creating an explosion. Energy is dispersed as seismic waves and infrasonic waves (low frequency sound). Significant energy goes into creating the explosion or is lost as heat. A typical seismic efficiency for explosions is 1% of the energy released by the explosion event (Richter, 1958). Therefore, the explosion energy, E_e, determined from the seismic energy E_s is assumed to be:

$$(2) \quad E_e = 100*E_s$$

These estimates are suitable for the current data set because all events occurred at the same place (the vent), produced similar seismic signatures, and were recorded at the same station.

2.2.3. Theoretical plume heights

To estimate plume heights, it is important to consider plume dynamics. Eruption columns can be considered to be composed of two parts. The first is the gas jet region, in which high particle velocities are present and in which momentum and kinetic energy predominantly controls particle motions (Sparks, 1986). This occurs in the first few hundred meters of plume height. The ash-gas mixture that is erupted can be modeled as a "projected slug" (Wilson et al., 1978). The second part is the convective zone, in which buoyancy dominates (Sparks, 1986). Because the plumes at Veniaminof are small, they are assumed to occur only in the gas-jet region. Therefore only kinetic energies (and not convection dynamics) need to be considered. The explosions are also assumed to be instantaneous explosions, which supply material to the plume for only a short time (as opposed to a maintained plume, in which material is continuously supplied to the plume), so that each plume is attributed to one explosion. Estimates of plume masses (~100 kg) for Stromboli were obtained from the study by Patrick (2005) which used FLIR imagery to obtain mass of ash bursts. Veniaminof displays similar eruption style as Stromboli, i.e., small, frequent explosions, usually accompanied by low frequency earthquakes. The masses quoted in Patrick (2005) were used as a starting point; larger masses (such as ~300kg - 1000 kg) were found to fit the observed data better.

Wind resistance and friction between ash particles are ignored and the kinetic energy at the source of the explosion is assumed to be equal to the potential energy at the top of the plume. Therefore the height, h, of the plume (m) can be estimated as:

$$(3) \qquad h = \frac{E_e}{mg}$$

where m is the mass (kg) and g is acceleration due to gravity, and E_e is the potential energy (J). This assumes all mass is at the top of the plume. Velocities (v) are estimated by the following equation:

$$(4) \qquad v = \sqrt{2\frac{E_e}{m}}$$

The estimated plume heights for various estimated masses of plumes are shown in figure 2.8. The observed plume heights are plotted on the figure as well and fit within boundaries made with the kinetic energy-derived plume heights, although the results suggest that higher magnitude seismic events may have larger masses. Finally, average calculated ejecta velocities range from 93 m/s to 209 m/s (for the 1000 kg and 200 kg estimated masses, respectively). These velocities agree with the initial rising velocities given by Sparks (1986).

2.2.4. Reduced displacement and plume heights

Typical magnitudes for the explosion earthquakes were around 1. This corresponds to a reduced displacement of 2.2 cm^2. In McNutt (2005), VEI estimates were compared with D_R measurements for 50 eruptions occurring at 31 volcanoes, showing that volcanic explosivity is related to tremor amplitude. Heights of the

Veniaminof plumes were all less than 5 km, corresponding to VEI 1 (plume heights of 100 m to 1000 m) and VEI 2 (plume heights 2-5 km). The corresponding D_R measurement ranges were entered into the plot made by McNutt (2005), shown here as figure 2.10. These data entries are in the lower range of values, but still within the typical range of values.

2.3. Discussion

Heights of ash plumes at Veniaminof show a positive correlation with the seismic amplitudes and magnitudes of the explosion earthquakes that accompanied them. Although conditions were not perfect for performing this study, the large number of observations that were able to be made partially outweighs this disadvantage. The low (but still statistically significant) correlation coefficient is probably due to factors such as low sampling rate of the camera, and errors in estimating heights due to windy conditions. Ideally, plumes would be measured at their peak heights after eruption, however, in the web camera images it is unclear whether the plumes reached their maximum height at the time of measurement. Wind shear will affect the plumes' apparent height as well, by distorting them from the 'vertical' as seen in the images. These factors have likely contributed a good deal of scatter to the data, as seen by the relatively low r^2 value of 0.3 for figure 2.7. The value of this project, however, is the robust sampling due to the high number of observations that were able to be made.

Different source processes may influence scatter in the data as well. For example, one cluster of events having low magnitudes and high plume height particularly distorts the otherwise more linear correlation (seen in figure 2.7 as the data points marked with 'x'). As seen in figure 2.9, these events are associated with seismicity similar to gliding tremor. These events all occurred within one hour (beginning ~13:00 AKST) on January 9, 2005. The events had longer durations but lower magnitudes than other events in the eruption sequence, which may contribute to higher plume heights (or perhaps just higher volume of ash) than other plumes with similar magnitudes, but shorter durations.

Using estimated kinetic energies of the explosion events showed that the Veniaminof plumes are small enough to be modeled in the gas thrust region by kinetic energy calculations; it is not necessary to consider convection. The scatter of data compared with modelling suggests different amounts of ash are erupted in different explosions. Finally, the reduced displacement and VEI for the 2005 eruption of Veniaminof fit within the error limits in the DR versus VEI plot ranges determined previously.

2.4. Conclusions

Understanding the relationships between seismicity and volcanic hazards is useful for monitoring purposes, especially during times when visual observations are not available but seismic data, which can be monitored remotely, is recorded. The 2005 eruption of Veniaminof provided a good opportunity to study the relationships

of plume heights to seismic magnitudes of explosion earthquakes, because of the hundreds of ash plumes and explosion earthquakes that occurred and were recorded on both webcam and seismic data. Plume heights and seismic magnitudes were compared and show a positive correlation. Further understanding of the nature of the Veniaminof plumes is found from using seismic energies to calculate theoretical plume heights, which showed that the plumes of this eruption can be considered as mainly functions of kinetic energy (gas thrust), without considering the effects of convection. While a study such as this would be improved by a webcam with a higher sampling rate, the large number of observations that were made offsets some of the error introduced by the low sampling rate of the web camera.

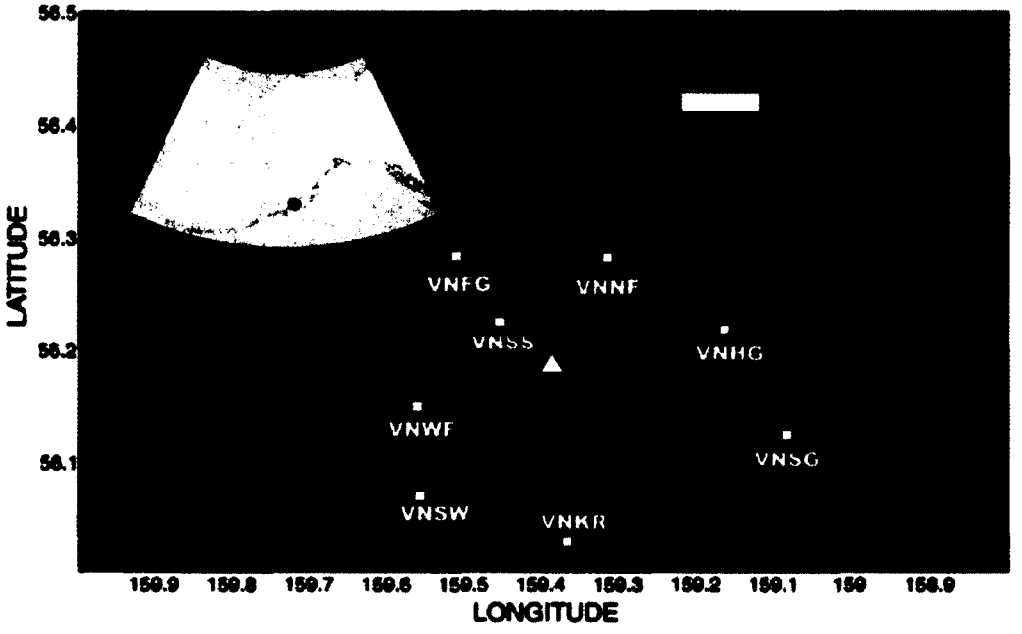

Figure 2.1

Index map of Veniaminof and its monitoring stations. The seismic stations are all short period (1s) single component vertical seismic stations, which are telemetered and digitized at the seismology laboratory in Fairbanks, Alaska. The triangle shows the vent. The arrow points towards Perryville. The seismic data for this study were recorded on station VNSS. The inset shows the location of Veniaminof on the Alaska peninsula, in south Alaska. Digital base map from the SRTM digital elevation model courtesy NASA/JPL.

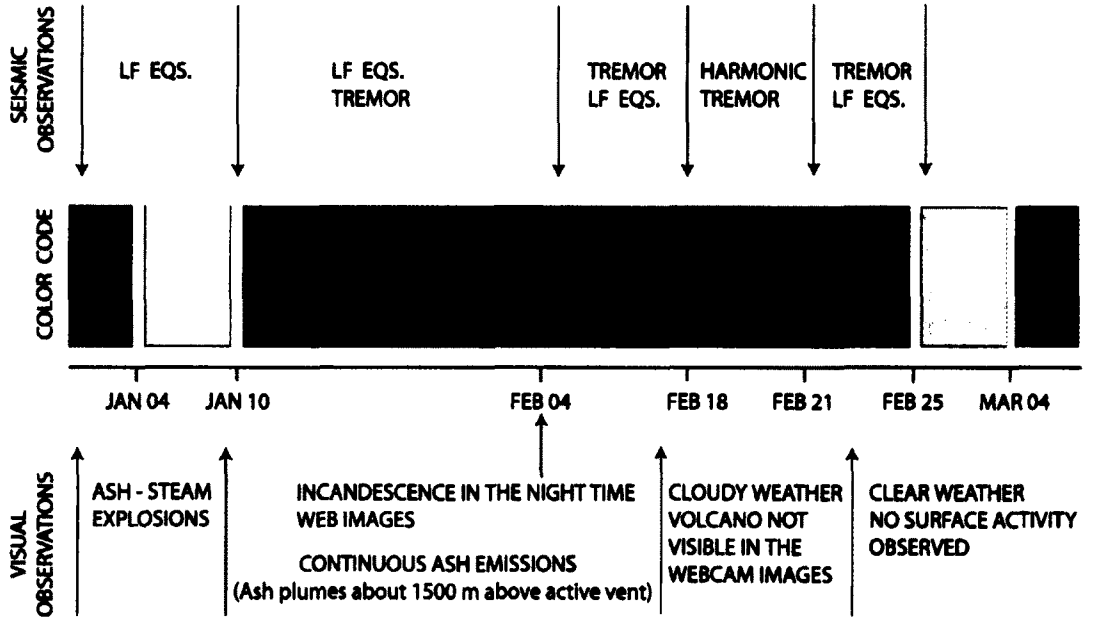

Figure 2.2

Chronology of Veniaminof eruption showing color code changes. Seismic and visual observations typical of each period are also shown. Most of the data used in this study came from early January, i.e., January 9, when the ash-steam explosions were occurring discretely, before the continuous ash emission phase began. Note that "LF" stands for low frequency, and "EQS" is an abbreviation for earthquakes. Figure from DeAngelis and McNutt (2005).

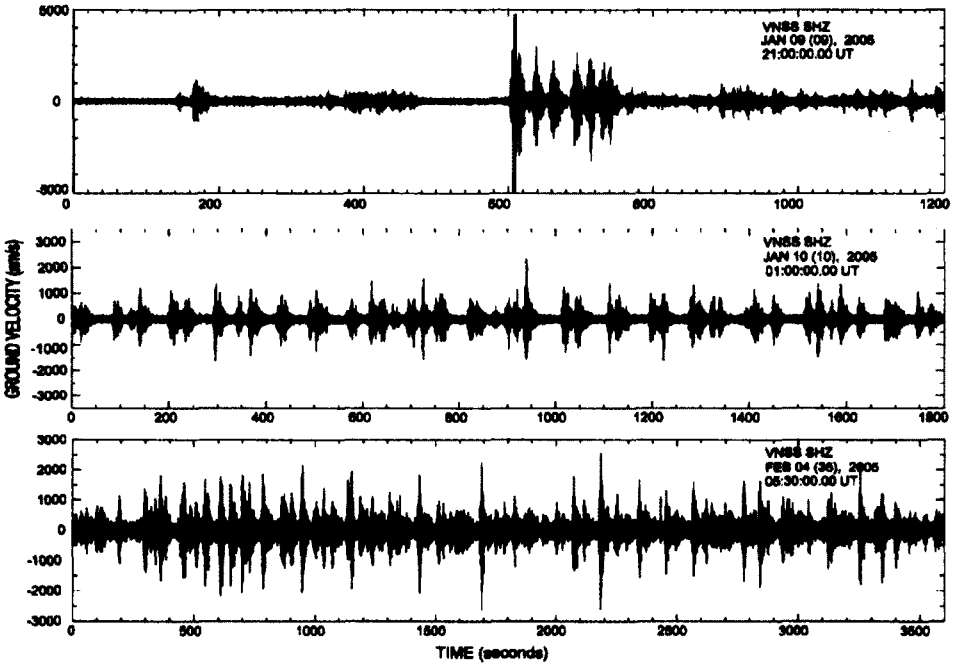

Figure 2.3

Examples of LF earthquake swarms at Veniaminof. These swarms have durations varying from tens of minutes to many hours recorded. The amplitudes and occurrence rates of LF events increased over the month of January, and correlated with surface activity that evolved from discrete and relatively small ash explosions into more continuous emissions forming ash plumes. Note the differences in time and amplitude scales for each plot. Figure from DeAngelis and McNutt (2005).

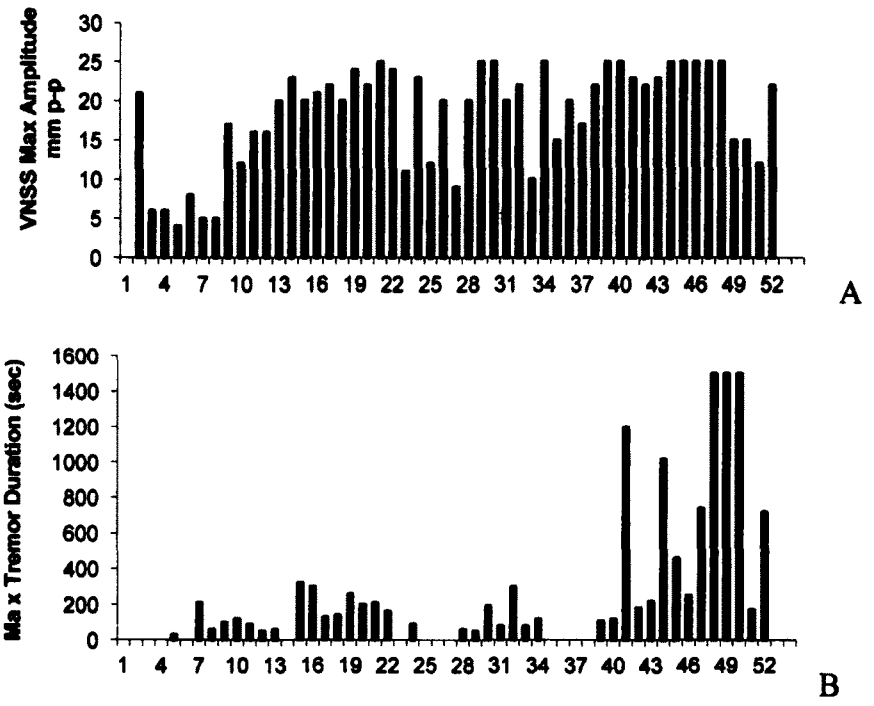

Figure 2.4

Daily counts of explosion earthquakes. The plots show A) the earthquakes' maximum peak-to-peak (p-p) amplitude in mm, B) the maximum tremor duration for that day, C) the number of events with zero-to-peak amplitude of 2.5 mm (measured from paper helicorder record), and D) the maximum reduced displacement (DR) in cm^2. Note that a DR of 2.2 cm^2 corresponds to a magnitude of 1.0. The displacement and duration measurements were made from helicorder records from station VNSS.

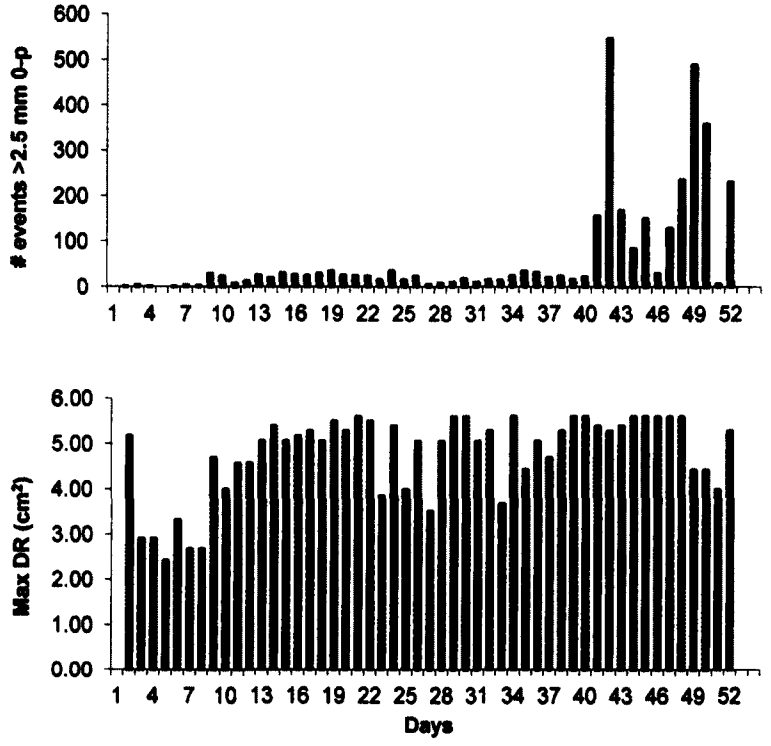

Figure 2.4 continued

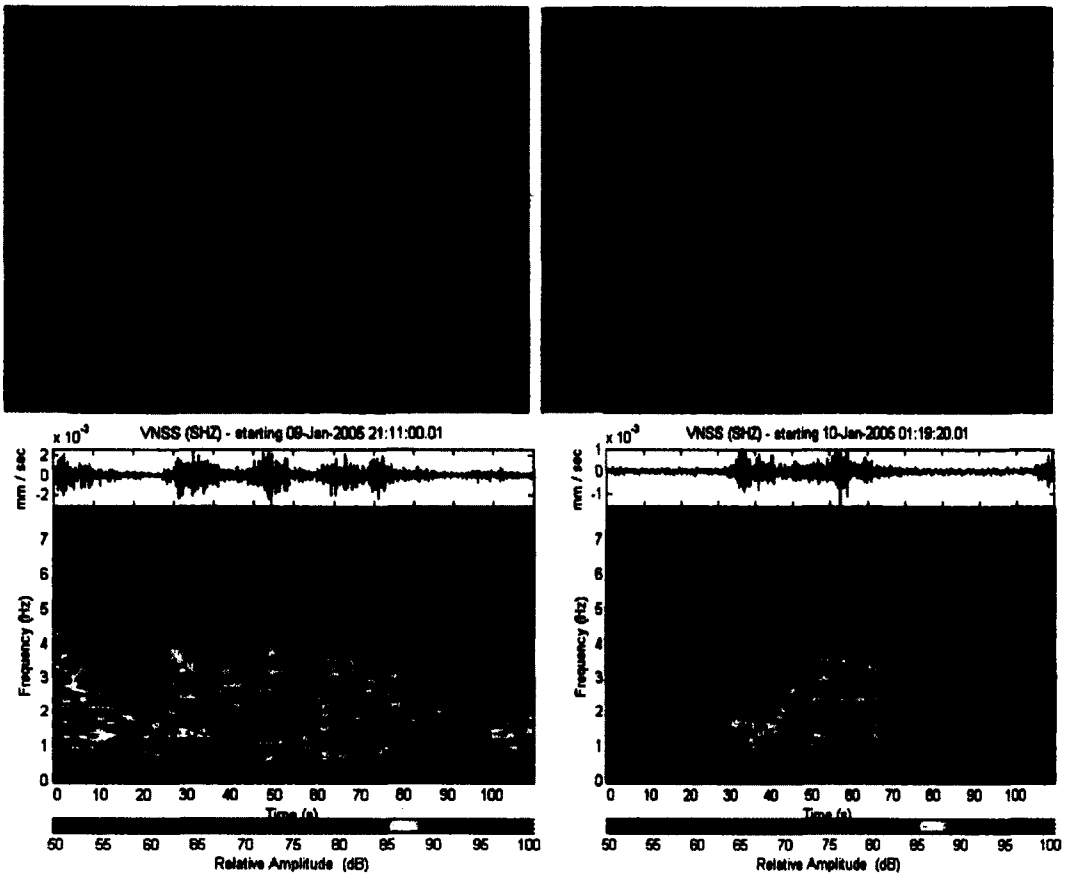

Figure 2.5

Example plume images and spectrograms of corresponding seismic event. The top left plume was measured to have a height of 1.8 km, and the plume height for the top right figure was measured to be 1.2 km. Note that the webcam images are in Alaska standard time, while the spectrograms are in UT. The first image has an offset time of 220 seconds from earthquake to plume image, the second has an offset time of 180 seconds.

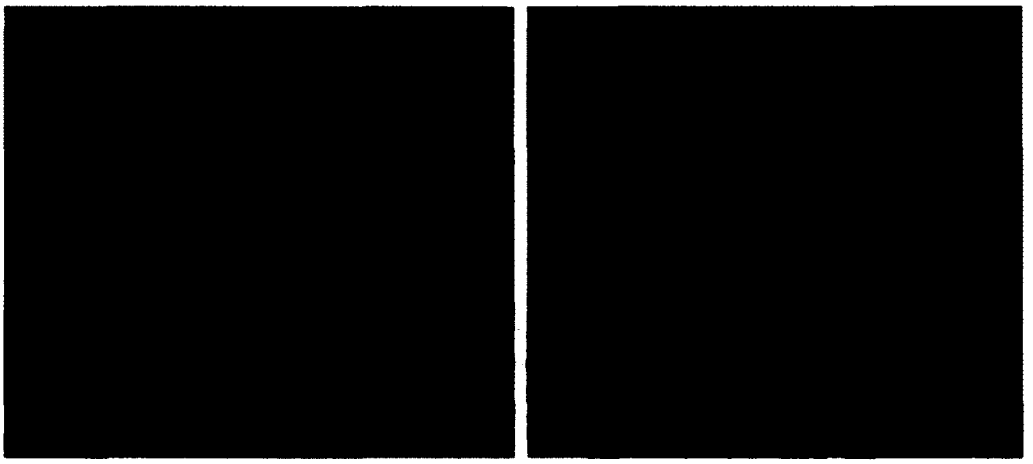

Figure 2.6

Images showing error sources in plume height measurements. A) shows the plume being blown to the west by wind so that a height measurement cannot be accurately made. B) shows the image of a particular plume that has most likely not yet reached its maximum height. Due to the camera's low sampling rate (1 image per 5 minutes), this is the only available image of this plume. Plumes as seen in the left were usually not included in the study cases, but plumes such as the right figure were included, because they are difficult to distinguish from smaller explosions.

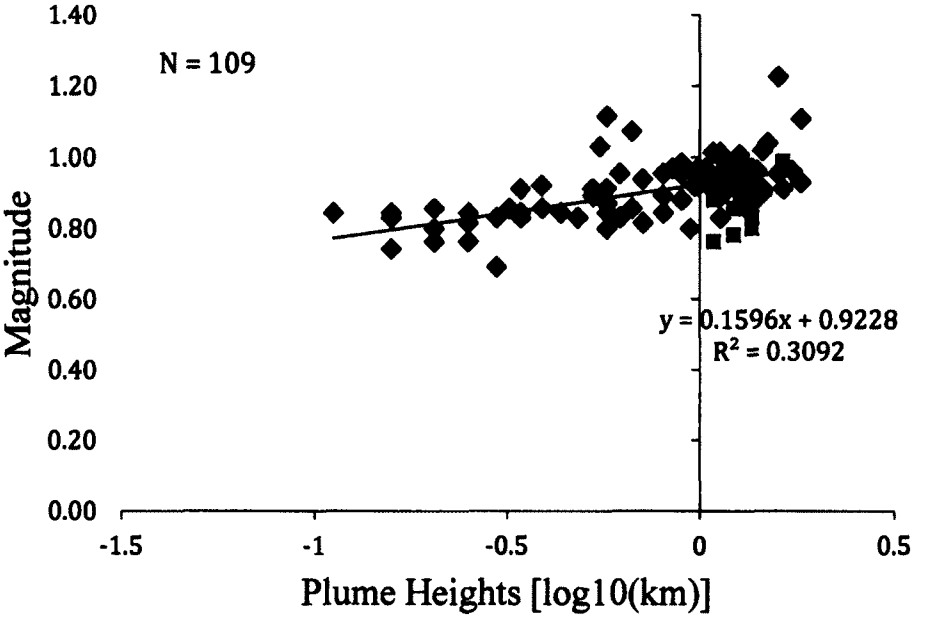

Figure 2.7

Magnitude of explosion earthquakes vs. observed plume heights. The plot shows a linear correlation with an r^2 value of .3, which is significant for a plot with 109 data points. Scatter can be attributed to the low sample rate of the web camera, wind shear may also be a factor, and the two-dimensional nature of the height measurements. One section of data points, indicated by the markers with an "x", which occurred ~13:00-14:00 AKST January 9, may be attributed to a different mechanism. These data points come from an episode of near continuous ash emissions which were associated with gliding tremor (see fig. 2.9), as opposed to discrete earthquakes. The earthquakes occurring at this time had longer durations, which may contribute to higher plume heights than those produced by earthquakes with similar amplitudes but shorter durations.

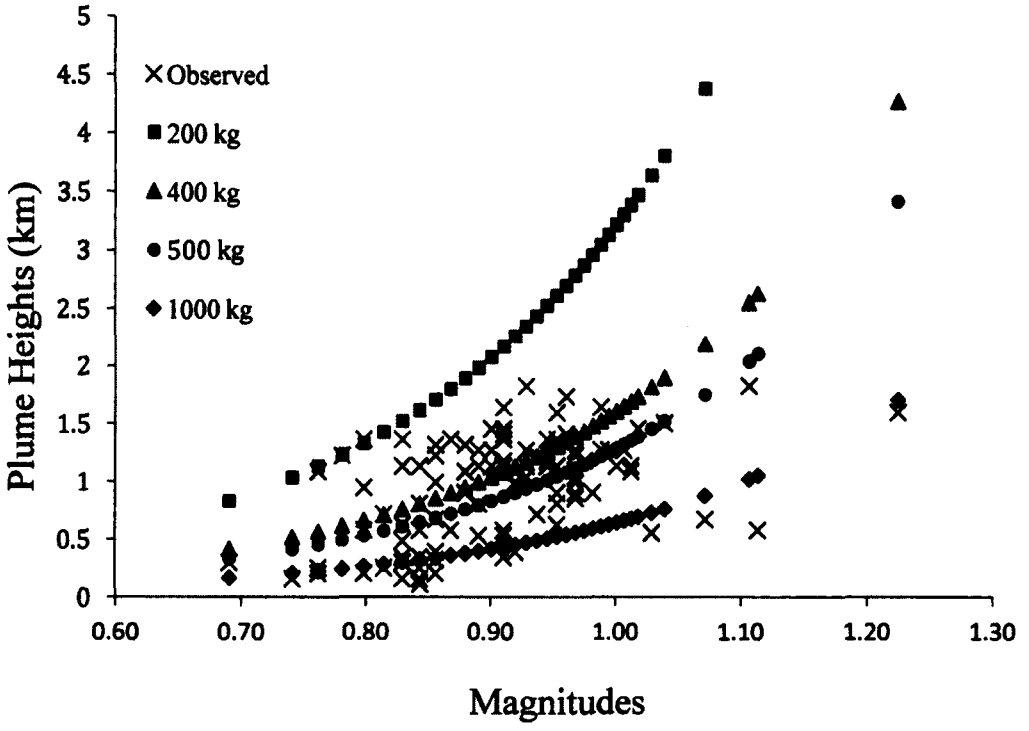

Figure 2.8

Estimated plume heights for different masses using energy calculations. The observed plumes fit within the boundaries made by choosing masses between 200 kg and 1000 kg. This result suggests that it is appropriate to model them as functions of kinetic energy, without considering the effects of convection or buoyancy. The results suggest that higher magnitude seismic events may have larger masses. Estimated velocities (initial velocities from vent) based on the same energies used to calculate plume heights range between 93 m/s (average for 1000 kg masses) to 209 m/s (for 200 kg masses).

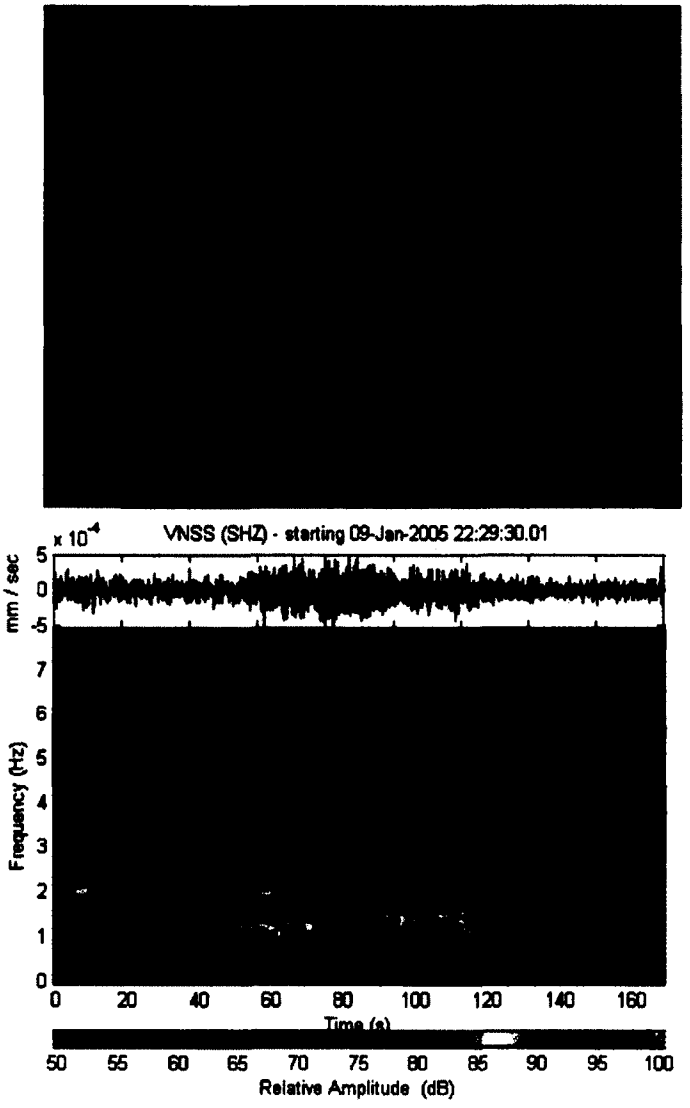

Figure 2.9

Example of gliding tremor and webcam plume. This event is representative of a cluster of events that occurred for approximately 1 hour on January 09, 2005. The plumes were darker in color and more spread out, likely a sign of continuous ash emission. The corresponding seismicity had lower amplitudes and resembles tremor which appears to 'glide' to a higher frequency during the course of the event.

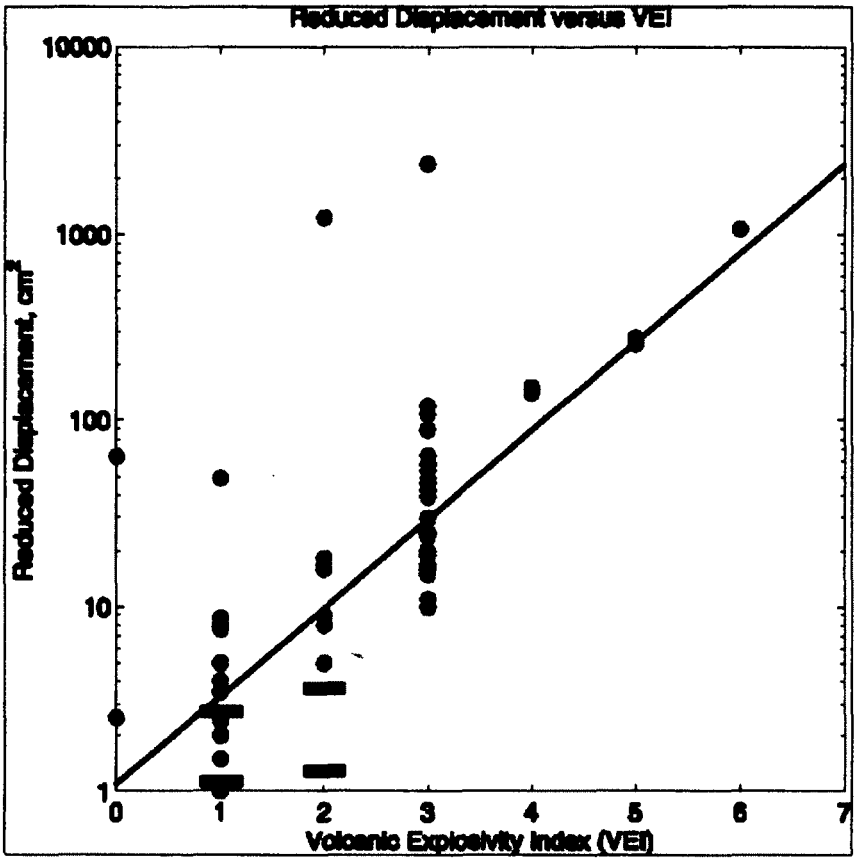

Figure 2.10

Reduced displacement vs. Volcanic Explosivity Index. This figure is modified from McNutt (2005), which was plotted from data from 50 eruptions and 31 volcanoes. It has been updated to include data from the 2005 eruption of Veniaminof. The red bars show ranges of reduced displacements for ash bursts at Veniaminof rated VEI 1 and 2, corresponding to plume heights of 100 m to 1000 m and 2-5 km, respectively. The Veniaminof data points are consistent with the variance range for VEI 1, but slightly lower than the VEI 2 range.

2.5. References

DeAngelis, S., McNutt, S.R., 2007. Observations of volcanic tremor during the January-February 2005 eruption of Mt. Veniaminof, Alaska. Bulletin of Volcanology, 69, p. 927-940.

DeAngelis, S., McNutt, S.R., 2005. Eruption and earthquake activity at Mt. Veniaminof, Alaska, during January-February 2005. American Geophysical Union, Fall Meeting 2005, abstract #V21C-0616.

Lahr, J.C., 1999. HYPOELLIPSE: A computer program for determining local earthquake hypocentral parameters, magnitude, and first motion pattern. U.S. Geological Survey Open-File Report 99-23, 116 p.

McGimsey, R.G., Neal, C.A., Dixon, J.P., Ushakov, S., 2007. 2005 Volcanic activity in Alaska, Kamchatka, and the Kurile Islands. Summary of events and response of the Alaska Volcano Observatory. U.S. Geological Survey Scientific Investigations Report 2007-5269, 94 p.

McNutt, S.R., 1994. Volcanic tremor amplitude correlated with eruption explosivity and its potential use in determining ash hazards to aviation. Volcanic Ash and Aviation Safety. U.S. Geological Survey Bulletin 2047, p. 377-385.

McNutt, S.R., 2005. A Review of Volcanic Seismology. Annual Reviews of Earth and Planetary Sciences, 33, p. 461-491.
doi: 10.1146/annurev.earth.33.092203.122459.

Newhall, C.G., Self, S., 1982. The volcanic explosivity index (VEI): an estimate of

explosive magnitude for historical volcanism. Journal of Geophysical Research, 87, p. 1231-1238.

Patrick, M., 2005. Strombolian eruption dynamics from thermal (FLIR) video imagery. University of Hawai'i at Manoa, 283 p.

Richter, C.F., 1958. Elementary Seismology: Freeman and Company, Inc., San Francisco. 768 p.

Sparks, R.S.J., 1986. The dimensions and dynamics of volcanic eruption columns. Bulletin of Volcanology, 48, 1, p. 3-15.

Wilson, L., Sparks, R.S.J., Huang, T.C., Watkins, N.D., 1978. The control of volcanic column heights by eruption energetics and dynamics. Journal of Geophysical Research, 83, B4, p. 1829-1835.

Chapter 3

Rockfalls at Augustine Volcano, Alaska: The Influence of Eruption Precursors and Seasonal Factors on Occurrence Patterns 1997-2009[2]

Abstract

Rockfalls have been recorded in seismic data at Augustine Volcano from 1997 to the present. Typical events last about 30 s and have frequencies >4 Hz on stations within 5 km of the summit. Many rockfalls are well recorded on summit seismic stations, suggesting that they originate from the steep summit dome. Typical background years such as 2003 or 2004 had several dozen events in the summer and fall (June to November) that were strong enough to trigger an automatic event detection system. For example, 17 rockfalls were recorded in 2003; mostly in late summer when air temperatures were warm and rainfall rates were highest, and 28 events were recorded in 2004, also in late summer. In 2005, about eight months before the onset of the eruption of Augustine in January 2006, there was a significant increase in the number of rockfalls detected. This increase of surface rockfall activity occurred at nearly the same time as precursory earthquake activity increased beneath Augustine. Overall there were more than 340 rockfalls in 2005, consisting of both short (less than 30 s) and long (greater than 30 s) duration events. The high

[2] DeRoin, N., and McNutt, S.R. 2011. Rockfalls at Augustine Volcano, Alaska: The Influence of Eruption Precursors and Seasonal Factors on Occurrence Patterns 1997-2009. Journal of Volcanology and Geothermal Research, 2011, 211-212, 61-75. http://dx.doi.org/10.1016/j.jvolgeores.2011.11.003

rate of rockfalls in 2005 constitutes a new class of precursory signal that needs to be incorporated into long-term monitoring strategies at Augustine and elsewhere. During the eruption, numerous rockfalls continued to occur, and block-and-ash flows dominated the seismic records when the volcano began a phase of dome growth and collapse. The high rates of rockfalls continued after the eruption ended, due to the new unstable lava dome and adjacent tephra at the summit. As of 2009 the rockfall rates are still high, but are declining steadily.

3.1. Introduction

Rockfalls and landslides are a common occurrence at many volcanoes around the world. The events may be small (single falling blocks), or very large avalanches. A scheme for classifying mass wasting events in general proposed by Sharpe (1938) includes slow-flowage and rapid flowage types, landslides and subsidence. Rockfalls, rockslides, debris falls and debris slides fall into the landslide category. Landslide movements are classified into five types by Varnes (1978): falls, topples, slides, spreads and flows. Within these types are further subdivisions, i.e., falling motions can include free-falling, bouncing, and rolling motions, and sliding movements can be mean rotational or translational sliding (Cruden and Varnes, 1996). Causes of landslides can be geologic (weak, sensitive, or weathered slope materials), morphological (tectonic or volcanic uplift, glacial rebound, deposition loading), physical (rainfall, snow melt, drawdown of tides, volcanic eruption, earthquake, thawing, freeze-and-thaw weathering, shrink-and-swell weathering) or

human (irrigation, deforestation, mining, excavation of slope, etc.) (Cruden and Varnes, 1996). Several of these factors may occur together to cause a landslide, however, only one trigger will exist which causes a landslide as a near-immediate response (Wieczorek, 1996). Triggers may be intense rainfall, rapid snowmelt, earthquake shaking, volcanic eruption, or water-level change (Wieczorek, 1996).

Seismic characterization of rockfalls is important for several reasons. Seismic monitoring of rockfalls can provide real-time hazard assessment at volcanoes. Seismic characterization of rockfalls can make it easier to distinguish them and remove them when monitoring other seismic activity (Surinach et al., 2005). Rockfalls can also be useful for monitoring volcanic activity, as sudden or gradual changes in their locations, sizes, or rates may be related to subsurface magma movements.

Rockfalls occur frequently at Augustine Volcano and occurred in high numbers before, during and after its eruption in 2006. Many of the rockfalls generated seismic signals large enough to trigger the automatic seismic event detection system (Johnson et al., 1995). Photographs of several smaller rockfalls at Augustine Volcano exist that show motion in the fall/rolling/bouncing category, but most of the rockfalls in this study were identified by the seismic signals they produced only, and not observed visually. For this reason, we refer to the events discussed here as rockfalls in general, except when it is known more specifically what type of event is occurring.

Rockfalls and flow events from four periods are studied in this paper. The first period (the background period) includes events occurring at low rates (average 28 per year) during the years from 1997 to 2004. The second and third periods include rockfalls as well as block-and-ash flows that occurred at high rates during the 2005 precursory and 2006 eruption periods. Some eruptive events were also recorded on a low-light camera operating in Homer, Alaska (Sentman et al., 2010). Detailed analyses of seismograms of rockfalls, including correlation of seismic amplitude ratio and rockfall paths as seen on the low-light camera, were performed by DeRoin et al., (2011). The fourth period includes the post-eruption years 2007-2009 during which the rate of the rockfalls gradually declined. As of this writing (2011) the rates have not yet returned to pre-eruption levels.

3.2. Augustine Island monitoring stations

Augustine Volcano is a 1260 m lava dome complex located on Augustine Island (59°21'45" N, 153°26'6" W) in Cook Inlet, Alaska. Figure 3.1 shows the seismic monitoring stations located on the island. Instruments are either telemetered short-period vertical stations (blue symbols, fig. 3.1) or campaign 3-component broadband stations (red symbols, fig. 3.1). One broadband station, AUL, is telemetered. The short-period stations use analog telemetry and the data are digitized at 100 samples per second (sps) in the seismology laboratory in Fairbanks. The broadband stations use on site digital recording also at 100 sps. Only the short-period stations are used for the automatic event detection algorithm.

During the explosive eruptions of January 11-28, 2006, four of the summit stations (AUS, AUP, AUR, and AUH) were destroyed, as well as station AUL on the north flank. The loss of these stations made locating small earthquakes at Augustine difficult because of too few arrival times. The sensitivity of the automatic event detection system was also affected. Small rockfalls occurring near the summit, which had made up a large fraction of the rockfalls prior to eruption, became impossible to detect. Some of the destroyed stations (AUH, AUP, and AUL) were reinstalled during the summer field season of 2006, but summit stations AUR and AUS have not been reinstalled.

3.3. Automatic event detection

Typically at Augustine, a variable number of seismic triggers occur per day; some are local earthquakes, regional earthquakes, teleseisms, noise events and local events such as rockfalls. Many of the rockfalls generated seismic signals large enough to trigger the automatic seismic event detection algorithm of the EARTHWORM system (Johnson et al., 1995). A trigger occurs when a defined short-term average (STA) of seismic amplitudes exceeds the long term average (LTA) of background seismicity by a pre-defined ratio. Typical durations of the STA and LTA are 1 and 8 s respectively, and thresholds are 2 to 3 (Dixon et al., 2003). The equation used (Dixon et al. 2005) is:

$$1) \qquad \eta = \mathrm{STAR} - \mathrm{RATIO} * \mathrm{LTAR} - |\,\mathrm{STA} - \mathrm{LTA}\,| - \mathrm{QUIET}$$

In equation (1), STAR and LTAR are the corresponding rectified averages of STA and LTA, where STAR is the absolute value of the difference of the seismic trace and the LTA, averaged over one second; LTAR is the absolute value of the difference of the seismic trace and the LTA, averaged over eight seconds. The parameters RATIO and QUIET are set to 2.3 and 4, respectively. When η is less than or equal to zero, the system declares a trigger for that station (Dixon et al. 2005). Each trigger is then manually inspected by an analyst. If the event is identified as a rockfall based on waveform characteristics, it is assigned the code 'X' and labeled as a "rockfall," and saved with the other triggers. In terms of waveform characteristics, rockfall signals in general have emergent onsets, lack clear P and S phases, and have low maximum amplitude to duration ratios. The rockfalls are usually not located. Note, however, that the STA and LTA parameters are designed to detect earthquakes, not rockfalls, so rockfalls may have occurred that were not detected by this system. Nevertheless the system parameters were stable for long periods so the detection of rockfalls was uniform.

Previously the event detection system used was XDETECT (Rogers, 1993), a PC based event acquisition system, but it was replaced by the EARTHWORM event acquisition system in 2002. Event triggering thresholds of XDETECT were similar, with a threshold of 3, but with STA and LTA windows of 32 (.32s) and 1024 (10.24s) samples, respectively. Therefore the period from 1997 to 2001 should be considered uniform, and the period 2002-2009 may also be considered uniform.

Slight differences in rockfall detection may exist between these two periods. However, because seismic analyst personnel has been mostly constant throughout both periods, in general the differences should be small.

3.4. Eruption Chronology

Augustine began erupting in January 2006, following an increase in local volcano-tectonic earthquakes that was first noted in late April 2005. The seismicity continued to increase through the rest of 2005 (Power et al., 2006). Small steam explosions began occurring in December 2005. The first large explosive eruption of Augustine occurred on January 11, 2006. Twelve more large explosive eruptions occurred on January 13, 14, 17 and 28 followed by a phase of continuous ash emission, then by dome growth during which numerous pyroclastic flows and block-and-ash flows occurred. As the unstable lava dome grew in spring 2006, rockfalls and related signals dominated the seismograms (see fig. 3.3 of Power et al., 2006). For additional information on the seismicity at Augustine and seismic precursors to the eruption explosions, see Power and Lalla (2010) and Buurman and West (2010); for eruption chronology see Coombs et al. (2010), and for more information on the pyroclastic flows and lahars see Vallance et al. (2010).

3.5. Characterization of rockfall seismic signals

3.5.1. General rockfall characteristics

Augustine rockfalls and flow events exhibited a variety of seismic waveforms (figs. 3.2 and 3.3). The signal onsets were usually emergent, but some of the shorter duration signals had impulsive (sharper) onsets especially at the closest stations. In the case of summit events the distances of stations to event locations may be only a few hundred meters. The durations of the signals ranged from 10 s to more than 120 s, although some of these longer signals had multiple high amplitude peaks, so these long signals may actually have been several individual rockfalls occurring very closely together in time. Low-light camera images of 2006 block-and-ash flows revealed several instances in which multiple block flows created longer compound seismic signals (Sentman et al., 2010). Frequencies of the rockfall seismograms observed were generally centered around 6-8 Hz (fig. 3.4), although higher frequencies were observed as well, up to 20 Hz. In general the seismic signal of a flow event emerges as the flow moves towards a station and then decays as the flow moves away from it. A steady progression of arrival times across the seismic network is expected, with earlier arrivals at stations closer to the rockfall. This was evident in the Augustine data prior to the destruction of the summit stations, as the signals usually arrived first at the summit stations AUP, AUR, and AUS, and arrived at stations lower on the slope, such as AUW and AUE, several seconds later.

3.5.2. Background years: 1997-2004

The numbers of rockfalls recorded at Augustine Volcano in the years 1997 to 2004 provide a view of the background rockfall behavior (figs. 3.5 and 3.6). The numbers in this period were mostly low, adding up to a total of 224 rockfalls detected, or an average of 28 per year. The rockfalls occurred in nearly all months but most events occurred in the summer and fall (June-November). Although some rockfalls were recorded prior to 1997, station coverage and reliability at Augustine were poor until 1997. The maximum number of rockfalls recorded in one year (in this period) was 69 in 1998, and the minimum was 1 rockfall detected in 2002. The 69 rockfalls in 1998 was a large increase over the 13 recorded rockfalls of the previous year or the 10 in the following year. The majority of the 1998 rockfalls occurred in June and July. During these months, increased steaming of the dome was observed, along with a large avalanche and several mudflows, although temperatures at the summit were reported to be similar to the previous year (McGimsey et al., 2003).

In March 2002, a new event detection system was implemented (Dixon et al., 2003). The old system, XDETECT (Rogers, 1993), a PC based event acquisition system, was replaced by the EARTHWORM event acquisition system (Johnson et al., 1995). For purposes of this study, the two systems returned similar data, although data from 2003 to the present are most uniform, because the seismic stations had fewer outages than in the previous years. In 2003, three years before the eruption, the number of detected events was still low, with 17 rockfalls detected.

The majority of these had long durations of ≥ 30 s and similar station arrival patterns. In the majority of cases signals arrived first at stations AUH, AUR, AUW, and AUL, located on the summit and to the north and west of the volcano. There was one shorter duration (9 s) event that showed up only on the summit stations AUP, AUR, and AUS. Figure 3.2 shows seismic traces typical of the longer duration rockfalls occurring in 2003 and 2004. The main frequencies of these rockfalls were usually ≥5 Hz (fig. 3.4). In 2004, 28 rockfalls were detected and a shift towards shorter rockfalls began. Approximately half of these events arrived at the summit stations first, followed by later arrivals at stations lower on the volcano's flanks. There were also 14 events that only appeared on the summit stations AUP, AUR, and AUS, indicative of small rockfalls on the steep summit dome complex.

Durations of the rockfalls occurring during each period were measured (fig. 3.7). Durations were measured at the stations which appeared to be closest to the rockfalls' location, as determined by the amplitude and duration of the seismic signals. (Signals recorded on farther stations experienced more attenuation and therefore the amplitudes sometimes appeared smaller and durations appeared shorter.) Because the events were recorded by triggering, recording of seismic signals could be clipped, but this was only an issue for signals greater than 120s. The majority of the rockfalls in the background period lasted 60 s or less. Overall, the shorter duration (0-19 s) rockfalls increased in numbers during 2004 and dominated in 2005. The longer duration rockfalls could often be seen on summit stations as well as stations located lower on the volcano, while the shorter duration

events are best observed on summit stations. Smaller rockfalls were apparently more often recorded when they occur near the summit, because stations at the summit are closer together in location so that signals show up on multiple stations in order to cause a trigger.

3.5.3. Precursory sequence and eruption 2005-2006

In mid 2005, there was a dramatic increase of detected rockfalls (347 rockfalls – see fig. 3.6) over previous years, although the event detection methods and settings remained the same (since 2002). There was also a significant increase in the number of short duration events appearing only on the summit stations. This was especially true from May - June, although the short duration events occurred in fall months (September-November) as well. Figure 3.3 shows two of the Augustine short duration summit rockfalls on two stations each. Only one such event occurred in 2003, 12 in 2004, then 234 occurred in 2005. The majority of the detected 2005 events were short duration summit events (fig. 3.7), most of which occurred in May and June 2005. Also in June 2005, a cluster of 13 longer duration rockfall events occurred, that arrived first at stations AUL and AUE, on the lower north and east sides of the volcano, as opposed to the summit.

Interestingly, some of the short duration rockfalls have impulsive onsets, including almost distinguishable P- and S-wave arrivals (see for example, fig. 3.3). To explain why this would be the case with rockfalls, we first note that Jolly et al. (2002), reported that, as seen at Soufriere Hills Volcano, Montserrat, a sudden,

impulsive onset reflects a more explosively triggered rockfall, while a purely gravitational trigger is reflected by an emergent onset. Also a large rock that impacts suddenly and transfers all of its energy into the ground in a fraction of a second should be able to produce seismic traces that have some distinguishable phases. (Phases in seismic signals may be produced by seismic wave reflections and refractions which occur when seismic waves encounter boundaries, e.g. changes in rock densities, in the Earth, and seismic wave multipathing, when seismic waves from the same source follow different paths to the recording station). Rockfalls observed at Mount Spurr in 1993 had sharp onsets and multiple phases on stations near the vent (S. McNutt, unpub. data). The rockfalls could be free falling into the area around the steep summit dome, causing a sudden onset upon impact. (In 2005 the summit dome stood roughly 50 m above the crater. See figure 6 of Coombs et al., 2010, for a topographical map of Augustine).

The change in the number of Augustine rockfalls in 2005 appears to be a precursor to the eruption that was not noticed at the time. Part of the reason for this is that the rockfalls could not be located using arrival time picks, hence the events did not appear on standard seismicity maps and plots used to monitor the volcano. The counts of recorded rockfalls by month for the years 1997-2002 are shown in figure 3.5, and for the years 2003-2009 in figure 3.6. The increase in detected events in 2005 is clear. In December 2005 several phreatic explosions occurred. These produced long duration, wideband signals, similar to some of the longer rockfall events, so there is some ambiguity or possible overlap.

After the explosive eruptions in January 2006, which deposited large amounts of loose tephra, there were numerous rockfall-like signals recorded in seismic data. Many of these were incandescent block-and-ash flows originating from the unstable summit dome. With the destruction of the summit stations early in the eruption (January 11-28, 2006), the ability to record the small summit rockfalls was lost. However, larger rockfalls continued to occur throughout 2006 and were recorded on seismic stations lower on the mountain such as AUW, AUL, AUI, and AUE (fig. 3.1).

Rockfall durations in 2006 resembled the pre-eruption distribution, but with much higher occurrence rates (fig. 3.7). Some of the durations of the 2006 rockfalls may be underestimated, because summit stations were damaged or destroyed in the eruption, and signals measured at stations farther from the rockfalls' locations were attenuated. Clipping of short period stations during the high seismic background of the eruption may have also contributed to errors in durations by making it hard to see when an event began or ended. However, because the summit stations on which the short events were primarily recorded were destroyed (AUS, AUP, and AUR), it is likely that many shorter duration events occurred but were not recorded. Extrusion of juvenile material ceased by March 16, 2006 (Coombs et al., 2010), however rockfalls continued to occur throughout the year.

3.5.4. Post-Eruption Rockfalls

Post-eruption, the rates of rockfalls decreased while still remaining much higher than the background years, 1997-2004. The pattern of highest rockfall rates in May/June, which is clear in 2005, still holds for 2007 to 2009 (fig. 3.6). In 2007 and 2008 the peak numbers were also in May, and the numbers of rockfalls generally declined steadily from May to November. By 2009 the peak had shifted and the decline pattern was less regular than 2007-2008. Figure 3.8 shows the decline in the rockfalls from 2007 to 2009. The yearly total number of rockfalls as well as the number of rockfalls in the peak month of each year appears to decline in a similar fashion. The decline from 2006 to 2007 may be even greater as the number of rockfalls in January 2006 is likely underestimated due to destroyed stations (some of which were replaced in summer 2006) and noise from eruption signals. Overall the number of rockfalls appears to be gradually returning to background rates and may return to the level seen before 2005 in a few years. The post-eruption rockfall durations resemble those of 2005, with the shorter duration events again dominating.

3.6. Mechanisms

The data show four types of rockfall occurrence. Two types are related to volcanic activity and include the rockfalls occurring during the precursory eruptive stage in 2005 and the rockfalls occurring during the eruption in 2006. Other types appear to fall into two patterns of seasonal/weather-related occurrence, with one pattern observed in the spring and the other in the fall. These patterns suggest

several mechanisms causing the rockfalls. Here we attempt to identify the key features of the different mechanisms for each period of rockfalls.

3.6.1. Steaming and heating at summit

3.6.1.1. Precursory rockfalls

The large increase in rockfalls occurring in spring 2005 precursory to the 2006 volcanic eruption clearly stands out from the background events. Possible causes of this increase in rockfalls are considered here. The large increase in rockfalls in May 2005 coincided with the increase in shallow volcanic earthquakes that was first noted on April 30, 2005 (Jacobs and McNutt, 2010). The increase in summit rockfalls in 2005 also occurred just after a temperature increase of 20-25 °C over previous summers was observed in the seismic station AUS vault (Jacobs and McNutt, 2010). Ambient temperature recorded at station AUS was one of the parameters used to determine the state of health of the stations. Temperature was measured only at this station. The temperature was measured with a thermistor (LM335A thermocouple) located approximately 1.4 m off the ground, and was reported every 12 hours from October 2000 to January 2006 (Jacobs and McNutt, 2010). The temperature increase was determined to be likely volcanic in nature (Jacobs and McNutt, 2010). The temperature increase could be due to one or more factors, including ground heating due to conduction or air heating due to increased steaming or nearby fumarolic activity. The addition of water to the ground materials caused by the presence of steam can cause an increase in pore-water pressures,

thereby reducing the confining pressures of the ground materials while the shear stresses remain constant.

Other factors, such as ground deformation and earthquake shaking causing the rockfalls have been considered. According to Cervelli et al. (2010) precursory deformation began in mid August 2005, so ground inflation probably did not cause the earlier (May-June) rockfalls. The occurrence of rockfalls with respect to earthquakes is another factor to consider in determining causes and triggers of rockfalls. The data show a similar pattern of occurrence with a systematic offset of about 1 day between earthquakes and rockfalls. Due to the offset and the fact that the earthquakes were small (most $M < 1.0$), we see no basis that individual earthquakes triggered specific rockfalls (fig. 3.9). The rockfalls at the end of April 2005 show a similar pattern of occurrence to that of the earthquakes (fig. 3.9), suggesting the same factors were responsible for the increase in both earthquakes and rockfalls. Specifically, we infer that increased heat and gases likely accompanied the increase in deeper seismicity (0-2 km below the summit), and the rockfalls occurred because the ground surface became more unstable as the heat and gases interacted with the surface materials.

A study of seismic b-values by Jacobs and McNutt (2010) lends strength to the pore pressure hypothesis mentioned above. In this study, seismic b-values were calculated for the long pre-eruptive earthquake swarm from April 30, 2005 to Jan 11, 2005, and the short pre-eruptive swarm immediately before the eruption in 2006. Seismic b-values are measures of the numbers of earthquakes occurring at certain

magnitudes and changes in b-values can reflect changes in volcanic environments. The long swarm was divided into three sections corresponding to stages of deformation as reported by Cervelli et al. (2006): June 1, 2005 to November 17, 2005; November 17, 2005 to December 10, 2005; and December 10, 2005 to January 11, 2006. The short swarm included the 13 hours immediately preceding the beginning of the eruption on January 11, 2006. Jacobs and McNutt (2010) found the b-values of the long-swarm (1.26 +/- 0.04) to be higher than the short swarm (.781 +/-.02). They note that high b-values have been attributed to increased pore pressures (Wyss, 1973) and thermal gradients (Warren and Latham, 1970). Overall, however, both pre-eruptive swarms had lower b-values than the background year periods (1.44 +/- .05 for January 1, 2000 to April 29, 2005). They attribute the lower b-values to increase of stresses at Augustine occurring during the pre-eruptive long swarm. The initial phase (beginning June 1, 2005) of the long swarm in which the rockfalls occurred had a lower b-value than that reported in the second phase (beginning November 17, 2005), and the higher b-value of the second phase is attributed to a dike intrusion as inferred by Cervelli et al. (2010). However, figure 7 in (Jacobs and McNutt, 2010) shows that the very beginning of the long seismic swarm, April 30-June 1, had a higher b-value than the following period. This temporary peak of b-values corresponds with the beginning of high rockfall occurrence, and lends strength to the hypothesis that higher pore pressures were leading to the high numbers of rockfalls.

3.6.1.2. Background years

Steaming at the surface may have also been a factor in causing rockfalls in earlier years at Augustine as well. 1998 was an anomaly among the background years in that 69 rockfalls occurred that year, with the majority of them occurring in July. Steaming was observed in July 1998 (McGimsey, et al., 2003), and therefore we infer that steam rising to the surface and heating the ground may have contributed to ground instability. Another incident of increased steaming which may have helped to cause rockfalls was reported in September 2003 (McGimsey et al., 2005), which was also the month that the highest numbers of rockfalls were recorded in 2003. However, in the 2003 case, even though the maximum number of rockfalls were recorded in September, this was only 5 rockfalls total. The steaming was reported on September 9, and the 5 rockfalls were recorded on September 1, 6, 7, and 27. Again pore pressure increase of ground materials caused by the steaming may have been a factor in the ground instability leading to the 1998 and 2003 rockfalls.

3.6.2. Dome growth and collapse and eruptive concurrent rockfalls

The rockfall events concurrent with the eruption include the February-March 2006 flow events (although rockfalls occurred throughout the eruption) that were determined from low-light camera images and geologic deposits data to be block-and-ash flows (Sentman et al., 2010; Coombs et al., 2010). During periods of dome growth, new hot material comes up to the dome surface, causing lobes or spines of lava to be extruded. The newly added material can increase steepness of the dome,

which can lead to instability and partial dome collapse. Coombs et al. (2010) suggests that the Augustine block-and-ash flows are similar to rockfall-induced block-and-ash flows seen at Unzen volcano. According to Ui et al. (1999) these block-and-ash flows occurred when the pore pressure of the lava and downslope tensional forces exceed the tensile strength of the deforming lava, causing a local explosion and fragmentation at the lobe front. Extrusion of juvenile material ceased by March 16, 2006 (Coombs et al., 2010). With new material no longer being extruded, growth and steepening of the dome stops, and rockfalls and dome collapses should eventually cease as the slope returns to gravitational stability.

3.6.3. Weather-related rockfalls

Two other types of rockfall patterns can be observed in figures 3.5 and 3.6. In the years 1997, 1999, 2003, 2004 and 2006 (minor peak), the peak numbers of rockfalls occurred in the late summer/early fall (months of September to November). This corresponds to the season when the summit was clear of snow, temperatures were above freezing, and rainfall rates were highest (fig. 3.10). Referring again to figure 3.5, in 1997, 12 of the 13 recorded rockfalls occurred in the fall, and the majority of those were in September. September was also the month (in 1997) with the highest rainfall rates. Appendix A shows several years of rainfall data at Homer, Alaska, located 112 km from Augustine volcano, for an overview of the weather patterns in that area.

Rainfall is a known cause of landslides and rockfalls. Rainfall may cause landslides by increasing the pore-water pressures within the ground materials of the slope. For a given slope there exists a critical pore-water pressure level, which when reached, causes ground instability (Keefer et al., 1987). Four factors of rainfall lead to landslide initiation: total rainfall, short-term storm intensity, antecedent storm precipitation, storm duration (Sidle and Ochiai, 2006). Previous studies have shown that intensity of rainfall may be more important to triggering landslides than long-term rainfall (e.g. Keefer et al., 1987; Larsen and Simon, 1993). Antecedent moisture, i.e., moisture already present in the slope materials at the time of rainfall, is also an important factor as prior periods of precipitation can form higher pore pressure creating conditions ripe for rockfalls to be triggered by a period of intense rainfall (Larsen and Simon, 1993). Long duration storms have been found to be correlated to triggering of deep seated mass movements (Sidle and Ochiai, 2006). A combination of all factors (total precipitation, intensity, antecedent moisture and rainfall duration) will likely contribute to creating the ground instability and eventual triggering of landslides and rockfalls. Although rainfall data more detailed than daily rainfall amounts (such as rainfall intensity) were not available for this study, we can nonetheless infer that many of these rockfalls were generated by the higher amounts of rainfall occurring in these months.

3.6.4. Seasonal rockfalls

In the years 1998, 2000, 2001, 2005, 2007, and 2008, the peak numbers of rockfalls were detected in the spring/summer months of May, June, and July. To explain the high numbers of spring and early summer rockfalls, we note weather patterns again. Appendix B shows the temperatures at Augustine Volcano (and Homer, Alaska, when temperatures from Augustine were not available). Loose or unstable summit material, combined with warming temperatures in spring/summer may be responsible for rockfall generation. As the temperatures begin to rise above thawing in May and June (fig. 3.10B) for parts of the day, freeze-thaw processes may occur. Water-rich surface material may alternately begin to thaw and then re-freeze, and the stretching and compression during freezing and thawing could contribute to ground instability in the summit region.

In 2000, 47 rockfalls were recorded with the maximum in June. June was the month in which the temperatures rose above freezing at the summit of Augustine (Appendix B). Rockfalls continued to occur throughout October, as the temperatures at the summit hovered slightly above freezing and then dropped and remained below freezing after October. In 2001 there were 27 rockfalls recorded, and again June was the month in which the maximum numbers of rockfalls were recorded. June was also the month in which temperatures at the summit began to rise about freezing. As opposed to 2001, when the temperatures hovered around the freezing point for a few months, the temperatures rose completely above freezing after July, which may account for less rockfalls the following months. The rockfalls of 2003 may have also

been a result of freezing temperatures rather than rainfall or steaming because September was the month in which the temperatures began to drop below freezing.

3.6.5. Post-eruption rockfalls

Rockfall numbers for 2007-2009 remained higher than the 1997-2004 background numbers. The mechanisms behind these rockfalls are most likely similar to those of the background years: rainwater from storms and instability caused by warming temperatures in spring; however, the increased amount of loose material due to the eruption causes the rates of the rockfalls in 2007-2009 to be higher. A slight change in the patterns of rockfall occurrence is noted between 2007/2008 and 2009. In 2007 and 2008 the peak numbers of rockfalls occurred in May, as in 2005. Several background years had peak months of rockfall numbers in June. Looking at the temperature data (Appendix B) shows that in 2007 and 2008 temperatures at Augustine were hovering around 4 degrees Celsius during most of May and have risen above 4 degrees by June. In 2009, the temperatures are rising above freezing also, but are not as steady as in 2007 and 2008. As long as no new material is erupted, the rockfall rates are expected to continue to decline in the future.

3.7. Discussion

In the preceding section, several possible mechanisms for rockfall generation were described. Some of these mechanisms have been observed to occur at other volcanoes previously. Precursory rockfalls have been observed at Soufriere Hills

Volcano, Montserrat, when increasing numbers of rockfalls have been observed as precursors to some eruptions (De Angelis et al., 2007). The difference between Soufriere Hills Volcano and Augustine precursor rockfalls is that the Soufriere Hills Volcano rockfalls occurred during a dome growth period while the dome was hot, while the precursory rockfalls at Augustine occurred eight months before the eruption, as the old cold lava dome was being heated by rising steam and gases.

Seasonal effects of various types have also been reported at Alaskan volcanoes. For example, eruptions at Pavlof Volcano, Alaska often occur in the northern hemisphere fall (McNutt, 1999). In the months of January and February, shore-ice events are frequently seen at Augustine. In contrast, glacial seismic activity is also frequently recorded at Redoubt and Spurr, but is highest in the summer (e.g. Leblanc et al., 2008). Post-eruption surficial seismicity was higher in summer months following the 1992 eruptions of Mount Spurr (McNutt, 1998); this activity is very similar to the Augustine post- eruption activity. Volcanic and rockfall activity has also been found to be related to rainfall and weather. Mastin (1994), reports that at Mount St. Helens, during the long-lasting dome building eruption, violent tephra explosions were triggered by rainfall occurring during storms, and Yamasoto et al. (1998) report that some pyroclastic flow and lava dome collapses at Unzen Volcano were caused by rainfall, and also that higher rates of precipitation increased the probability of pyroclastic flows and dome collapses.

The main characteristics of rockfalls occurring during four periods (the background years, precursory phase, eruptive phase, and post-eruptive phase) at

Augustine Volcano have been described and possible causes for them have been given. The data suggest that freeze-thaw cycles and steaming may be the most likely causes of the rockfalls. Rain is likely still a factor, but there is less evidence showing rockfall occurring after a period of high rainfall. The numbers of rockfalls occurring in fall were generally lower than in spring.

Although for some periods discussed (such as in 2003 during the observed steaming events), small numbers of rockfalls were involved, making it more difficult to draw conclusions about the rockfalls' causes, the main conclusions of this analysis were drawn from periods in which seismic station coverage was consistent over long periods of time, and the rockfalls occurred in large enough numbers that the addition or subtraction of a few rockfalls would not make a noticeable difference in the data.

3.8. Conclusions

Many rockfalls were detected at Augustine Volcano, Alaska before, during and after the 2006 eruption. Two distinct seasonal patterns of rockfall occurrences were observed: one in which lower overall numbers of rockfalls were detected and the peak numbers per year occur in the months September to November, and one in which higher overall numbers of rockfalls were detected and peak numbers occurred in the months May to June. Both of these patterns occur in the years before and after the eruption and are attributed to unstable ground due to steaming or heating, rainfall and loose summit materials. The seasonal patterns of the rockfalls occurring in the background and post-eruption years appear to be caused by a combination of weather

patterns, eruptive activity, and summit instability. The rockfalls occurring in the background years appear to be more closely related to the freeze-thaw cycle in spring and late fall than rainfall; however, rain is still considered to be factor in rockfall generation (figs. 3.5, 3.6 and 3.10). The high rate of rockfalls in 2005, which coincided with eruption precursors (seismicity and heat), is attributed to increased steaming at the summit, caused by subterranean gases and steam rising to the summit and creating instability in the ground, and were a clear sign that the summit had become unstable. During the dome growth and collapse phase many block and ash flows were detected as well. The eruption of block and ash flows was independently confirmed by the low-light camera in Homer, Alaska. The events that occurred in the four periods at Augustine show that a combination of seasonal effects and instability due to heating and lubrication due to gases and steam, as well as lava dome growth, may be responsible for the changing patterns and numbers of rockfalls. At this time rockfalls are still occurring at Augustine and the level of occurrence has not yet returned to the background levels observed prior to 2005. Monitoring strategies are currently being adjusted to take rockfalls into account at other Alaskan volcanoes, because they may be potential precursors to eruptions and therefore offer additional insight to the physical processes occurring.

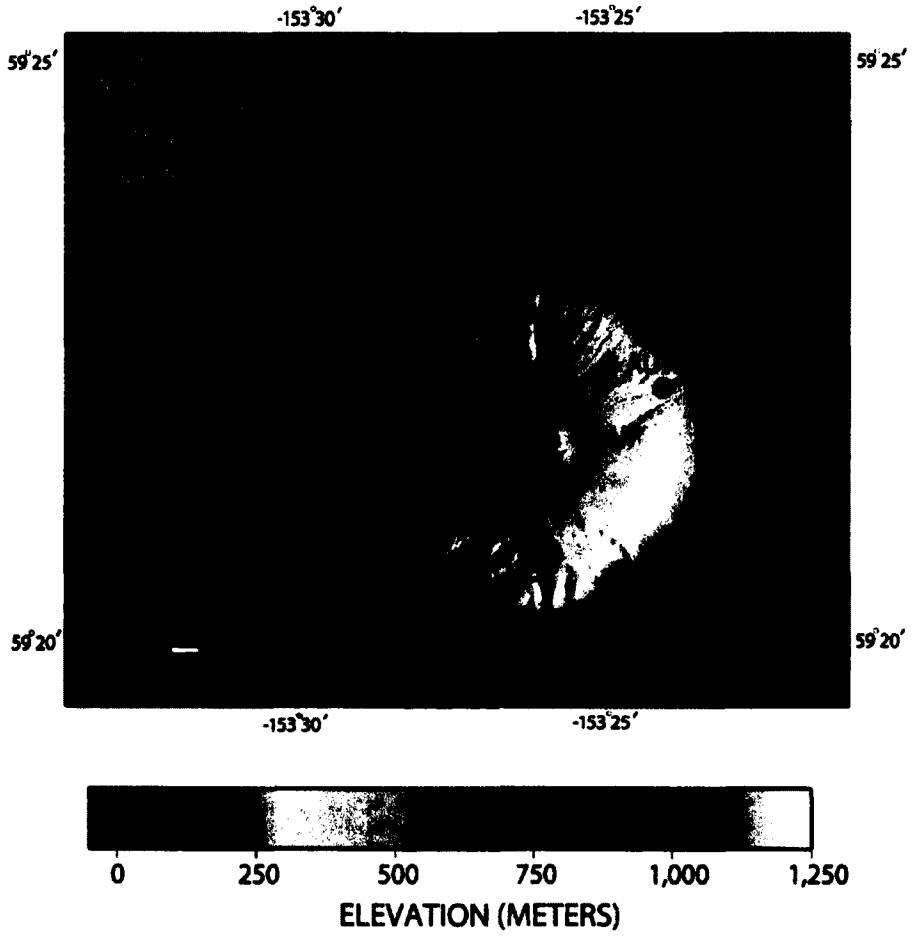

Figure 3.1

Map of seismic stations on Augustine. The permanent telemetered seismic stations and campaign broadband seismic stations have blue and red symbols, respectively. All of the permanent stations are short period, except AUL, which is a broadband station. AUP, AUH, AUR, AUS, and AUL were all damaged or destroyed during the eruption. Since then, AUL, AUP and AUH have been repaired. The lowlight camera in Homer is 112 km to the east of Augustine. The arrow on the figure points in the direction of the camera. (Figure modified from H. Buurman.)

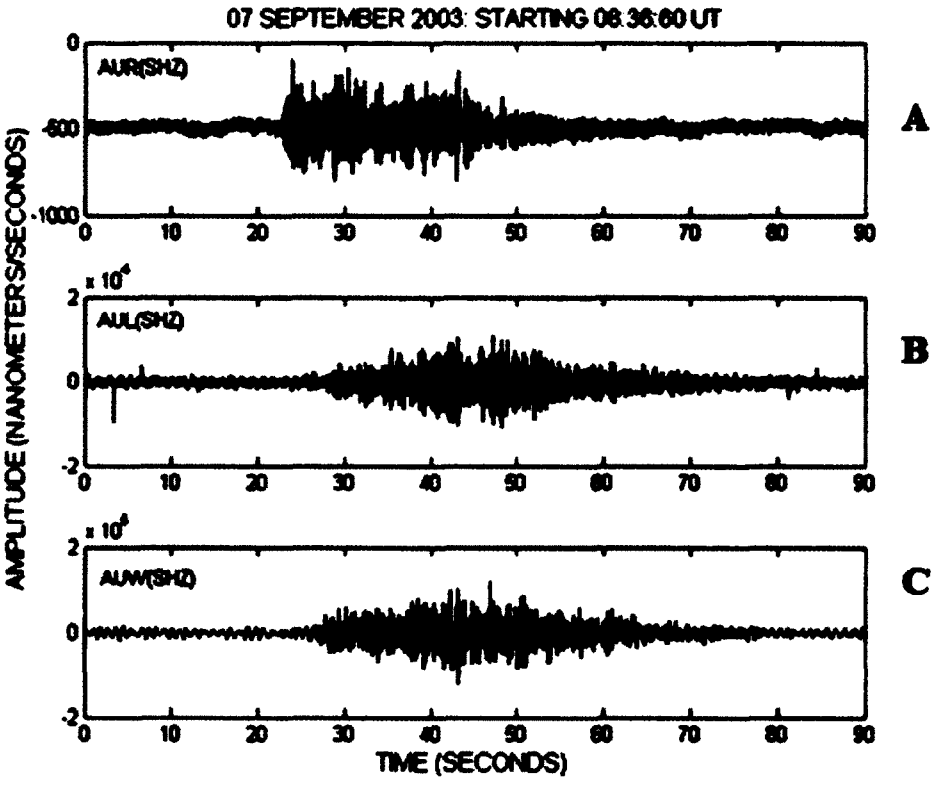

Figure 3.2

Seismograms of longer duration rockfalls. The rockfalls here are typical of those occurring 2003 - 2004, last 30 seconds or longer, and arrive first at summit stations (AUP, AUR (shown in A), AUH, and AUS) and then arrive later at lower elevation stations (AUW and AUL (shown in B and C) , and AUE). The lower event is a compound event, appearing on the summit stations (D) AUS, (E) AUR, and (F) AUP. SHZ is the channel code for the vertical component of short-period sensors. Note the difference in amplitude scales.

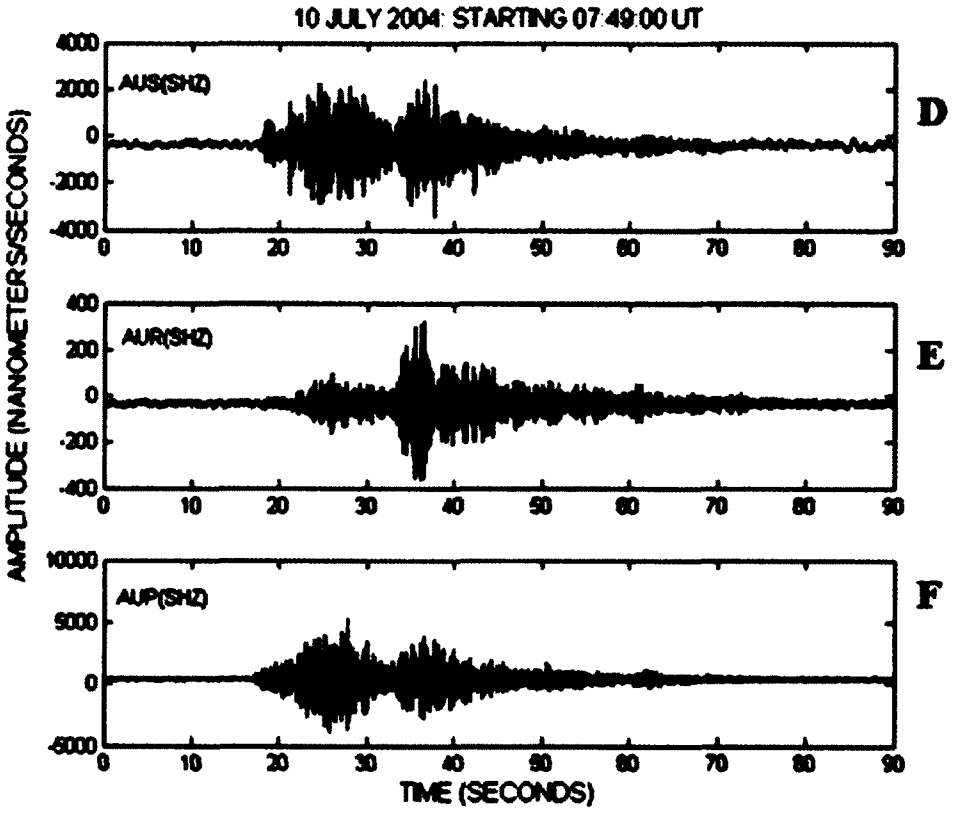

Figure 3.2 continued

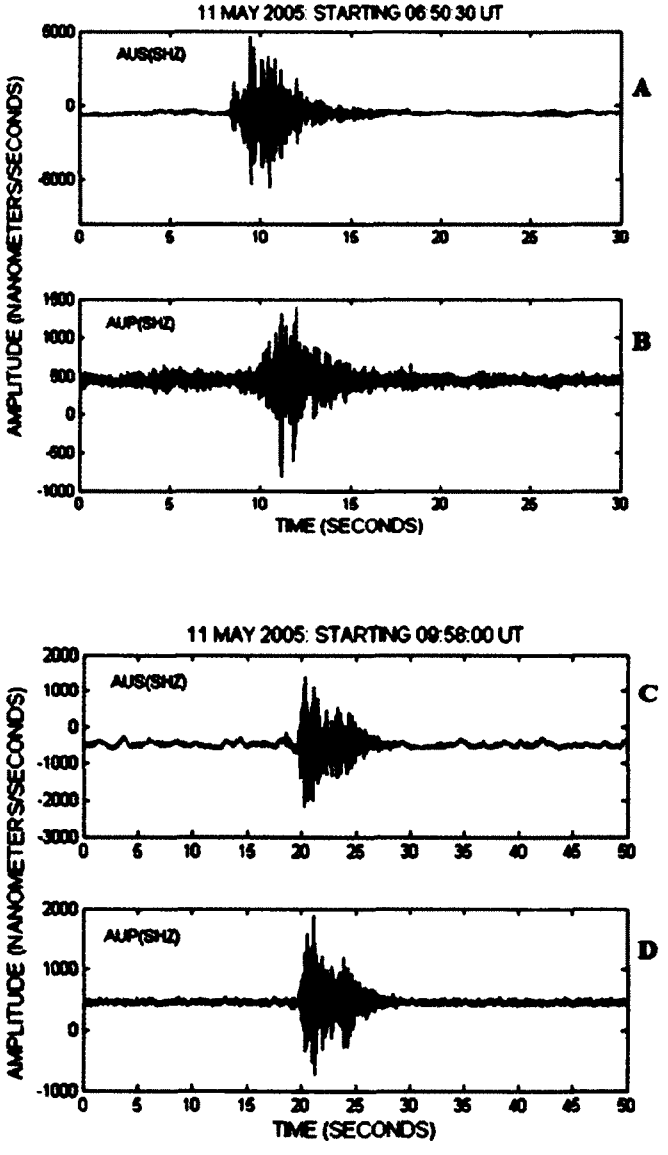

Figure 3.3

Seismograms of shorter duration (<30 seconds) rockfalls. The examples here only appear on the summit stations AUR, AUS (see A and C), and AUP (see B and D). SHZ is the channel code for the vertical component of short-period sensors. Note the different time and amplitude scales.

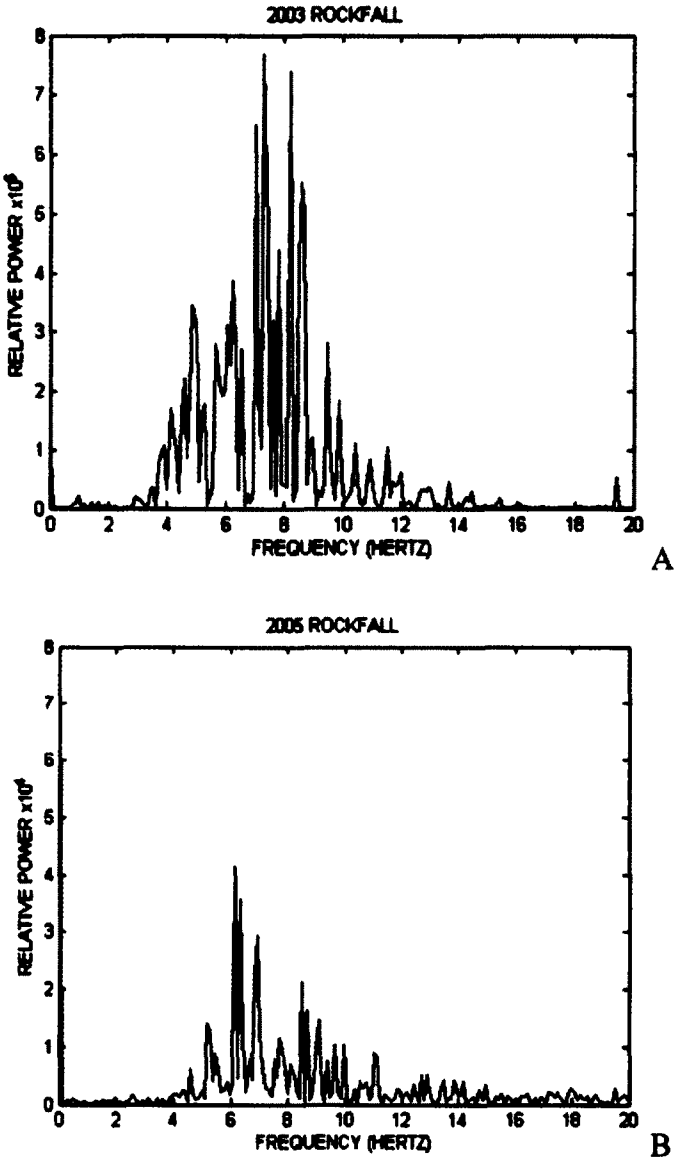

Figure 3.4

Power spectral density plots for two rockfalls. (A) shows a rockfall from 2003 and was recorded on station AUH, and B) shows rockfall from 2005, recorded on station AUS. The dominant frequencies for A range from 7 to 9 Hz, while those of B are between 6 and 7 Hz.

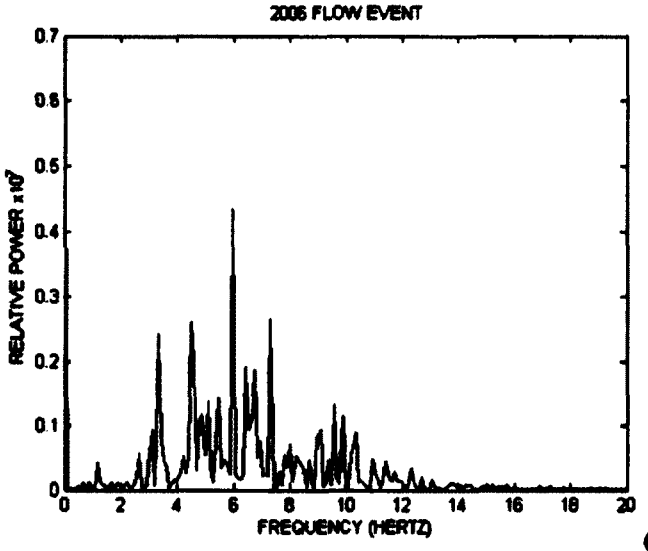

C

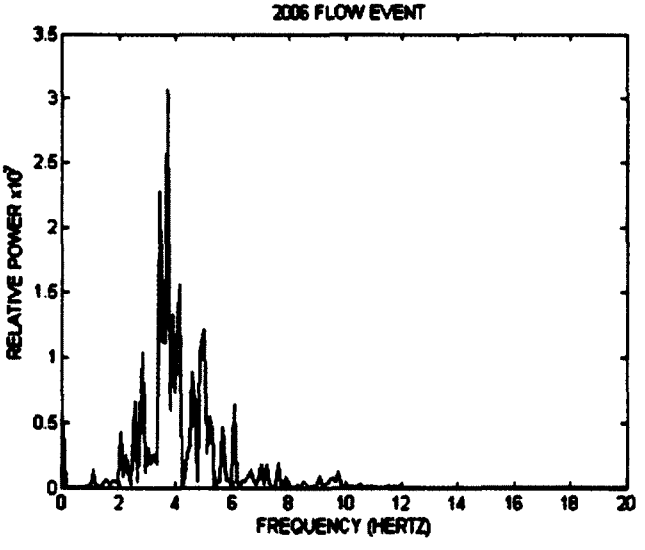

D

Figure 3.4 continued

C) and D) power spectral density plots for two flow events in 2006, recorded on station AUE. The dominant frequencies of these events are 6 Hz and between 3 and 4 Hz, respectively.

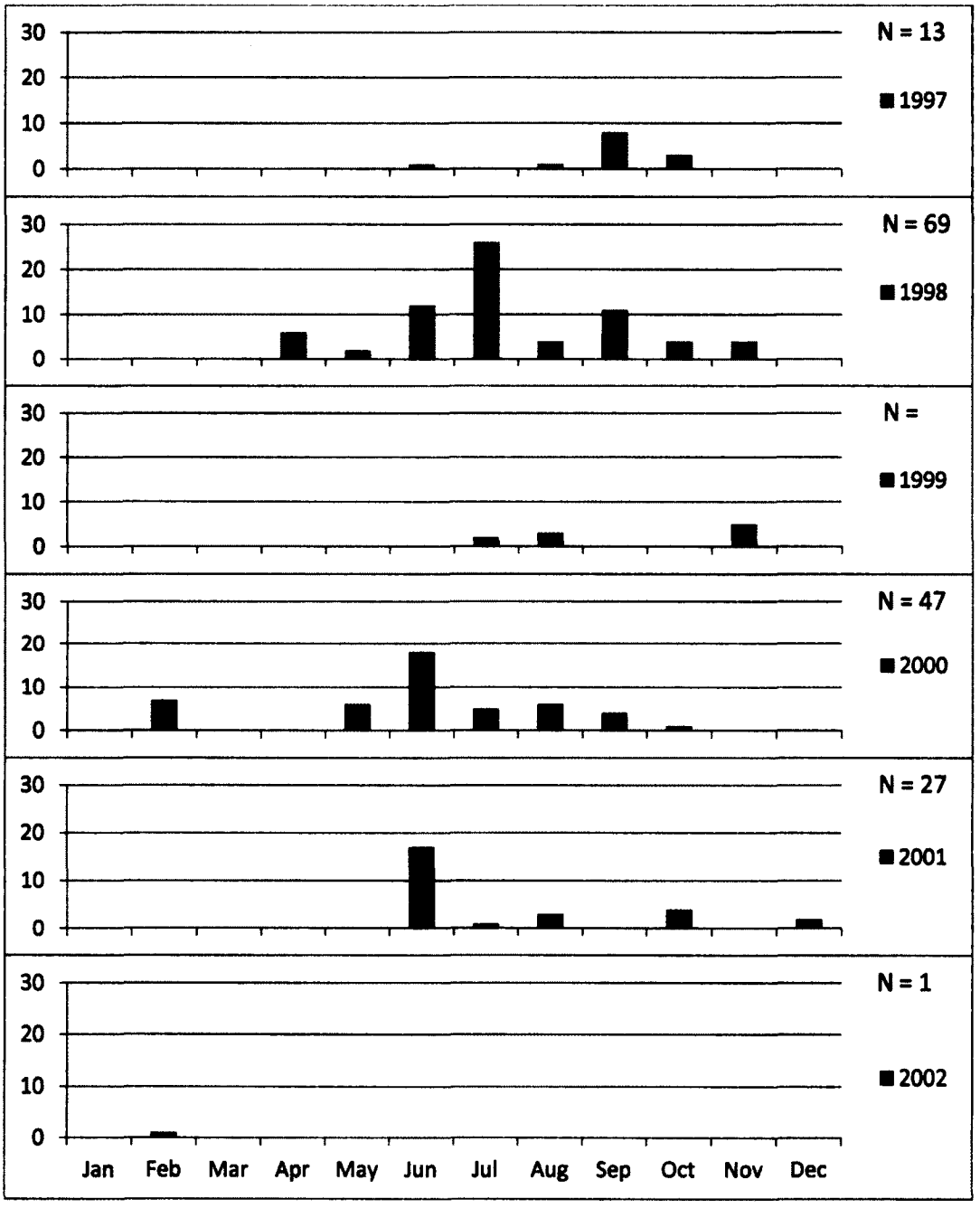

Figure 3.5

Monthly rockfall rates for 1997-2002. Peaks occur during the summer months of June and July, and during the fall months of September to November.

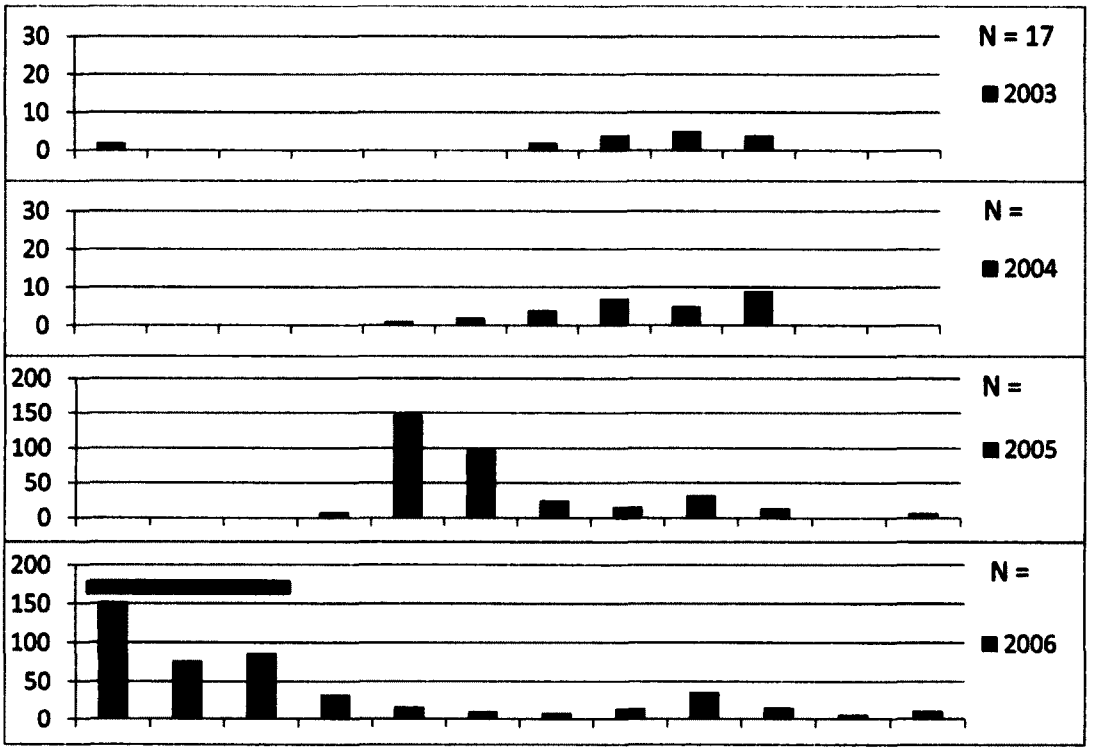

Figure 3.6

Monthly rockfall rates for 2003-2009. The background years of 2003 and 2004 show that most rockfalls occurred during the months of heaviest rainfall (see also Figure 3.10A). In 2005, the peak numbers of rockfalls occurred in May and coincided with the first increase of seismic activity in April-May. In 2006, the rockfall rates were affected by the eruption (indicated by heavy horizontal line) and the highest numbers occurred in January. In 2007 and 2008, the peak numbers were again in May. Note that the vertical scales are different for various years.

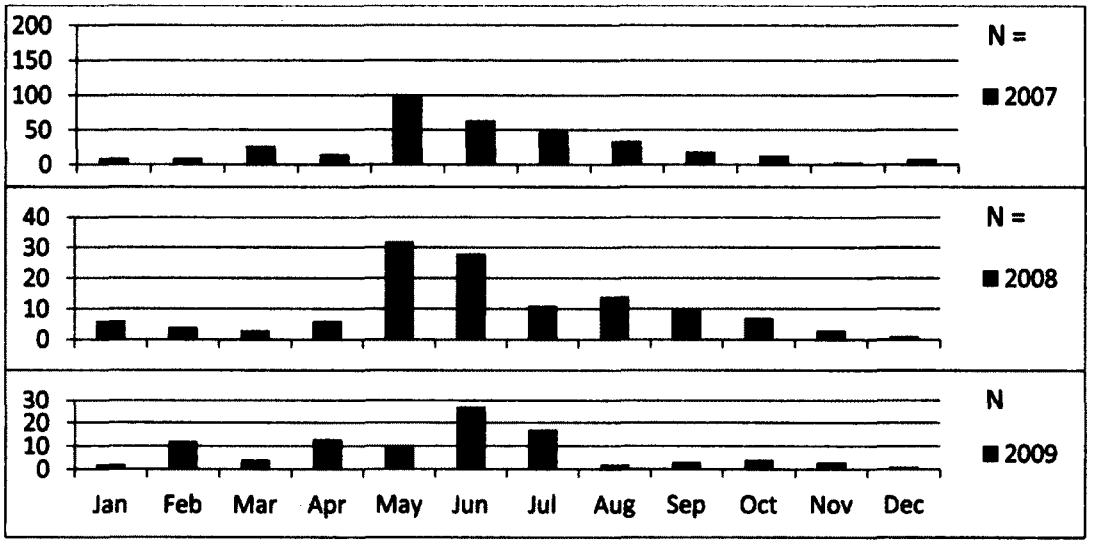

Figure 3.6 continued

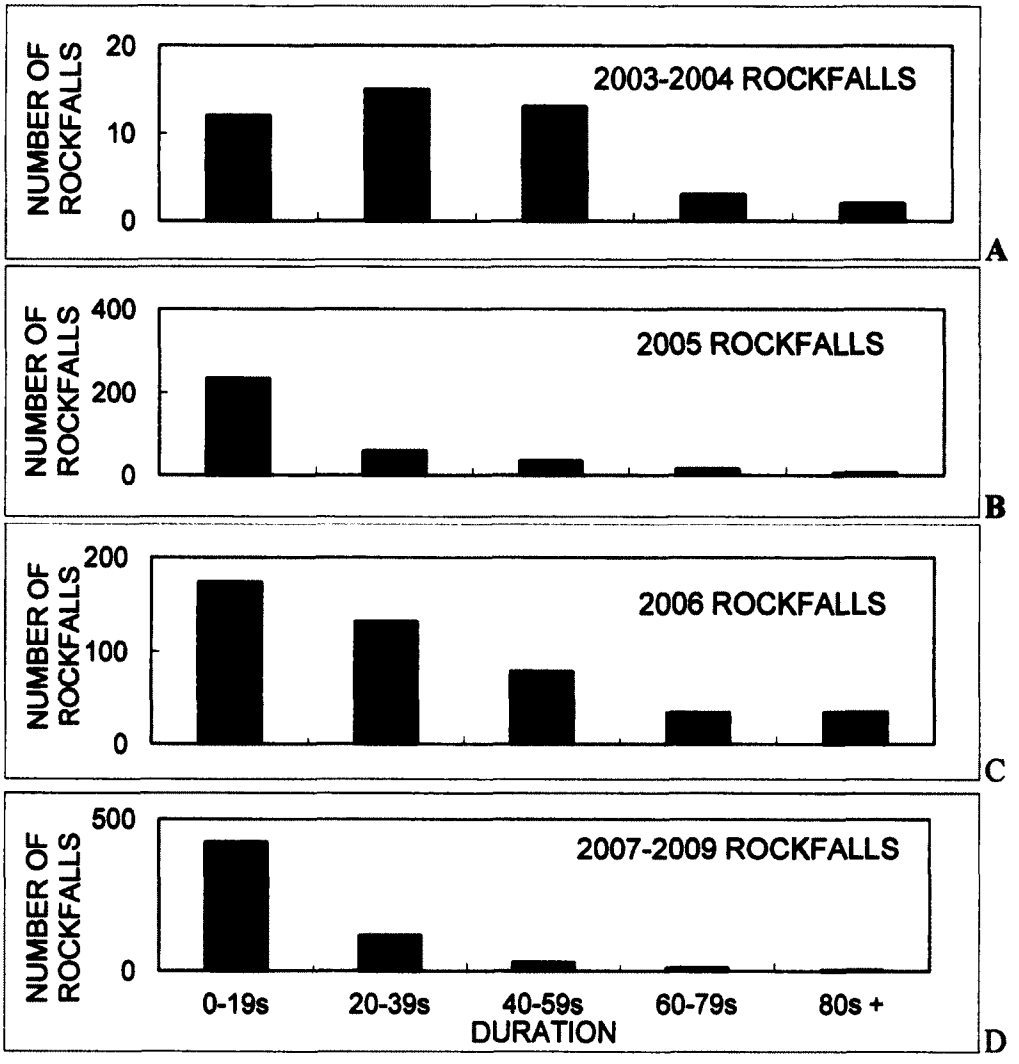

Figure 3.7

Histogram of rockfall durations for 2003-2009. A) 45 rockfalls in 2003 and 2004 show the background activity. B) 347 rockfalls occurring in 2005, showing the increase in occurrence of the shorter duration summit rockfalls. C) 370 rockfalls from 2006; these data also include some co-eruptive signals. D) 572 rockfalls from 2007-2009, likely due to heat and unstable ground.

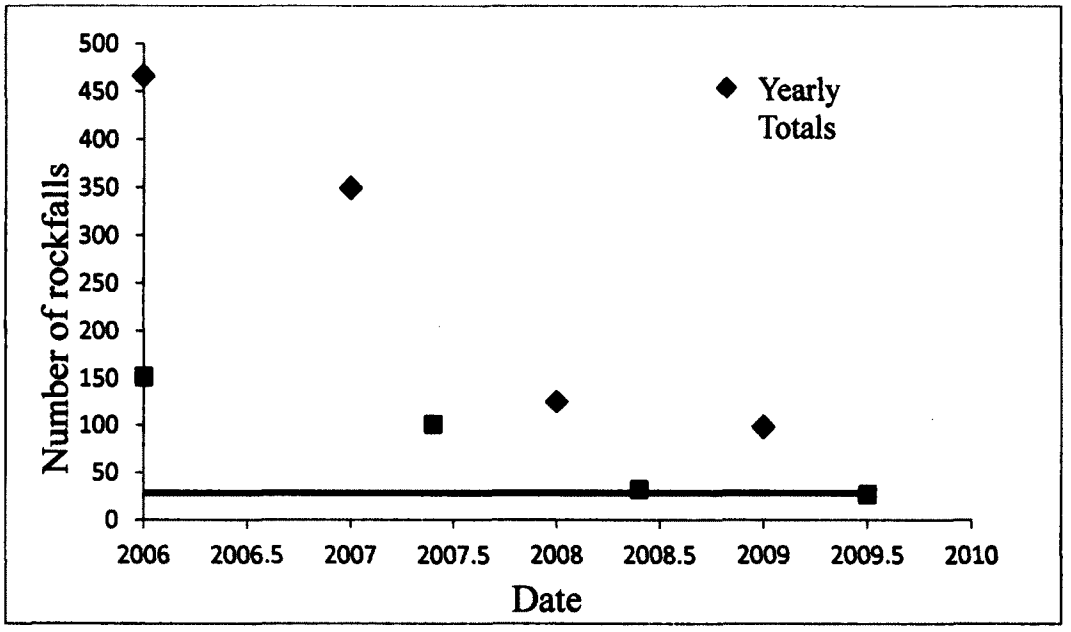

Figure 3.8

Decline in rockfall numbers over time. The diamond symbols are the total number of rockfalls per year and the square symbols are the total of rockfalls from the peak month of each year. The horizontal straight line is the average of the yearly number of rockfalls occurring in the background years of 1997-2004. Both yearly total and peak month plots show a steep decline that is now beginning to stabilize around less than 100 events per year and with a peak month of about 25 events. (Although it is not plotted here, data for 2010 has since become available and fits into the general pattern as well).

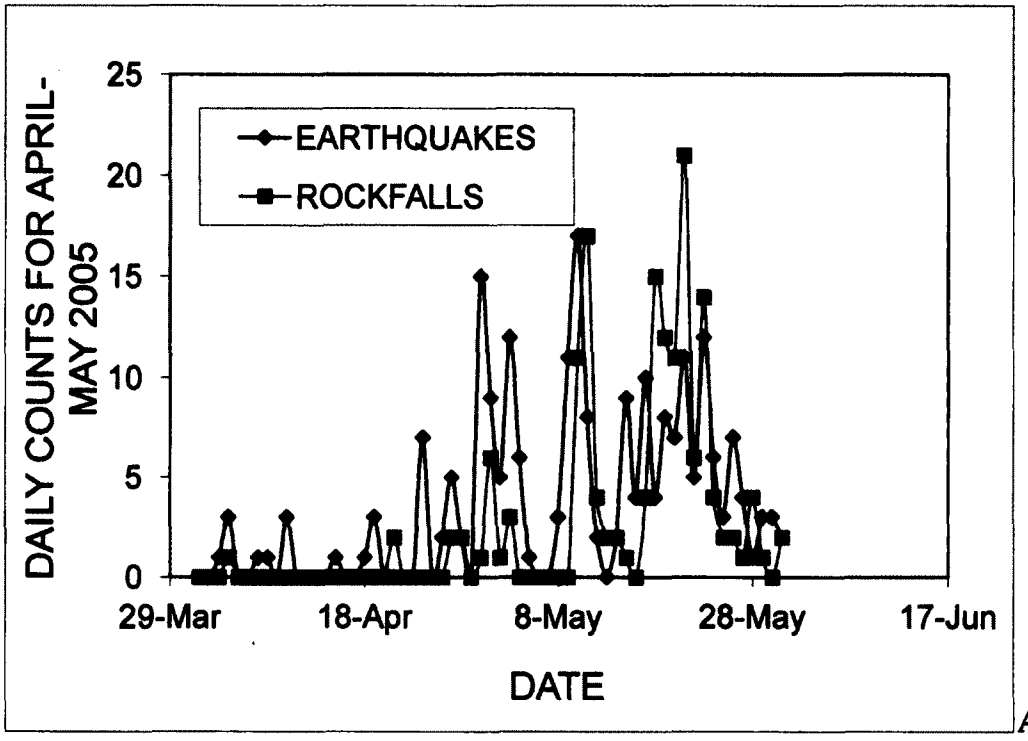

A

Figure 3.9

Daily numbers of rockfalls and volcanic earthquakes in April-May 2005. A) The daily numbers of rockfalls (red squares) and volcanic earthquakes (black diamonds) in April and May of 2005. The rockfalls occur in a similar pattern to the earthquakes but are delayed by about 1 day, suggesting that similar factors are responsible for both the rockfalls and the earthquakes, but that the earthquakes themselves are not directly triggering the rockfalls.

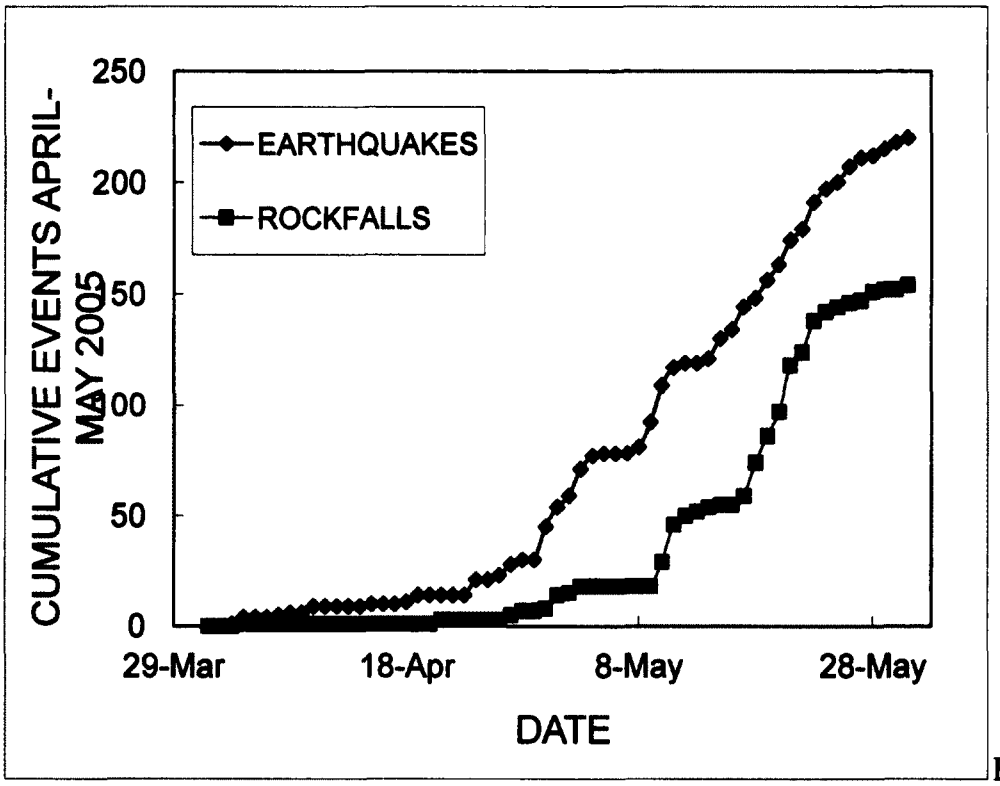

B

Figure 3.9 continued

B) Cumulative numbers of earthquakes and rockfalls in April/May 2005. Symbols are the same as in part A. Note that the data is in points, where each point is the daily or cumulative total. The lines on the plot are therefore not 'real data' but are used to better show the offset between earthquakes and rockfalls.

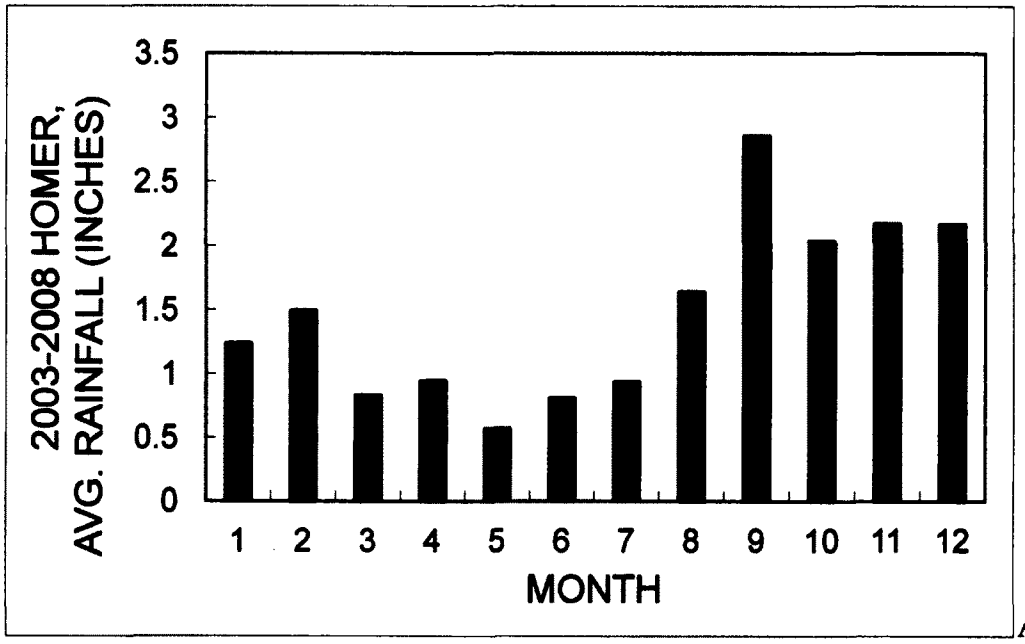

A

Figure 3.10

Stacked monthly rainfall rates and average temperatures at Homer. A) Stacked monthly rainfall rates at Homer, AK, near Augustine Island for 2003-2008. The late summer/autumn months typically experience the most rainfall.

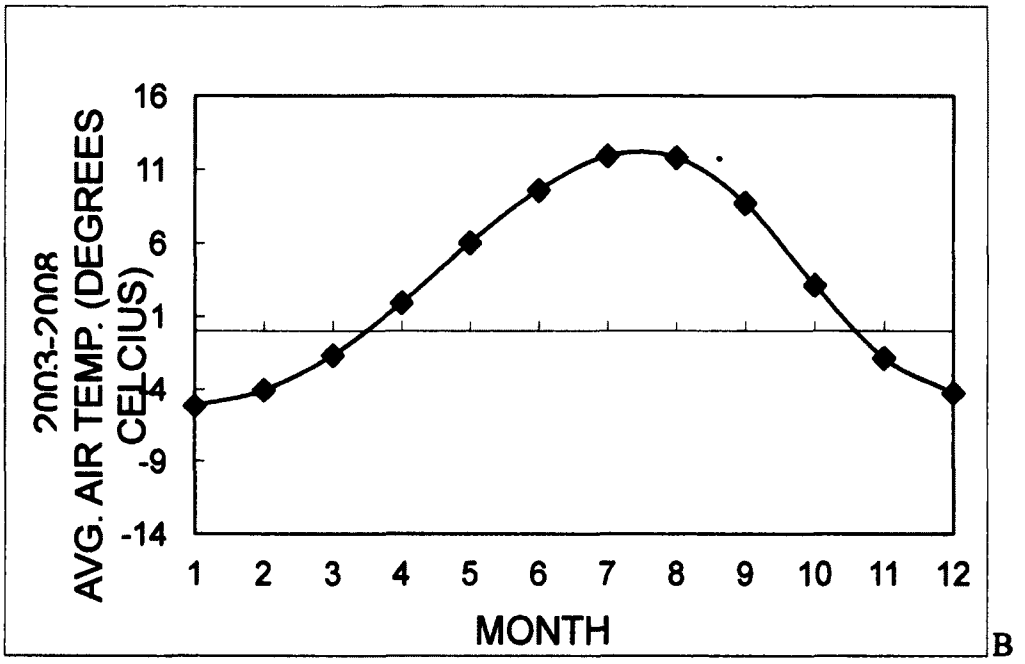

Figure 3.10 continued

B) Average monthly temperatures for Homer, AK. Note that temperatures at the summit of Augustine will be about 4°C cooler than the sea level temperatures shown. Even after the temperature rises above freezing, it may take some time before the ground thaws, so according to the average temperatures shown in the figure, thawing of the ground and melting of snow and ice likely occurs in May and June. Rainfall and temperature data come from Climate-Zone (2009) and the National Climate Data Center (2009).

3.9. References

Buurman, H.,West, M., 2010. Seismic precursors to volcanic explosions during the 2006 eruption of Augustine Volcano. U.S. Geological Survey Professional Paper 1769, p. 41-57.

Cervelli, P.F., Fournier, T.J., Freymeuller, J.T., Power, J.A., 2006. Ground deformation associated with the precursory unrest and early phases of the January 2006 eruption of Augustine Volcano, Alaska. Geophysical Research Letters, 33, doi: 10.1029/2006GL027219.

Cervelli, P.F., Fournier, T.J., Freymeuller, J.T., Power, J.A., Lisowski, M., Pauk, B.A., 2010. Geodetic constraints on magma movement and withdrawal during the 2006 eruption of Augustine Volcano. U.S. Geological Survey Professional Paper 1769, p. 427-452.

Climate-Zone, 2009. http://www.climate-zone.com

Coombs, M.L., Bull, K.F., Vallance, J.W., Schneider, D.J., Thoms, E.E., Wessels, R.L., McGimsey, R.G., 2010. Timing, distribution, and character of proximal products of the 2006 eruption of Augustine Volcano, Alaska. U.S. Geological Survey Professional Paper 1769, p. 145-185.

Cruden, D.M., Varnes, D.J., 1996. Landslide types and processes, in Landslides—Investigation and Mitigation, edited by Turner, A.K., and Schuster, R.L., p.36-75, Special Report 247, Transport. Res. Board, National Res. Council, National Academic Press, Washington, D.C.

De Angelis, S., Bass, V., Hards, V., Ryan, G., 2007. Seismic characterization of pyroclastic flow activity at Soufriere Hills Volcano. Natural Hazards and Earth System Science 7, no. 4, p. 467-472.

DeRoin, N., McNutt, S.R., Sentman, D.D., Reyes, C.G., 2011. Seismicity of Block-and-Ash Flows Occurring During the 2006 Eruption of Augustine Volcano, Alaska. Journal of Volcanology and Geothermal Research. 213-214, p. 14-26.

Dixon, J.P., Power, J. A., Stihler, S.D., 2005. A Comparison of Seismic Event Detection with IASPEI and Earthworm Acquisition at Alaskan Volcanoes. Seismological Research Letters, 76, no. 2, p. 168-176, DOI: 10.1785/gssrl.76.2.168

Dixon, J.P., Stihler, S.D., Power, J.A., Tytgat, G., Moran, S.C., Sanchez, J., Estes, S., McNutt, S.R., Paskievitch, J., 2003. Catalog of Earthquake Hypocenters at Alaskan Volcanoes: January 1 through December 31, 2002. U.S. Geological Survey Open-File Report 03-267. 58 p.

Jacobs, K., McNutt, S.R., 2010. Seismicity rates and processes during the earthquake swarm preceding the 2006 eruptions of Augustine volcano. U.S. Geological Survey Professional Paper 1769, p. 59-83.

Johnson, C.E., Bittenbinder, A., Bogaert, D., Dietz, L., Kohler, W., 1995. EARTHWORM: A Flexible Approach to Seismograph Network Processing. Incorporated Research Institutions for Seismology Newsletter, 14, no.2, p. 1-4.

Jolly, A.D., Thompson, G., Norton, G.E., 2002. Locating pyroclastic flows on Soufriere Hills volcano, Montserrat, West Indies, using amplitude signals from high dynamic range instruments. Journal of Volcanology and Geothermal Research, 118, p. 299-317.

Keefer, D.K., Wilson, R.C., Mark, R.K., Brabb, E.E., Brown, W.M., Ellen, S.D., Harp, E.L., Wieczorek, G.F., Alger, C.S., Zatkin, R.S., 1987. Real-time landslide warning during heavy rainfall. Science, New Series, Vol. 238, p. 921-925.

Larsen, M.C., Simon, A., 1993. A rainfall intensity-duration threshold for landslides in a humid-tropical environment, Puerto Rico. Geografiska Annaler. Series A, Physical Geography, Vol. 75, p. 13-23.

Leblanc, L., Larsen, C., West, M., Truffer, M., O'Neel, Shad, 2008. Time-Series Analysis of Icequakes and Ice Motion, Bering Glacier, AK. Eos Trans AGU, 89(53), Fall Meet., Suppl., Abstract C11D-0535

Mastin, L.G., 1994. Explosive tephra emissions at Mount St. Helens, 1989-1991: The violent escape of magmatic gas following storms? Geological Society of America Bulletin, 106, p. 175-185. DOI: 10.1130/0016-7606.

McGimsey, R.G., Neal, C.A., Girina, O., 2003. 1998 volcanic activity in Alaska and Kamchatka: Summary of events and response of the Alaska Volcano Observatory. U.S. Geological Survey Open-File Report OF 03-0423, 35 p.

McGimsey, R.G., Neal, C.A., Girina, O., 2005. 2003 volcanic activity in Alaska and Kamchatka: Summary of events and response of the Alaska Volcano Observatory. U.S. Geological Survey Open-File Report 2005-1310, 62 p.

McNutt, S.R., 1998. Actions Taken and Lessons Learned from Volcanic Seismology in Alaska, 1989-1998. Eos Trans. Amer. Geophys. Union, 79 no. 45, supplement, p. F973.

McNutt, S.R., 1999. Eruptions of Pavlof Volcano, Alaska, and their possible modulation by ocean load and tectonic stress: Re-evaluation of the hypothesis based on new data from 1984-1998. Pure Appl. Geophys., 155, p. 701-712.

National Climate Data Center (NCDC), 2009. http://www.ncdc.noaa.gov/oa/ncdc.html

Power, J.A., Lalla, D.J., 2010. Seismic observations of Augustine Volcano, Alaska; 1970 – 2007: U.S. Geological Survey Professional Paper 1769, p. 3-40.

Power, J.A, Nye, C.J., Coombs, M.L., Wessels, R.L., Cervelli, P.F., Dehn, J., Wallace, K.L., Freymueller, J.T., Doukas, M.P., 2006. The reawakening of Alaska's Augustine Volcano. Eos, 87, no. 37, p. 373-377.

Rogers, J.A., 1993, XDETECT version 3.18 users reference guide, U.S. Geological Survey Open-File Report 93-261-A, 25p.

Sentman, D.D., McNutt, S.R., Stenbaek-Nielsen, H.C., Tytgat, G., DeRoin, N., 2010. Imaging observations of thermal emissions from Augustine volcano using a small astronomical camera. U.S. Geological Survey Professional Paper 1769, p. 569-577.

Sharpe, C.F.S., 1938. Landslides and related phenomena, a study of mass movements of soil and rock, Columbia Univ. Press, New York, 137 p., reprinted 1960 by Pageant Books Inc., Paterson, N.J.

Sidle, R.C., Ochiai, H., 2006. Landslide: Processes, Prediction and Land Use. Water Resources Monograph 18. American Geophysical Union, Washington, D.C., 312 p.

Surinach, E., Vilajosana, I., Khazaradze, G., Biescas, B., Furdada, G., Vilaplana, J.M., 2005. Seismic detection and characterization of landslides and other mass movements. Natural Hazards and Earth System Sciences, 5, p. 791-798.

Ui, T., Matsuwo, N., Sumita, M., Fujinawa, A., 1999. Generation of block and ash flows during the 1990-1995 eruption of Unzen Volcano, Japan. Journal of Volcanology and Geothermal Research, 89, p. 123-138.

Vallance, J.W., Bull, K.F., Coombs, M.L., 2010. Pyroclastic flows, lahars and mixed avalanches generated during the 2006 eruption of Augustine Volcano. U.S. Geological Survey Professional Paper 1769, p. 221-267.

Varnes, D.J., 1978. Slope Movement types and processes. In Special Report 176: Landslides: Analysis and Control (R.L. Schuster and R.J. Krizek, eds.) TRB, National Research Council, Washington, D.C., p. 12-33.

Warren, N.W., Latham, G.V., 1970. An experimental study of thermally induced microfracturing and its relation to volcanic seismicity. Journal of Geoophysical Research, 75, p. 4455-4464.

Wieczorek, G.F., 1996. Landslide triggering mechanisms, in Landslides—Investigation and Mitigation, edited by Turner, A.K., and Schuster, R.L., p. 76-90, Special Report 247, Transport. Res. Board, National Res. Council, National Academic Press, Washington, D.C.

Wyss, M., 1973. Towards a physical understanding of the earthquake frequency distribution. Geophysical Journal of the Royal Astronomical Society, 31, p. 341-359.

Yamasoto, H., Kitagawa, S., and Komiya, M., 1998, Effect of rainfall on dacitic lava dome collapse at Unzen volcano, Japan. Papers in Meteorology and Geophysics 48, No. 3, p. 73-78.

Chapter 4

Seismicity of Block-and-Ash Flows Occurring During the 2006 Eruption of Augustine Volcano, Alaska[3]

Abstract

In January 2006, Augustine Volcano began erupting following an increase in seismicity that was first noted in late April 2005. Thirteen large explosive eruptions of Augustine occurred from January 11 to 28, 2006, followed by a continuously erupting phase and then by a dome growth phase in which numerous pyroclastic flows and block-and-ash flows occurred. As a new steep-sided and unstable dome grew in spring 2006, rockfalls and related signals, likely block-and-ash flows, dominated the seismic record. Relative amplitudes at pairs of seismic stations for 68 block-and-ash flow events were examined to constrain locations of the flow-events. Higher amplitudes were associated with events closer to a given station. These relations were confirmed by images collected on a low-light camera. Captured images show a correlation between flow direction and seismic amplitude ratios from nearby stations AUE and AUW. Seismic amplitudes and energies of the flow signals, measured in several different ways, were found to correlate with the surface areas and run-out distances of the flows. The M_L range of rockfalls was 0.1 to 1.1,

---

[3] DeRoin, N., McNutt, S.R., Sentman, D.D., and Reyes, C. 2011. Seismicity of Rockfalls and Block-and-Ash Flows Occurring During the 2006 Eruption of Augustine Volcano, Alaska. Journal of Volcanology and Geothermal Research, 2011, 213-214, 14-26. http://dx.doi.org/10.1016/j.jvolgeores.2011.10.007

and seismic efficiencies were estimated to be much less than 1%. Particle motion analyses showed that the seismic waves contained both body waves and surface waves and demonstrate that the flows were acting as moving sources with velocities of 30-93 m/s.

4.1. Introduction

Rockfalls and other flows are common features at active volcanoes. Previous researchers have studied the seismicity of rockfalls at several volcanoes, including rockfalls and avalanches in the Cascades Range (Norris, 1994), pyroclastic flows at Unzen (Uhira et al., 1994), and nuees ardentes at Merapi (Brodscholl et al., 2000). Norris's study on Mount St. Helens' rockfalls found a nearly linear relation between seismic amplitude and rockfall source volume. Calder et al. (1999) observed contrasting mobilities of several types of pyroclastic density currents at Soufriere Hills volcano, Montserrat, and found that dome-collapse flows had mobilities similar to cold rockfalls. Researchers have also located pyroclastic flows using seismic amplitudes or other seismic data. Battaglia and Aki (2003) developed a method of locating rockfalls and other signals at Piton de la Fournaise volcano using seismic amplitudes. Jolly et al. (2002) located pyroclastic flows using amplitudes of signals from a seismic array at Soufriere Hills Volcano, Montserrat. Kumagai et al. (2009) developed a method to locate lahars at Cotopaxi volcano, Ecuador, based on tremor signals. Studies of the seismic efficiency (conversion of potential energy to seismic energy) of rockfalls have been done previously. The ratios of seismic to potential

energy were found in one study to be 0.25 (Vilasojana et al., 2008) and in another, 10^{-6} to 10^{-3} (Deparis and Jongmans, 2008). Weichert et al. (1994) found a correlation between the seismic efficiency and the slope of the detachment surface. Studies of block-and-ash flows compared with visual data have been done by Ui et al. (1999), who observed block-and-ash flows at Unzen volcano, Japan, with video cameras. They observed two mechanisms of flow generation, depending on whether exogenous or endogenous dome growth was occurring.

Even before its eruption in 2006, Augustine has been a source of numerous rockfalls. Many of these rockfalls generated signals large enough to trigger the automatic seismic event detection algorithm of the EARTHWORM system. In this system, a trigger occurs when a defined short-term average (STA) of seismic amplitudes exceeds the long term average (LTA) of background seismic activity by a pre-defined ratio. Typical durations of the STA and LTA are 1 and 8 s respectively, and thresholds are 2 to 3 (Dixon et al., 2003). The STA/LTA triggering system is currently used for all the seismically monitored volcanoes of the Alaska Volcano Observatory (Johnson et al., 1995; Dixon et al., 2010). For further analysis of the background, precursory and post-eruption rockfalls see DeRoin and McNutt (2011). During the course of the 2006 eruption, the volcano produced many incandescent flows as it entered into a state of continuous eruption in late January. A low-light astronomical camera recorded numerous images of rockfalls and block-and-ash flows occurring at the same time as the recorded seismic traces (Sentman et al., 2010).

The goal of this paper is to determine the extent to which constraints can be placed on rockfall events based on seismic data. Rockfall events are generated by different mechanisms than earthquakes (i.e. brittle rock fracture and fluid flow for volcano tectonic and volcano low-frequency earthquakes respectively) so calculations which are commonly made for earthquakes cannot be meaningfully applied to rockfalls. However, seismic measurements of rockfalls have been correlated to many characteristics of rockfalls previously. To this end, various measurements of seismic amplitudes, magnitudes, and energies have been calculated to determine which quantities can best be related to observed rockfall characteristics.

4.2. Augustine Island monitoring stations

Augustine Volcano is a 1260 meter lava dome complex located on Augustine Island (59°21'45" N, 153°26'6" W) in Cook Inlet. The seismic monitoring stations located on Augustine Island, and operated by AVO are shown in Figure 4.1. Instruments are either telemetered short-period vertical stations (blue symbols, fig. 4.1) or campaign 3-component broadband stations (red symbols, fig. 4.1). One broadband station, AUL, is telemetered. The short-period stations use analog telemetry and the data are digitized at 100 samples per second (sps) in the seismology laboratory in Fairbanks. The broadband stations use digital recording also at 100 sps. Only the short-period stations are used for the automatic event detection algorithm.

During the explosive eruptions January 11-28, the summit stations (AUS, AUP, AUR, and AUH) were destroyed, as well as AUL on the north flank. The loss of these stations made locating earthquakes at Augustine difficult. Small rockfalls occurring near the summit, which had made up a large fraction of the rockfalls prior to eruption, became impossible to detect. Some of the destroyed stations (AUH, AUP, and AUL) were reinstalled during the summer field season of 2006, but summit stations AUR and AUS have not been reinstalled. A low light camera also monitored the volcano from Homer, located 112 km east of Augustine, beginning on January 21, 2006. The low-light camera was originally installed to record lightning at the volcano, but it has proved to be useful in recording incandescent block-and-ash flows occurring during the effusive phase and the dome growth and collapse phase (Sentman et al., 2010). The camera, a monochrome Starlight Xpress model SXV-M7 16-bits/pixel integrating astronomical camera with a USB 2.0 external interface, uses a 1/2 inch format Sony ICX429ALL monochrome 752- by 582-pixel CCD array, with pixel dimensions 8.6.by 8.3 μm (Sentman et al., 2010). The lenses used for most observations were a Tamron 35 mm f/2.4 CCTV (11.0° by 8.2° field of view, 26.6-m/pixel resolution at the observing distance of 105 km to Augustine Island) and a Sigma 135 mm f/1.8 (2.85° by 2.0° field-of-view, 6.89-m/pixel resolution at Augustine Volcano) (Sentman et al., 2010). Pictures were taken at different intervals throughout the eruption, but the images from February 8 were taken fifteen seconds apart. To compare the seismic data with the camera images, a time period was needed during which both low-light camera images of flows and

high quality seismic data were available. Although the dome growth and collapse period produced many flows throughout the eruption, and the low-light camera recorded data on several nights, the corresponding seismic data were not always suitable for analysis. High background noise and clipping of seismic data, which occurred during many periods of block-and-ash flows, limited the available time periods for analysis. Data from February 8, 2006, including seismic data and video images, were best suited for this analysis, because the weather was clear and because the high rate of dome growth resulted in many flows. At this time the seismic stations were functioning properly, the data had good signal-to-noise ratios, and the seismic traces from the short-period stations were not saturated.

4.3. Eruption chronology

Augustine began erupting in January 2006, following an increase in seismicity that was first noted in late April 2005. The seismicity continued to increase through the rest of 2005 (Power et al., 2006). Small steam explosions began occurring in December 2005. The first large explosive eruption of Augustine occurred on January 11, 2006. Twelve more large explosive eruptions occurred on January 13, 14, 17 and 28 followed by a phase of continuous ash emission, then by dome growth in which numerous pyroclastic flows and block-and-ash flows occurred. As the unstable lava dome grew in spring 2006, rockfalls and related signals dominated the seismograms. Cervelli et al. (2010) describe the deformation of the edifice throughout the eruption. For more information on the seismicity at

Augustine and seismic precursors to the eruption explosions, see Power and Lalla (2010) and Buurman and West (2010); for eruption chronology see Coombs et al. (2010), and for more information on the pyroclastic flows and lahars see Vallance et al. (2010).

The number of different types of seismic events that occurred at Augustine during the 2006 eruption was counted and is shown in a summary plot in Figure 4.2. Daily counts of events at Augustine with amplitudes exceeding 5000 nm per second were made and classified as either "volcano-tectonic" or "rockfall and explosive" (M. West, unpub. data). The events labeled "rockfall and explosive" made up the majority of the events counted in February (fig. 4.2). Many of these occurred in early February at rates as high as 19 events per hour. Observations from the low-light camera show that block-and-ash flows did occur at very high rates such as this.

4.4. Analysis of seismic signals and lowlight camera images

4.4.1. Estimation of block-and-ash flow path from seismic amplitude ratios

During the course of the 2006 eruption, the volcano produced many incandescent flows as it entered into a state of continuous eruption in late January. Field observations of these flows are discussed by Vallance et al. (2010). A low-light astronomical camera recorded numerous images of rockfalls and block-and-ash flows occurring at the same time as the recorded seismic traces (Sentman et al., 2010). These images provided confirmation of the flows' occurrences, locations, sizes, starting and ending heights, and run-out distances, with varying degrees of

uncertainty. The locations of the flows, as seen in the camera images, match with the location of the mapped block-and-ash flow deposits (Coombs et al., 2010) As seen on the camera, which faces the east side of the volcano (fig. 4.1), the block-and-ash flows traveled by two main routes: down the north slope (and appearing on the right side of the low-light camera images) or down to the northeast (to the front-right on the images). Pyroclastic flow and rockfall deposits were present on other slopes (S, SW, etc) of the volcano as well as seen in Coombs (2010); however, the majority of the flows during the continuous phase of the eruption occurred in the areas shown on the camera. They generated emergent seismic signals, with no clear P- or S-wave arrivals, and with durations generally <2 min. Low-light camera images of 2006 block-and-ash flows revealed several instances in which larger compound signals are created by overlapping or superimposed seismic signals from multiple consecutive block flows. Comparison of the seismic traces of the block-and-ash flows seen in the videos showed that when the flows are moving to the east, the peak seismic amplitudes at AUE, the station on the east flank, were usually higher than those at AUW (fig. 4.3). When the block-and-ash flows went to the north, the amplitudes at AUE and AUW were usually roughly equal (fig. 4.4).

Figure 4.5 shows a set of seismograms of two block-and-ash flows occurring within 2 min of one another and their corresponding camera images. The flows are moving in different directions and have different amplitude ratios on AUE and AUW. The flow going to the north has a larger seismic amplitude at AUW and smaller amplitude at AUE, while the flow going to the northeast has a large

amplitude at AUE but a very small amplitude at AUW. This pair of images and seismograms, just minutes apart, confirms the basic observation that is further analyzed in the remainder of this paper.

Ratios of maximum peak-to-peak amplitudes were used to compare the flow directions with the seismic signals. Peak-to-peak amplitude measurements were made because they are analogous to seismic magnitudes, and they can be performed quickly in real-time monitoring situations. To ensure that the peak-to-peak amplitudes used were not being affected by random noise spikes, however, root-mean-squared (RMS) amplitudes of the entire traces were also calculated and were found to correlate well with the peak-to-peak amplitudes (fig. 4.6). Next, ratios of peak-to-peak amplitudes at AUE and AUW were compared with the images to determine if the rockfall paths seen on the low-light camera correlated with the amplitude ratios. This was done in order to test the hypothesis that if the amplitude ratio of AUE/AUW for a particular flow was equal to about 1 (with amplitude ratios in the range .95 to 1.04), then the flow was approximately equidistant from AUE and AUW; and that if the amplitude ratio was greater than 1, the flow likely traveled more towards the east (AUE); and finally that if the same ratio is less than 1, the flow traveled down the west (AUW) side of the volcano. Of all the rockfalls in this same data set seen on the video going to the northeast, 85% had AUE/AUW ratios greater than 1. While events with AUE/AUW amplitude ratios greater than 1 were not guaranteed to flow to the northeast as opposed to the north, as the AUE/AUW

amplitude ratios increased, the percentage of events that traveled to the northeast also increased.

4.4.2. Seismic efficiencies

One goal of this study was to calculate the seismic efficiencies of the block-and-ash flows. The seismic efficiency is the percentage of the total energy that goes into producing seismic waves. A typical value for the seismic efficiency for earthquakes and other seismic events is 1% (Scholz, 1990), and varying values have been calculated for rockfall events, from 25% (Vilasojana et al., 2008) to .0006% (Weichart et al., 1994; Deparis and Jongmans, 2008). In order to find the seismic efficiency for a block-and-ash flow, the total energy and the seismic energy for that flow are needed. To calculate the seismic efficiency, we chose several large events that showed up clearly on both the camera images and seismic data. The kinetic energy was calculated for the individual flows, using measurements of size and speed made from the low-light camera images. The seismic energy was calculated from the seismic data; first magnitude calculations were made, then energy was estimated from magnitude, via the Gutenberg-Richter energy-magnitude relationship (Richter, 1958).

4.4.3. Volume calculations and errors

In order to estimate seismic efficiencies, volume estimates were needed for the individual flow events to calculate mass and energy. Several approaches were

tried and the results were compared with the camera images, while taking into account the limitations of volume estimates obtained from the camera. We calculated volume estimates for several individual flows, by assuming the flows to be half-ellipsoids (with equal height and width radii) and calculated the volumes based on measurements obtained from the camera images. These were compared with the geological field estimate of the total volume of erupted material in the months of February and March, which is $5.3x10^7$ m^3 and includes lava dome growth, lava flows and pyroclastic and block-and-ash flows (Coombs et al., 2010). After comparing our data with the geological field estimates for the intervals with video evidence of flows or seismic activity indicative of flow activity, we estimate about $2.7x10^7$ m^3 of the above estimate corresponds to the flows similar to the ones we have observed on the video. Comparing this volume estimate with our total volume estimate of $2x10^{10}$ m^3 (obtained from the video images and total event numbers, (fig. 4.2)), we find that our results are systematically overestimated by a factor of about 740, (assuming the deposits have not been underestimated due to erosion or washout). In order to bring our estimates of individual event volumes into agreement with geological estimates, we recalculated them with this correction factor. A rock density of 1670 kg/m^3, the density of the inflated eruptive deposits (Coombs et al., 2010), was used to find the masses after the volume was calculated.

Although comparing our volume estimates with the geological field estimates helped to bring our values more in line, overall the low-light camera proved to be unsuitable for volume calculations for several reasons. According to Harris et al.

(1997) and J. Dehn (pers. comm.) heat sensing cameras are susceptible to several effects that can exaggerate the apparent size of the incandescent event. First, pixel to pixel bleed can cause pixels with no incandescent material in them to be counted. There is also the fact that a small amount of incandescent material, taking up only a few percent of the area of the actual pixel, can cause the whole pixel to be illuminated. The pixels used in this study are 26.6 m x 26.6 m = 707 m^2 in area. If a pixel of this size is counted in the surface area estimation when only 1-10% of the pixel area is actually filled with incandescent material, this can lead to overestimations of 1 to 2 orders of magnitude. Third, the camera records hot material, which may be solids or gases. Overall, then, all the factors of which we are aware render the lowlight camera data not suitable for volume estimates. The video data remain useful for determining directions and relative sizes, but not absolute sizes or volumes.

4.4.4. Energy estimations

Because the total distances the flows have traveled and the propagation velocities are known or can be estimated (from the video and deposit maps), the kinetic energies of the flows can also be estimated. These energies can then be compared with the seismic energy releases to determine the seismic efficiencies of the events. Estimates of the kinetic energies were calculated for the flows from video images. The kinetic energy was calculated using the equation $\frac{1}{2} mv^2$, where m is the individual event mass, and v is the velocity of a particular flow as determined

from the videos, using the run-out distance and the video duration. Because the camera images were taken at fifteen second intervals, a maximum of 30 s of error can be produced in the durations, if the flow begins immediately after one image is taken and ends immediately before another image is taken. Velocity errors are dependent on total time of the events, but for typical events studied here, the errors range from 14% to 50%. Velocities likely vary throughout the course of the flow, so overall averages are used here. Errors in the kinetic energy calculations can therefore be large (up to one half order of magnitude) because the velocity term is squared.

4.4.5. Particle motions and magnitude calculations

Particle motion analysis of 3-component data showed that the block-and-ash flows are comprised of both body and surface waves, including Rayleigh waves, (fig. 4.7) with both surface waves and body waves present in highest amplitudes. Because body waves are present in the peak amplitudes of the flow events it is possible to calculate local (Richter) magnitudes for the events. M_L was originally derived for earthquakes, however, so it still may not be suitable for use with non-earthquake signals. In practice, M_L is routinely applied to non-earthquake seismic signals such as quarry blasts. It is a convenient way to characterize the "size" of an event for comparative purposes, regardless of the mechanisms causing the event. Because of their emergent onsets and irregular wave trains, as well as the high background signal level at this time, the rockfall signals cannot be located by

traditional means, such as P- and S-wave arrival times. However, the locations can be estimated from the low light camera data. Rockfalls and block-and-ash flows are moving sources that do not have one set location, so for the purposes of the magnitude calculations the center of the image of the block-and-ash flow on the low light camera was used as the location. Errors depend on the travel distance of the rockfall, but the overall run-out distances are small enough that errors will not greatly affect the magnitude calculations. Magnitudes were obtained from the location program HYPOELLIPSE (Lahr, 1999), by picking synthetic P- and S-wave arrivals using the seismic data analysis program XPICK (Robinson, 1990) that corresponded with the locations seen in the images. Although only 9 of the roughly 70 block-and-ash flow events could be located this way, magnitudes for the rest of the events were calculated from a linear fit of maximum amplitudes to the local magnitude calculated with HYPOELLIPSE. This is justified because locations were known, the stations were the same, and the frequency contents and waveforms were similar. Magnitudes ranged from 0.1 to 1.1.

4.4.6. Seismic energy release and seismic efficiencies

To determine the seismic energy release we use the empirical Gutenberg-Richter relationship (Richter, 1958):

(1) $\text{Log } E = 9.9+1.9M_L-0.0024M_L^2$

HYPOELLIPSE gives local magnitudes, and therefore Equation (1), which is based on local magnitudes, was appropriate. The seismic energy was compared with the kinetic energy of the flows calculated from the video. Table 1 shows the estimated seismic efficiencies for the nine flow events that occurred on February 8, 2006. The average seismic efficiency for the block-and-ash flows calculated by empirical M_L energy is 7.6×10^{-4} %, much lower than the typical value for earthquakes of 1%. No correlations between seismic efficiency and other characteristics, such as magnitude, surface area, run-out distance, or duration, were found. Most likely the seismic efficiencies are low because of poor coupling between the flow material and ground.

4.4.7. Duration magnitudes, energy and seismic efficiencies

Because the seismic waveforms of the flow events generally have long durations and small amplitudes, the duration magnitudes were also calculated, to explore the possibility that they are a better representation of the rockfalls' size than amplitude based local magnitudes. The duration magnitudes M_C were calculated using the equation from Lee et al. (1972):

$$(2) \qquad M_C = -.87 + 2.00 \log(\tau) + .0035\Delta$$

where τ is the duration in seconds and Δ is epicentral distance in km. Because the distances are so small, the final term that considers epicentral distance is negligible.

Using durations results in systematically overestimated magnitudes that ranged from 1.5 to 3.4, and did not vary with rockfall sizes as estimated from video, or with run-out distances or seismic amplitudes. The energies were calculated using the Gutenberg-Richter equation (Richter, 1958):

$$(3) \qquad \log E = 9.9 + 1.9 * M_C - (0.024 * M_C^2)$$

Note that this is the same formula as equation (1) but substitutes M_C for M_L. Energies calculated from duration magnitudes may be better representations of the energy put into the ground from the traction and momentum transfer of the material as it moves down the volcano's flanks; however, duration magnitudes do not seem to be useful in distinguishing between the flow sizes as they appear on video. Because the majority of events had small amplitudes and long codas, the energies calculated from duration magnitudes are probably also overestimated. An alternative energy estimation is to take the sum of several shorter duration events that add up to the duration of the longer events to give an equivalent magnitude. The last column in Table 1 shows the seismic efficiencies calculated from such equivalent duration magnitudes. These seismic efficiencies (which have an average value of 2.8 %) are much higher than the M_L–based energy estimations of seismic efficiency and are much closer to the typical seismic efficiencies for earthquakes (1%).

The duration magnitudes were not found to correlate with any measured rockfall characteristics; therefore, using the seismic amplitudes or the M_L and

empirical energy calculations for such comparisons is preferred. Another quantity, the dimensionless seismic energy, which is derived directly from the seismic waveforms by summing the squares of the signal amplitudes and dividing by the sampling frequency, was calculated next in order to better determine relative energies. The dimensionless energy is useful for relative comparisons, but lacks physical units. Plotting the dimensionless seismic energy against the calculations of the M_L energy release shows a significant linear fit (fig. 4.8). This shows that amplitudes, energies determined from M_L, and dimensionless seismic energies are well correlated with each other. These quantities give comparable results when compared with other rockfall characteristics.

4.4.8. Surface areas

Although volume estimates were needed to calculate seismic efficiencies, many uncertainties and sources of error were present in these calculations. This necessitated finding another way of measuring the size of the flows. Because the camera images are two-dimensional, surface areas are used as proxies for size. For consistency, the surface area is estimated by counting the number of pixels above a certain brightness level. The cutoff brightness level was chosen to include the majority of the pixels making up the block-and-ash flow in the low-light image, while excluding some of the edge-pixels which begin to blend in with the cooler background (see Sentman et al., 2010, for discussion of the camera characteristics). The images used in these calculations all came from a single night of recording, so

the camera settings are consistent from image to image. The surface areas show a linear correlation with the seismic amplitudes at station AUE (with r^2 values of 0.60 and 0.62) (fig. 4.9 A-B). These results are consistent with the work of Norris (1994). There was a similar correlation between surface area and the dimensionless seismic energy, (fig. 4.9 C-D), but the correlation with the empirical energy (fig. 9 E-F) does not appear to hold. Scatter in these plots comes from various factors. First, because the images are two-dimensional, the third dimension necessary to finding the true volume of the flows is missing. Second, projections of pixels from camera images onto 3D volcanoes have been done (e.g. Dehn et al., 2002) and have found a difference in area/volume calculations of about a factor of 2. Third, seismic efficiencies also vary for the events. This means that different percentages of the total energy for each flow contribute to the seismic energy.

4.4.9. Durations

Durations were calculated for the flow events from the seismic data. Seismic durations range from 15 to 105 s. Durations were calculated for events that were not overlapping in time; however, the seismic background level was fairly high during the period of dome growth and collapse, which could lead to errors in determining the start and end times of the seismic signals. Seismic durations were estimated with an uncertainty of about 10 seconds, or about +/- 5 seconds at each end. Seismic durations were then compared with durations seen from the camera images. The camera images were taken at 15 second intervals, which could produce a maximum

of 30 seconds of error, as discussed previously. Nevertheless, the ranges of durations of the data are sufficiently large to give meaningful results. Figure 4.10 shows a plot of the seismic durations compared with the flow durations seen in the video, for 24 of the February 8th flow events. Longer lasting events on the video were expected to produce longer lasting seismograms and in general this is seen to be the case. Therefore the duration of the flow event can be estimated from the seismic signal.

4.4.10. Run-out distances

Next we compared the distances traveled by the flows with several parameters. The run-out distance was plotted against the seismic amplitude (fig. 4.11A), the dimensionless seismic energy (fig. 4.11, B-C), and the empirical seismic energy (fig. 4.11, D-E). The flows going to the north travel farther and have more variation in the distances traveled. These north-bound flows with the largest run-out distances are also more energetic than the northeast ones, according to figures 4.11, b-e. These relationships hold despite the large amount of scatter observed. The scatter is highest for small energy values.

4.5. Changes in azimuth of arrival

As the block-and-ash flows move down the slope of the volcano, the angle at which the waves arrive at a seismic station on the flank should change, since the flow is a moving source. Station AU14 is the only station used for this analysis as it

was the broadband station closest to the block-and-ash flows (fig. 4.1). Other broadband stations were not close enough or did not provide clear enough signals for the analysis. To determine if the change in azimuth of arrival is observable, the horizontal components of particle motion were plotted against each other. Figure 4.12A shows the seismogram of the flow event used for this analysis. This event traveled down the northern slope and had a duration of about 55 s. Figure 4.4A shows the low light camera image of the event after traveling its maximum distance (as well as it can be seen given the resolution of the camera).

This analysis uses unfiltered seismic data from broadband station AU14. For several different times throughout the time series, indicated by the numbers on figure 4.12A, the north component (AU14 HHN) and east component (AU14 HHE) have been plotted against one another. Frequencies of about 3 Hz were typical for rotations when they occurred, so the data were plotted in sections of 30 data points (~1 cycle) at a time. For each 2-second segment (about 6 cycles) we plot the north-south component versus the east-west component, with the different 30-data point series plotted as different symbols. The plots are essentially map views of the ground motion at the station AU14, and they show both linear and elliptical motion. The plots that show motion ranging from linear to elongated elliptical are the ones used for this analysis. Linear least square fits were applied to the plots to indicate the azimuth of the data and the ones with the higher r^2 values— and therefore higher linearity— were used for each segment. Data from noise caused some irregular signals, but when these are removed, the data series show nearly linear elliptical

motion towards and away from the station AU14 and in a few cases motion perpendicular to the station. The results suggest that waves arrive with varying azimuths. Similar azimuths occur frequently, suggesting several common locations. Once the azimuths of the horizontal ground motions were calculated they were extrapolated from the station back to the flow deposit site. (fig. 4.13) Using the distances and times determined from a map and the seismogram shown in figure 4.12A, the velocities of the flow segments were estimated and are given in figure 4.13. The slowest of these velocities (30 m/s) occurred when the flow was farthest from the summit and agrees with the average velocity calculated earlier (Table 4.1). However, the average of all the velocities calculated from particle motions and azimuth of arrivals is 92.7 m/s, higher than the average calculated from the video. One persistent azimuth appeared to be directed towards the vent and plotting it on the map confirms this (fig. 4.13, inset).

4.6. Discussion

Rockfalls and block-and-ash flows occur frequently at volcanoes and are commonly recorded on seismic data. At Augustine volcano, seismic data are usually the only measurements made of the rockfalls and flows. The installation of the low-light camera in Homer and its recording of the incandescent flows has provided an opportunity to compare the seismic data of them with visual data. The low resolution of the camera, however, makes estimating absolute volumes and absolute locations difficult. The seismic data may still be compared to the relative sizes and

relative distances traveled by the flows. Using surface area for the size, for example, removes the need to guess at a third dimension, although errors will still be introduced by making 2-D estimates of a 3-D shape. Relations vary between surface areas and volumes of different shapes; however, a plot of the estimated volumes (used for seismic efficiencies) and surface area shows a nearly linear correlation with a high r^2 value of 0.77. Assuming that surface area as measured from the low-light camera is a suitable estimate of the block-and-flows' volume, the results of this study agree with Norris, (1994) who found a nearly linear relation between seismic amplitude and source volume for rockfalls.

Because no two flows occur in exactly the same way, many differences in seismic signals, originating from different motions, can be expected. The coefficient of friction will vary depending on the mechanism of motion and shape of material that is falling. Therefore the amount of energy put into the ground can vary depending on the block motions, such as whether they are sliding, rolling or freefalling. Sliding blocks are traction events, and freefalling or bouncing rocks are cases of momentum transfer. The mechanisms of motion will also affect whether calculating M_L for the block-and-ash flows is valid. The M_L scale was developed for shear fracture events, and this assumption is not met for landslide events. However, if the mass in the block-and-ash flow is sliding over the ground, it creates the traction similar to a shear fracture event. Rolling rocks would not create the same motion. For the flow events in this study, it has not been possible to determine which type of motion is occurring, but differences in durations, amplitudes, and onset

characteristics may be explained by different flow mechanisms. Particle size distribution and the terrain over which the flow travels should also affect these characteristics. According to Cole et al. (2009), decreased seismic amplitudes can be caused by the presence of unconsolidated deposits from previous flows that are in the flow path. The attempts to quantify the rockfalls may not have been successful for determining absolute sizes, but have still provided useful results regarding relative sizes, i.e. figure 4.9. Relative measurements are still useful, because relations between quantities such as size, energy, run-out distance seismic amplitudes can be determined. Systematic relations were found between seismic amplitudes/energies and surface areas (fig. 4.9), seismic and video durations (fig. 4.10), and seismic amplitudes/energies and run-out distance (fig. 4.11). Relationships with seismic amplitudes are preferred over root-mean-squared amplitudes and magnitudes because they are the easier measurement to make, and can be done in real-time.

In calculating the seismic efficiencies, we determined what portion of the total energy went into the ground as seismic energy. Because the run-out distance and durations had already been measured from the low-light camera, and because more uncertainties were involved in calculating the potential energy, kinetic energy was calculated as the total energy of the flow events. The kinetic energies may be lower overall than potential energy estimates due to friction and heat loss. The results of two methods (local magnitudes and duration magnitudes) of calculating seismic energy (not including dimensionless seismic energy) are given in Table 1. Seismic efficiencies for the flow events that were calculated with local magnitudes

were much lower than the efficiencies calculated with duration magnitudes, and closer to those values found by Vilasojana et al. (2008). Although the efficiencies calculated with duration magnitudes were much closer to those quoted in Scholz (1990) for other seismic events (1% for events such as earthquakes, nuclear explosions, and quarry blasts), and Deparis and Jongmans (2008), they may be overestimated due to the fact that the flows are gravitational in nature. We infer that the low estimates of < 1 % are most representative of the surficial processes observed, because there is likely to be poor coupling between hot block-and-ash flow and the loose ground material.

Although the dome growth and collapse period produced thousands of flows throughout the eruption, and although the low-light camera was recording for several nights, only a limited time was suitable for joint analysis with seismic data. In some periods too many flows occurred too closely together to distinguish between them in the seismic data, or the seismic data were clipped on short period stations. In order to record the block-and-ash flows well, the stations needed to be relatively close such as stations AUE and AUW, however, closer stations tended to clip. This study was also limited by the number of seismic stations on the volcano as well as their locations. Greater coverage of the island with short period and broadband seismometers would improve the ability to locate flows based on seismic amplitudes, as would higher resolution video or photographic recording. Broadband stations closer to the summit would be necessary to analyze the seismic waves closer to the events or summit. The addition of the campaign broadband stations helped with the

particle motion analysis; the close location of AU14 made it the most suitable to use for analysis.

4.7. Conclusions

The recording of the 2006 flow events with the low-light camera provided an opportunity to verify and quantify block-and-ash flow events and to make direct comparisons between seismic and visual observations. Several different measurements and calculations of amplitude and energy were done to compare with flow characteristics. Peak-to-peak seismic amplitudes are the fastest and simplest measurements that can be made during real-time monitoring, so these were first compared with block-and-ash flow characteristics such as surface area, run-out distance, and direction. The peak-to-peak amplitudes and dimensionless seismic energies correlated best with run-out distance and relative surface area.

In general, seismic amplitudes, energies determined from M_L, and dimensionless seismic energies are all highly correlated with each other, and give comparable results when compared with block-and-ash flow characteristics. Duration magnitudes did not vary enough to compare with these measurements.

The images provided by the low-light camera were found to have too many sources of error to be used for precise volume and mass estimations; however, they were still helpful in determining locations, run-out distances, relative sizes, and relative seismic efficiencies of the flows that occurred during the continuous and effusive stages of the eruption. Durations, run-out distances, and surface areas

correlate with varying degrees of errors with seismic data. Together these observations suggest that seismic data may be used to estimate relative sizes and locations of block-and-ash flows, both of which are useful to characterize hazards.

Surface waves, including Rayleigh wave motion, as well as body waves were present in the block-and-ash flow seismograms. Particle motions also showed that the events are acting as moving sources with different azimuths of arrival through time. Estimates of the velocities of the flows were made by tracing the azimuths of arrival at different times back to the apparent source at several times and calculating the distance traveled between each. The velocity estimates show the flows first increasing and then gradually decreasing in speed. This agrees with the shape of the volcano; the upper slopes are steep whereas the lower slopes are more gradual.

The 2006 Augustine eruption was marked by the occurrence of thousands of rockfalls and block-and-ash flows. Despite the fact that the rockfalls and flow event signals formed the bulk of the seismic signals from the 2006 Augustine eruption, they have been previously understudied. Seismic analysis of flow events can provide hazard monitoring information on directions, durations, sizes and run-out distances. Although the seismic energies of the flow events were low, the low seismic efficiencies and high event numbers made mean that a tremendous amount of volcanic energy was released through the flow events. While the novelty of this study is the introduction of the low-light camera, a side benefit of having the visual data provides confirmation that seismic data alone can track the course of the eruption.

Acknowledgements

We thank S. Stihler for the help in identifying rockfalls, G. Tytgat for assisting with creating the low-light camera videos and helping with troubleshooting, and H. Buurman and M. West for use of their figures. This work was partially supported by the Alaska Volcano Observatory and the U.S. Geological Survey (USGS), as part of their Volcano Hazards Program, and by additional funds by the State of Alaska and the University of Alaska Fairbanks Geophysical Institute.

Table 4.1. Magnitude, energy, and seismic efficiencies for 9 block-and-ash flows.

Event Time UT (AKST)	Mag[1]	Emp.[2] Mag. Eng (J)	Equiv.[3] D_{MAG} Eng (J)	Corr.[4] Mass (kg)	Avg.[5] Velocity (m/s)	Kinetic[6] Energy (J)	Seis. Eff.[7] (from M_L) (%)	Seis. Eff.[8] (from D_{MAG}) (%)
8:44 (11:44 pm)*	0.4	$4.5x10^3$	$3.0x10^7$	$1.4x10^7$	15.96	$3.6x10^8$	$1.3x10^{-3}$	8.4
9:28 (12:28 am)	0.7	$1.7x10^4$	$1.3x10^7$	$1.5x10^7$	52.01	$6.0x10^9$	$2.8x10^{-4}$	0.2
9:56 (12:56 am)	1.1	$9.1x10^4$	$1.3x10^7$	$2.3x10^7$	52.01	$4.3x10^9$	$2.1x10^{-3}$	0.3
10:05 (1:05 am)	0.9	$3.9x10^4$	$1.7x10^7$	$1.4x10^7$	97.85	$2.3x10^9$	$1.7x10^{-3}$	0.7
12:17 (03:17 am)*	0.1	$1.2x10^3$	$8.7x10^6$	$2.5x10^6$	29.90	$1.4x10^9$	$8.6x10^{-5}$	6.2
12:33 (3:33 am)	0.2	$1.9x10^3$	$3.6x10^7$	$5.5x10^6$	40.10	$1.0x10^9$	$1.8x10^{-4}$	3.4
12:34 (03:34 am)*	0.2	$1.9x10^3$	$3.6x10^7$	$8.2x10^6$	30.36	$1.3x10^9$	$1.5x10^{-4}$	2.8
13:30 (4:30 am)	0.9	$3.9x10^4$	$1.3x10^7$	$2.4x10^7$	31.29	$4.5x10^9$	$8.8x10^{-4}$	0.3
13:59 (04:59 am)*	0.2	$1.9x10^3$	$3.6x10^7$	$3.6x10^6$	17.18	$1.1x10^9$	$1.7x10^{-4}$	3.2

*Denotes events traveling to the northeast

[1]Local magnitude

2Empirical Magnitude was calculated from Equation 1

[3]Empirical equivalent duration magnitude energy was calculated from Equation 1

[4]Corrected mass, obtained from video assuming $V=(4/3\pi ab^2)/2$, using a rock density of 1670 km/m^3, and then dividing by a correction factor of 740

5Average velocity was calculated from video run-out distance and duration.

6 Kinetic Energy was calculated with half-ellipsoid volume assumption using $KE=1/2mv^2$.

[7]Seismic efficiency from empirical ML energy was calculated by ratio of Column 3 (Emp. Mag E) / Column 7 (KE) x100%

[8]Seismic efficiency from empirical duration magnitude energy, calculated by ratio of Column 4 (Equiv D_{MAG} E)/ Column 7 (KE) x100%

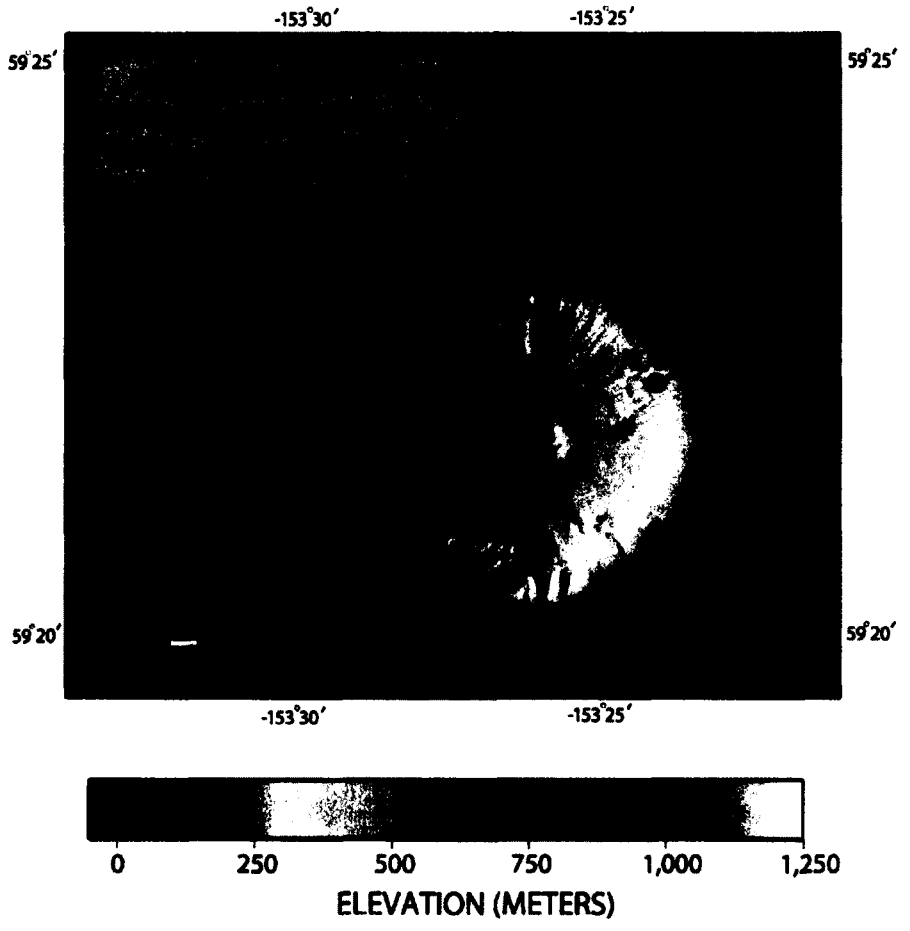

Figure 4.1

Map showing the seismic stations at Augustine. The telemetered seismic stations and campaign broadband seismic stations have blue and red labels, respectively. Except for AUL- which is broadband- all of the telemetered stations are short period stations. AUP, AUH, AUR, AUS, and AUL were all damaged or destroyed during the eruption. Since then, AUL, AUP and AUH have been repaired. The lowlight camera in Homer is 112 km to the east of Augustine. The black arrow on the figure points in the direction of the camera. (Figure courtesy of H. Buurman.)

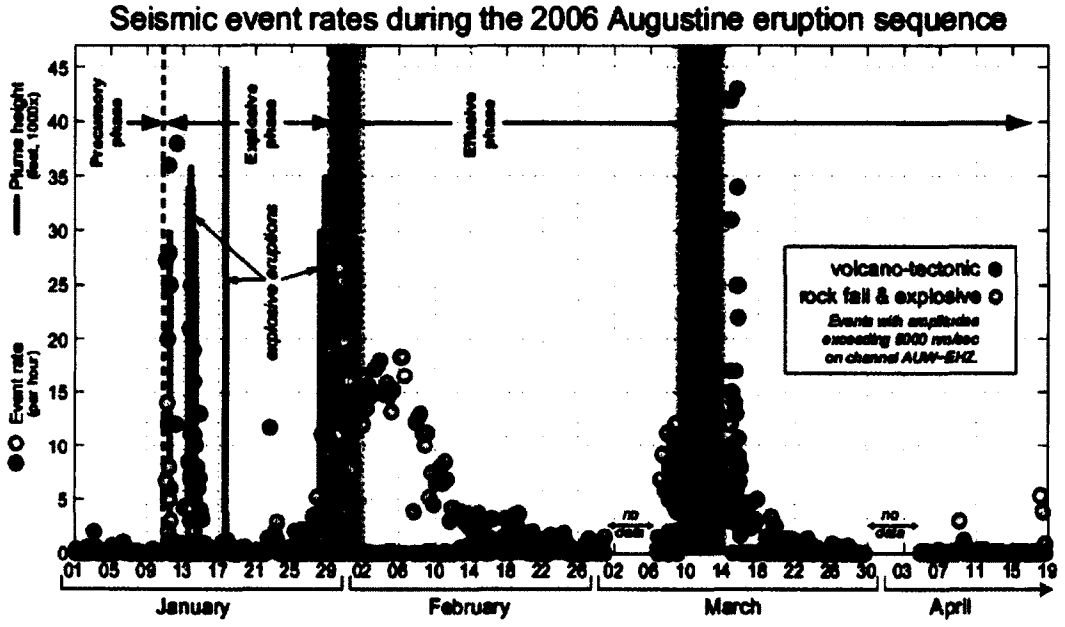

Figure 4.2

Daily counts of seismic events during 2006 Augustine eruption. The dots represent the event rate per hour of rockfalls/ explosions and earthquakes. Events that are likely rockfalls or explosions are labeled with yellow dots. Located earthquakes are red dots. Explosions are indicated by vertical bars. The peak in early February shows these types of events occurring at rates of up 15-20 events per hour. (Figure courtesy M. West).

Figure 4.3

Lowlight camera image and seismogram of northeast block-and-ash flow. A) A large flow, seen on the low-light camera, going to the northeast (with a smaller component located on the north flank).

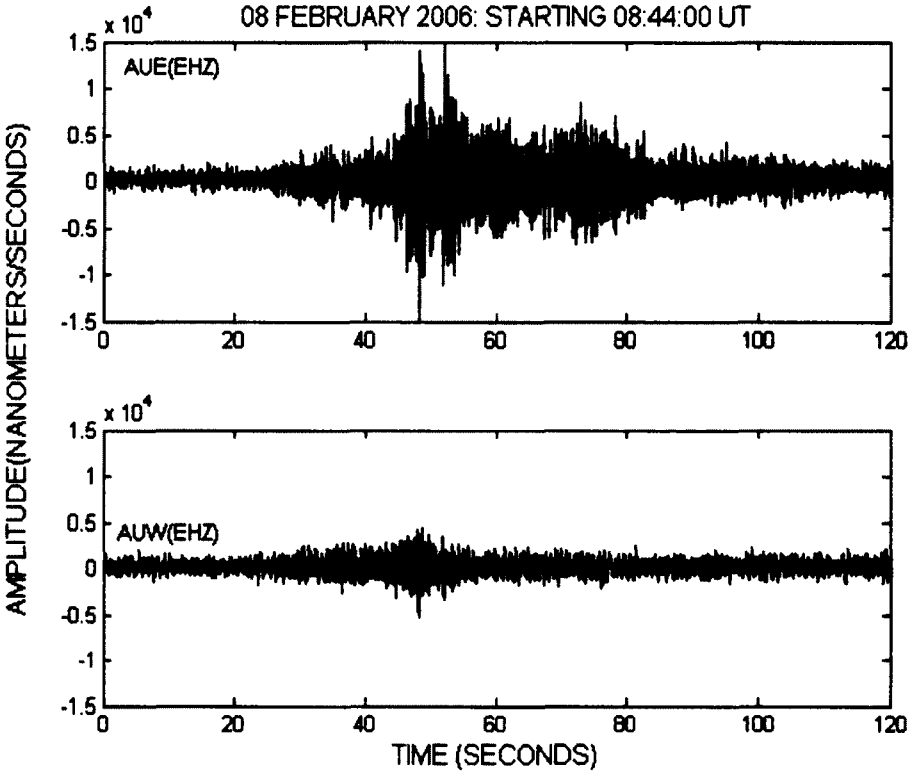

B

Figure 4.3 continued

B) The seismograms originating from the event shown in (A). The amplitude at AUE, on the top, is much larger than that of AUW. A description of the low-light imaging system used to obtain these images is given in Sentman et al. (2010).


A

Figure 4.4

Lowlight camera image and seismogram of north block-and-ash flow. A) A large block-and-ash flow, seen on the low-light camera, going to the north.

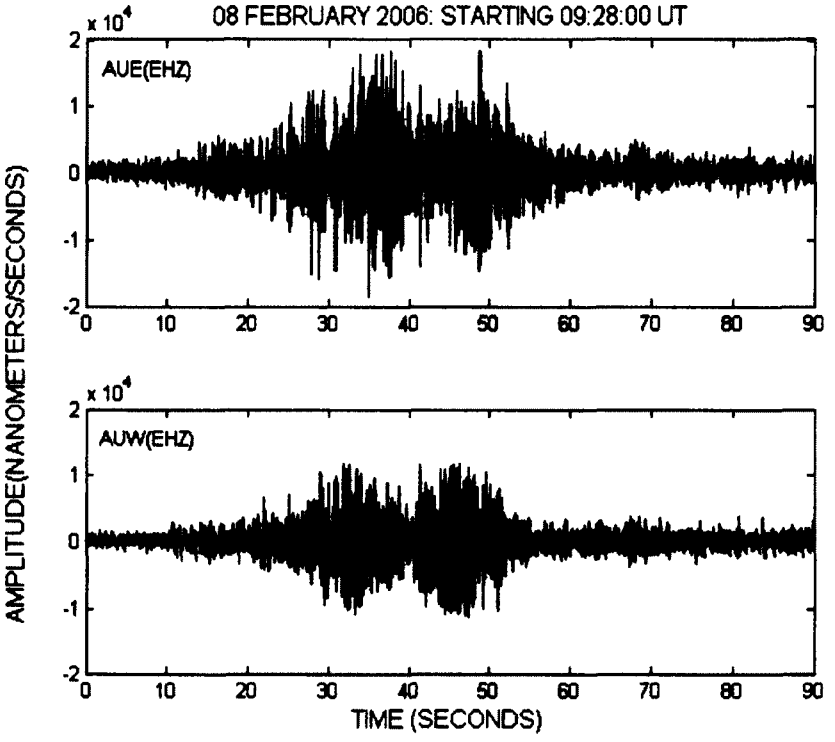

B

Figure 4.4 continued

B) The seismic traces corresponding with the flow in (A). The seismic trace for AUE is on the top, the trace for AUW is on the bottom. The amplitudes at the two stations are similar. A description of the low-light imaging system used to obtain these images is given in Sentman et al. (2010).

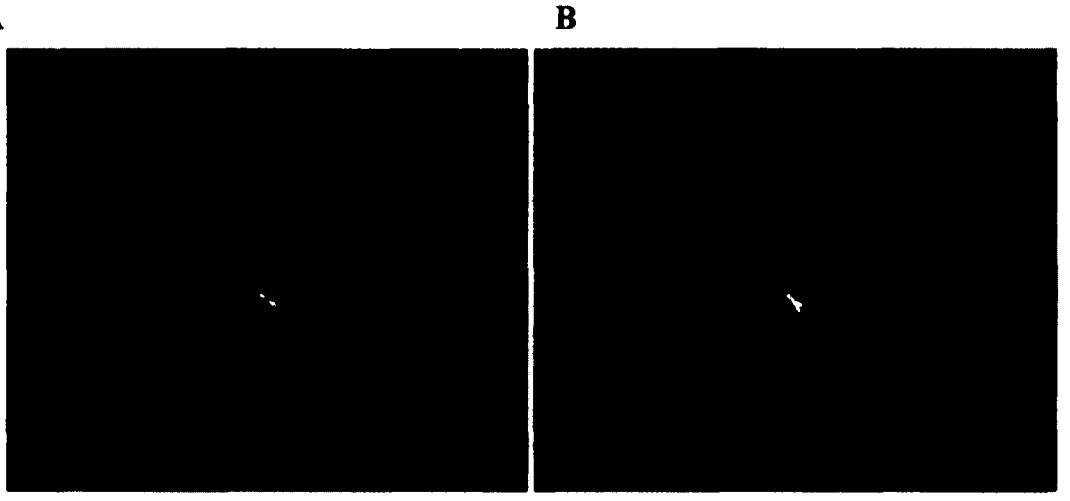

Figure 4.5

Lowlight camera images and seismograms of two block-and-ash flows . The two events occurred within a 5 minute time period. A) Image of a flow going to the north side of the volcano. Its corresponding seismic signal (part C) shows that the seismic amplitude at AUW is higher than that at AUE. B) Image of flow going to the northeast. The amplitude at AUE is higher than the amplitude at AUW.

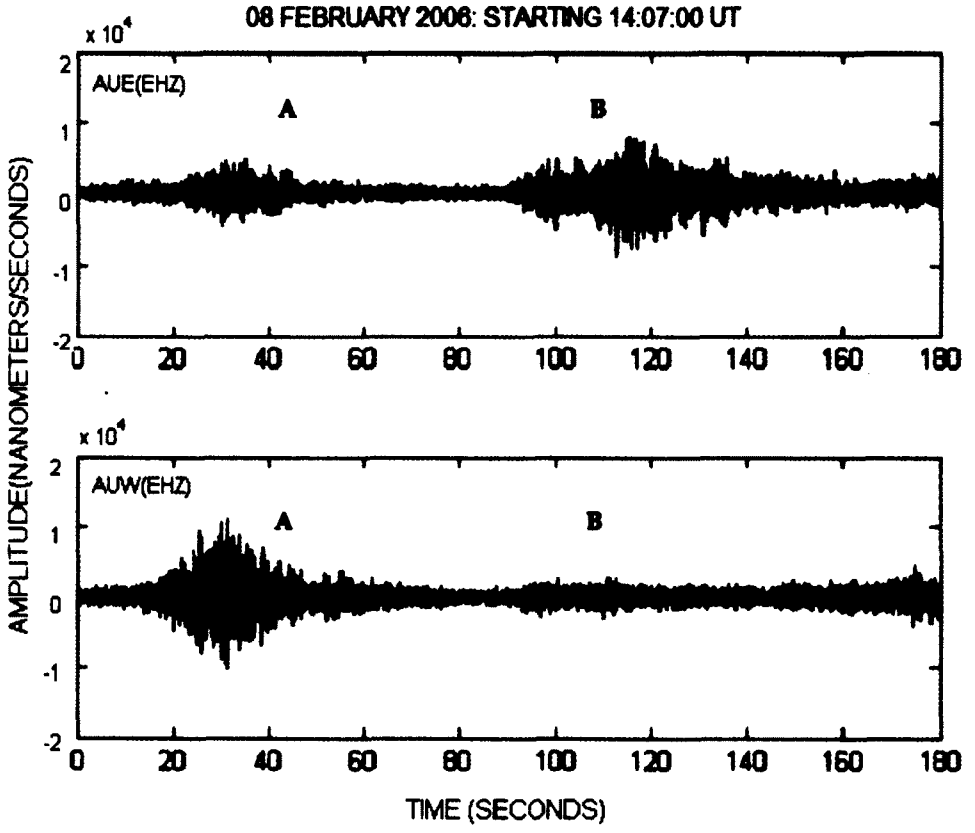

C

Figure 4.5 continued

C) Seismic trace showing the two flows. The amplitude is larger at AUW for the first event when the flow is moving toward the north. The amplitude is larger at AUE for the second event when the flow is moving more toward the east.

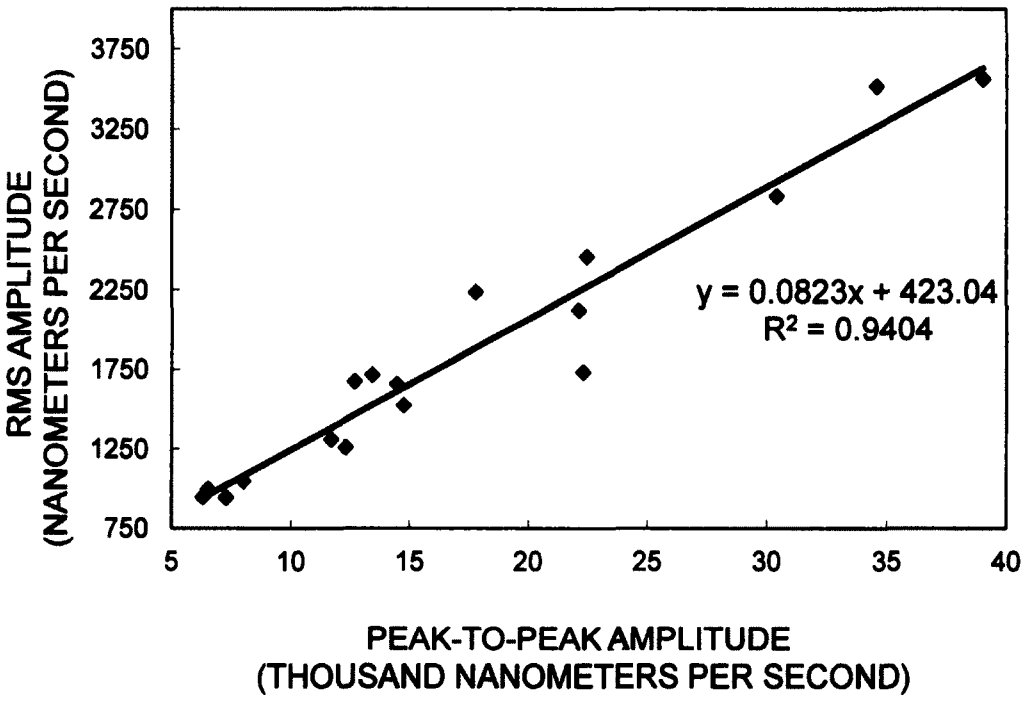

Figures 4.6

RMS amplitudes vs. peak-to-peak amplitudes at AUE . The correlation of the two amplitude measurements suggests that the maximum peak-to-peak amplitude measurements are not contaminated by stray peaks and are suitable for use in magnitude and energy calculations.

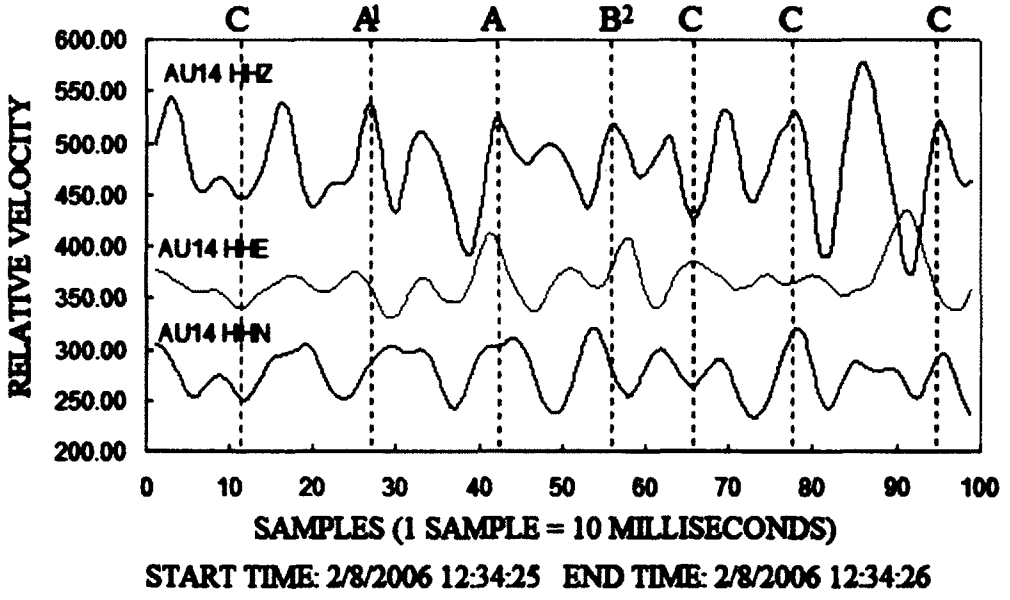

A

Figure 4.7

Three components of broadband seismic data from station AU14. A) One second of data from three components of broadband seismic data from station AU14 on the NE flank (see fig. 4.1). The vertical units are in nanometers per second, but traces have been offset from one another for comparison between components for the purpose of determining particle motion. Sections of the waveforms correspond to Rayleigh waves (A), PL waves (B), or body waves (C). Rayleigh waves seen here are traveling up on the vertical component, while moving north and west simultaneously. The PL wave also moves up on the vertical component, while moving east and south simultaneously. For body waves, the components show rectilinear motion.

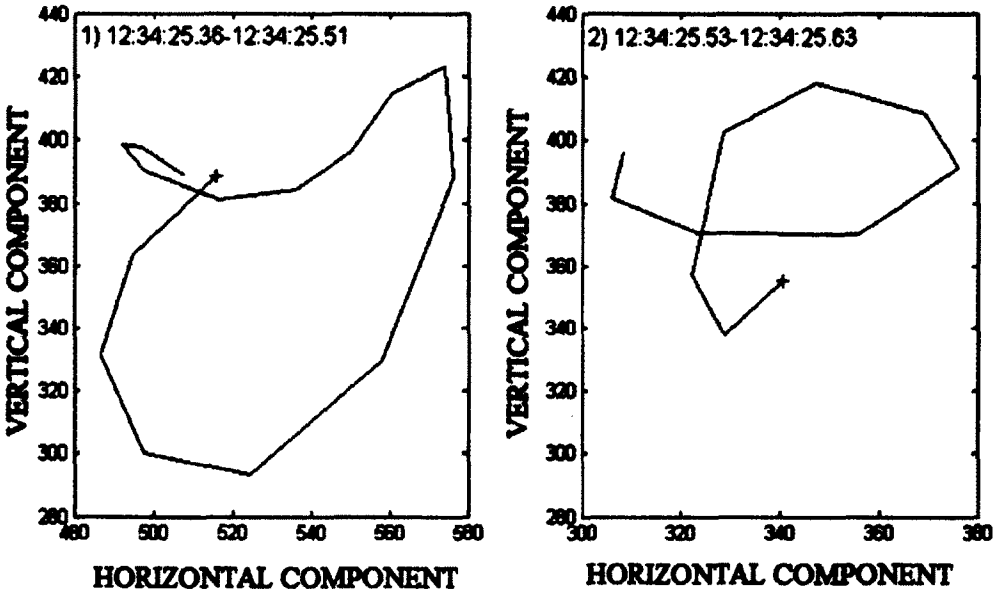

B

Figure 4.7 continued

B) Particle motion plots for two segments of the data shown in A) above, one a Rayleigh wave (labeled A^1 in part A) and one a PL wave (labeled B^2). The plus symbol is the starting point for each case.

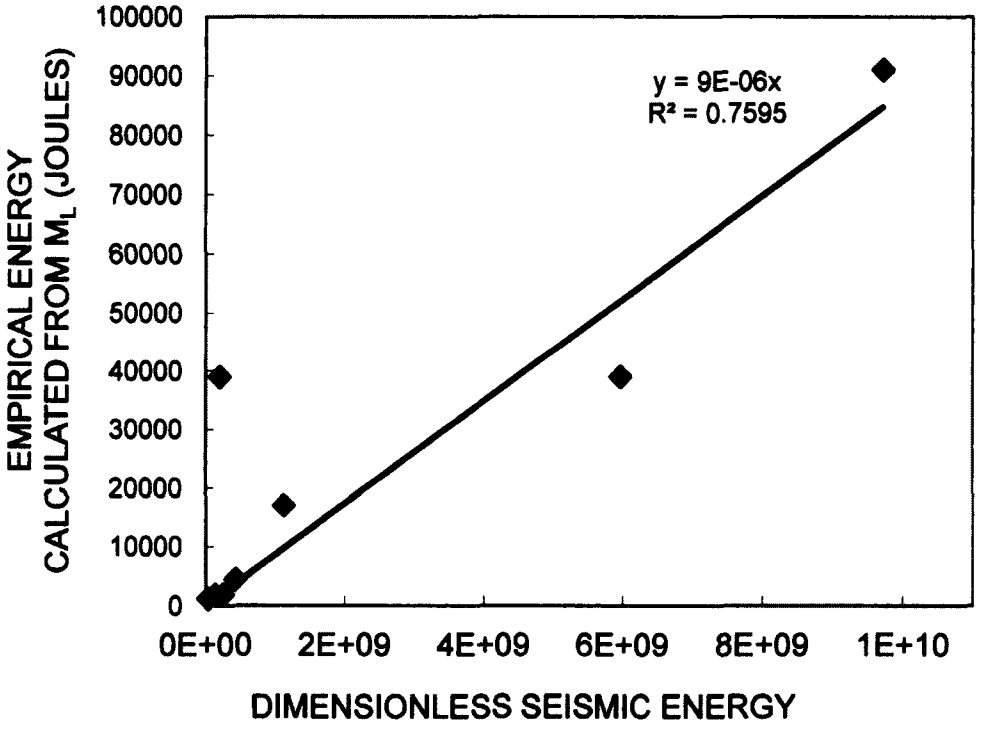

Figure 4.8

Gutenberg-Richter seismic energy vs. dimensionless seismic energy. The empirical energy is calculated from equation (1) using local magnitudes plotted against dimensionless seismic energy. The dimensionless seismic energy is calculated by summing the squares of the seismic signal and dividing by the sampling rate. The strong correlation suggests that it is valid to use the energy calculated from magnitudes for comparison purposes.

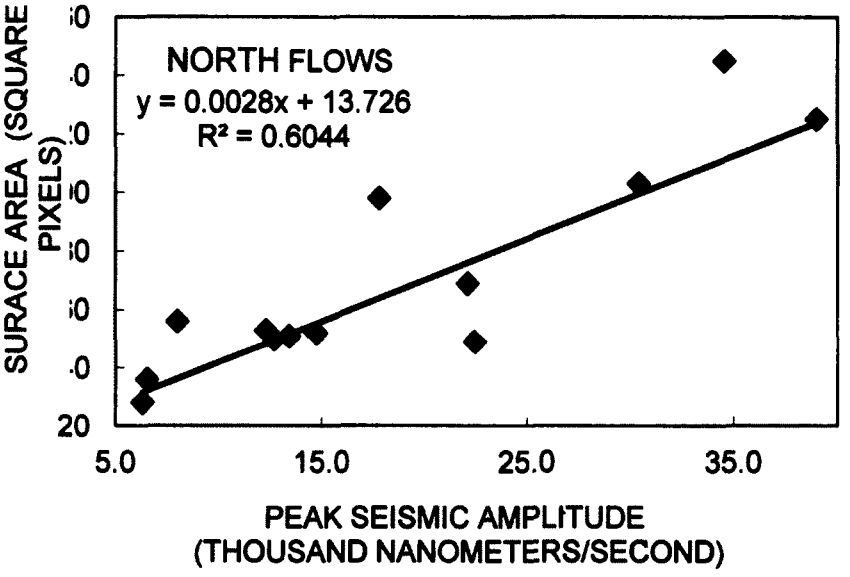

A

Figure 4.9

Surface area vs. seismic amplitudes and energies. The surface area measured for the block-and-ash flows (as observed in the lowlight video images) in relation to (A) peak seismic amplitude at AUE for the north-going flows, (B) peak seismic amplitude for the northeast-going flows, (C) dimensionless seismic energy (calculated directly from the waveforms) for the north-going flows, (D) dimensionless seismic energy for the northeast-going flows, (E) empirically calculated seismic energy for north-going flows, and (F) empirically calculated seismic energy for northeast-going flows. The surface area shows a significant fit with the seismic amplitude and the dimensionless seismic energy, but a weaker correlation with the empirical energy.

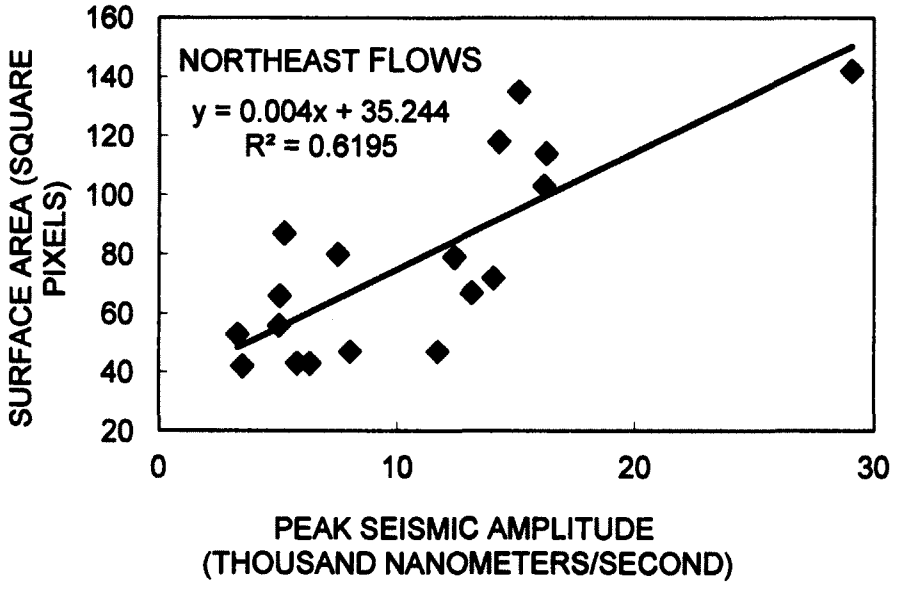

B

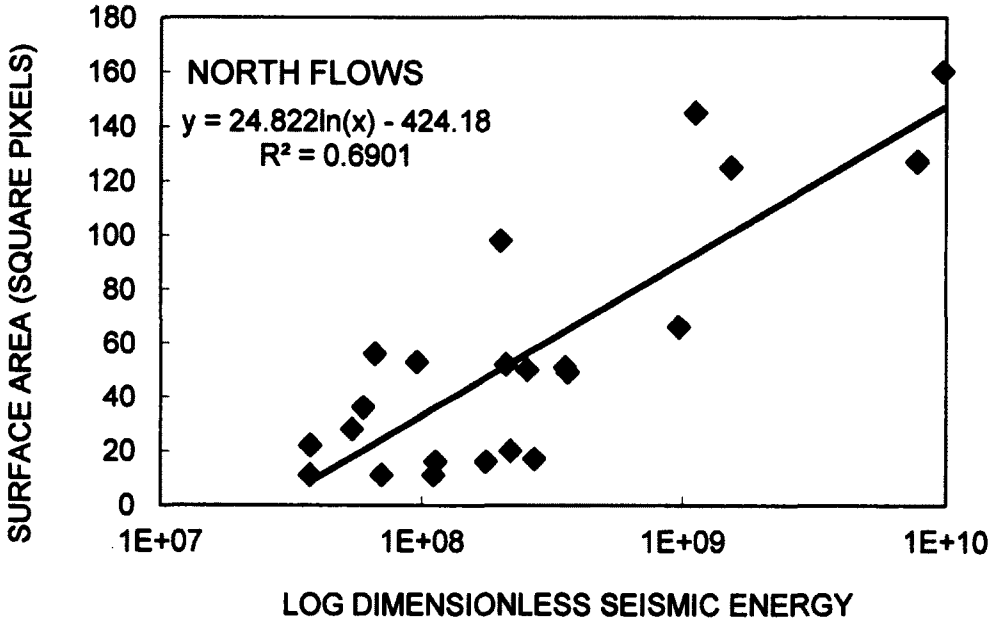

C

Figure 4.9 continued

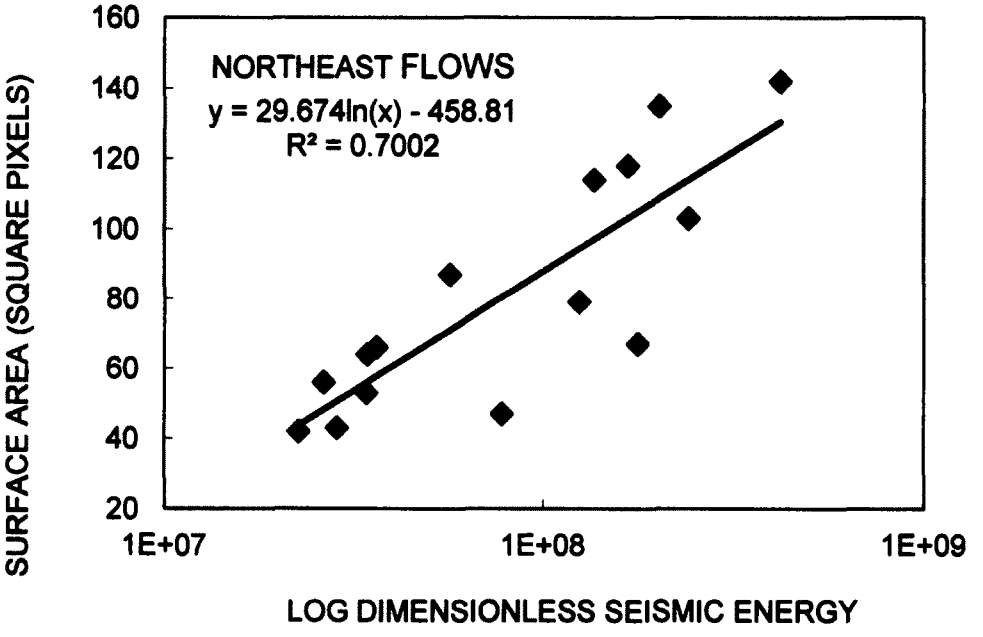

D

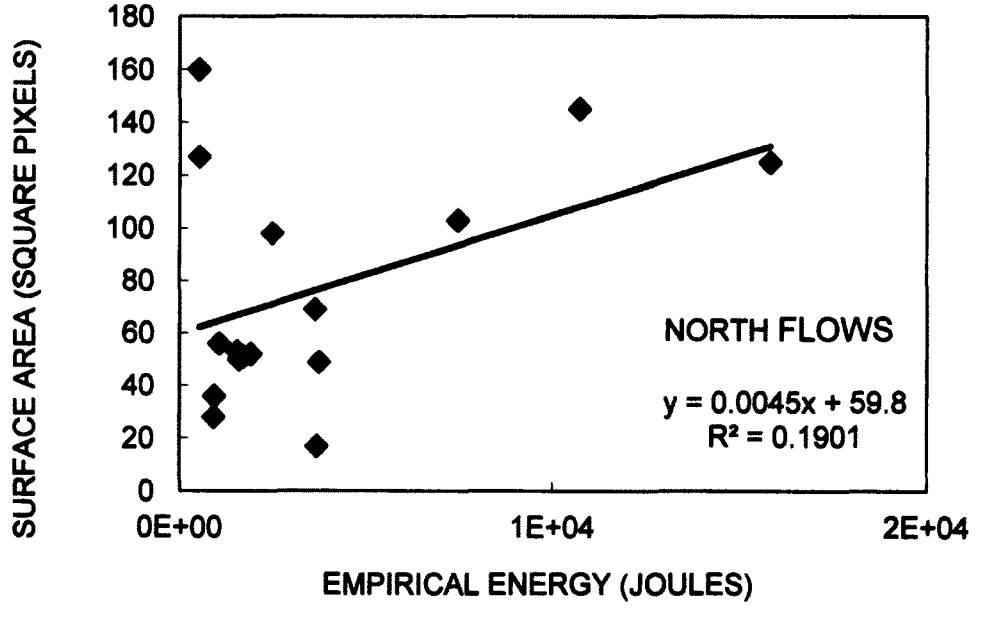

E

Figure 4.9 continued

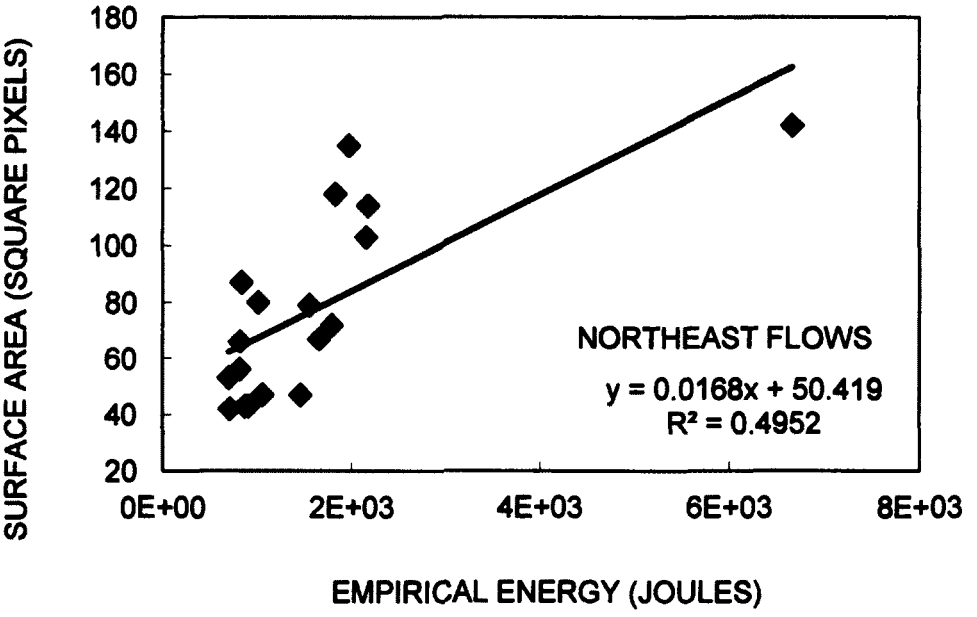

F

Figure 4.9 continued

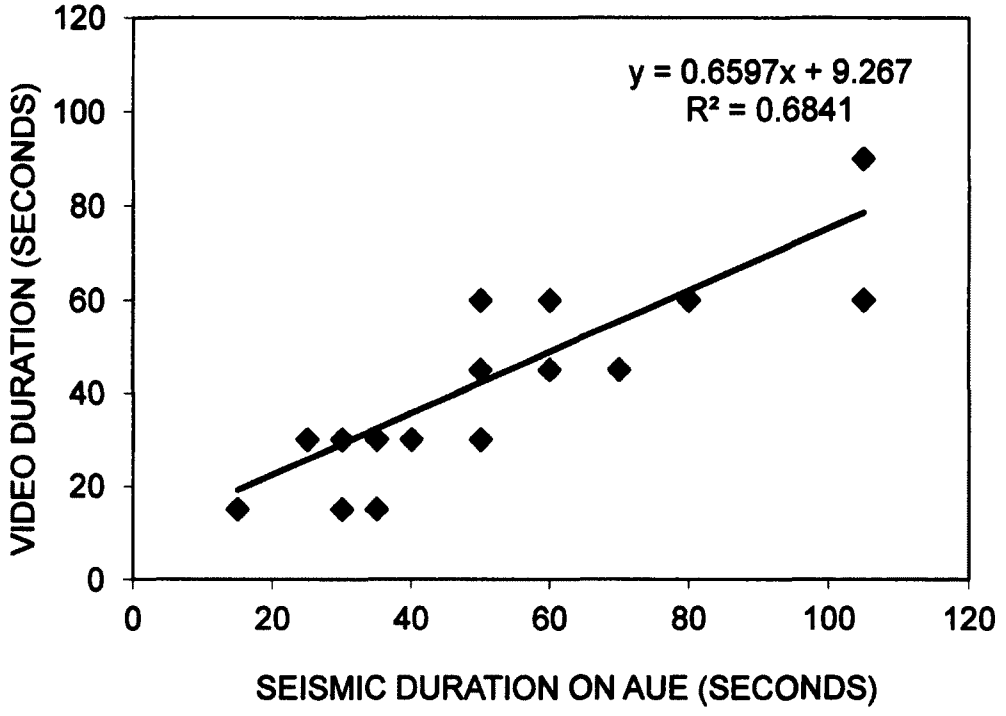

Figure 4.10

Video duration vs. seismic durations. The plot includes 24 isolated (not compound) events. Because the images are 15 seconds apart, the video duration estimates could have a maximum error of 30 seconds, shown by the vertical error bars. Because the seismic data are continuous, they can be used to reliably estimate the flow durations.

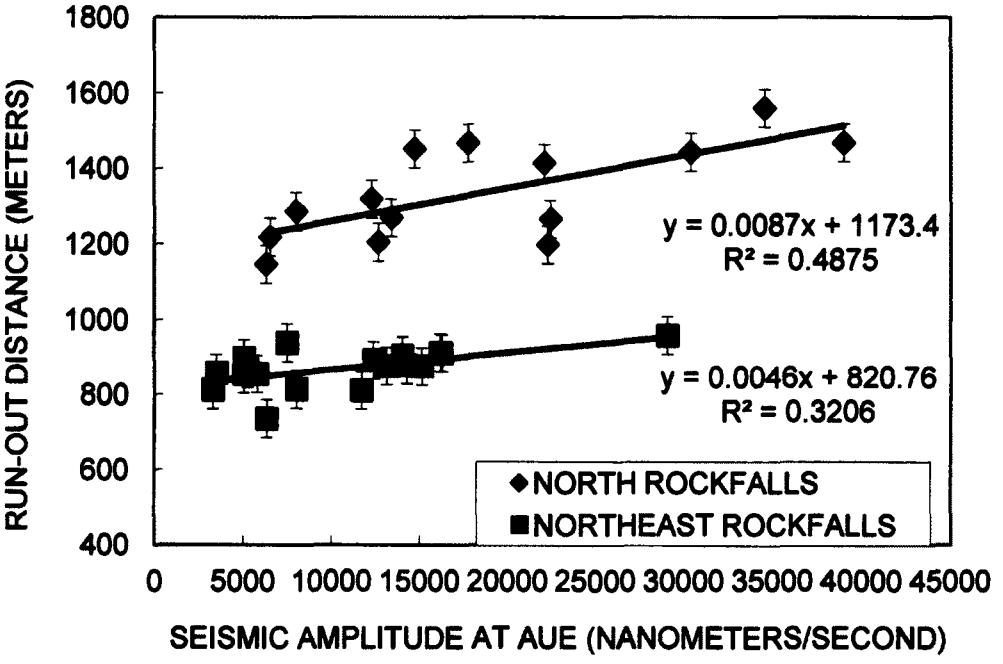

A

Figure 4.11

Run-out distances vs. seismic amplitudes and energies. Maximum distances traveled by block-and-ash flows plotted against: (A) seismic amplitude at AUE for both north and northeast-going block-and-ash flows,(B) dimensionless seismic energy for the north-going flows,(C) dimensionless seismic energy for northeast-going flows,(D) empirical energy for north-going flows and (E) empirical energy for northeast-going flows. Note that the vertical and horizontal scales differ. Runout distances can be estimated from seismic data but with different relationships for different directions. Error was estimated to be about 50 m at both the start and end point of the flow as seen on the video images.

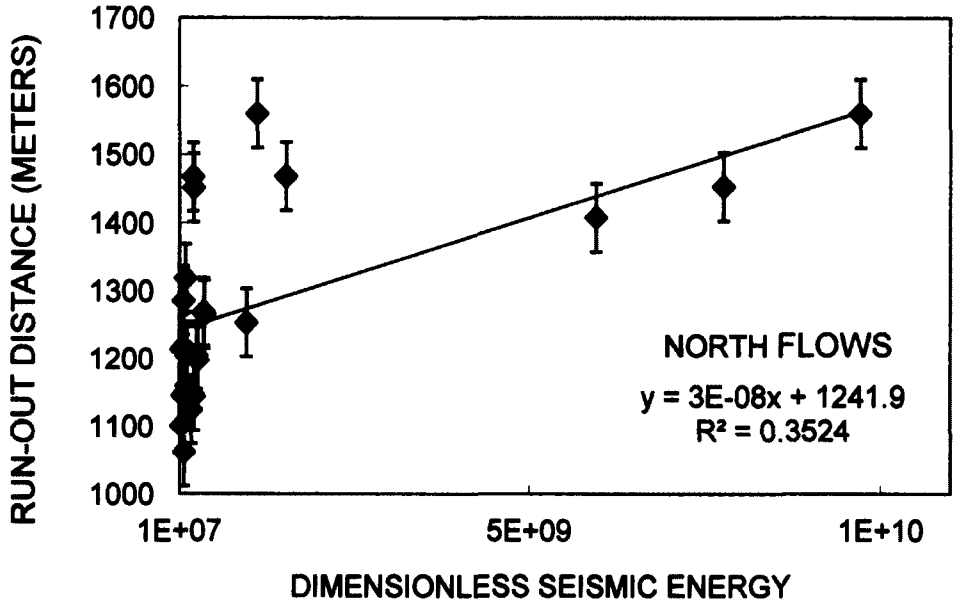

B

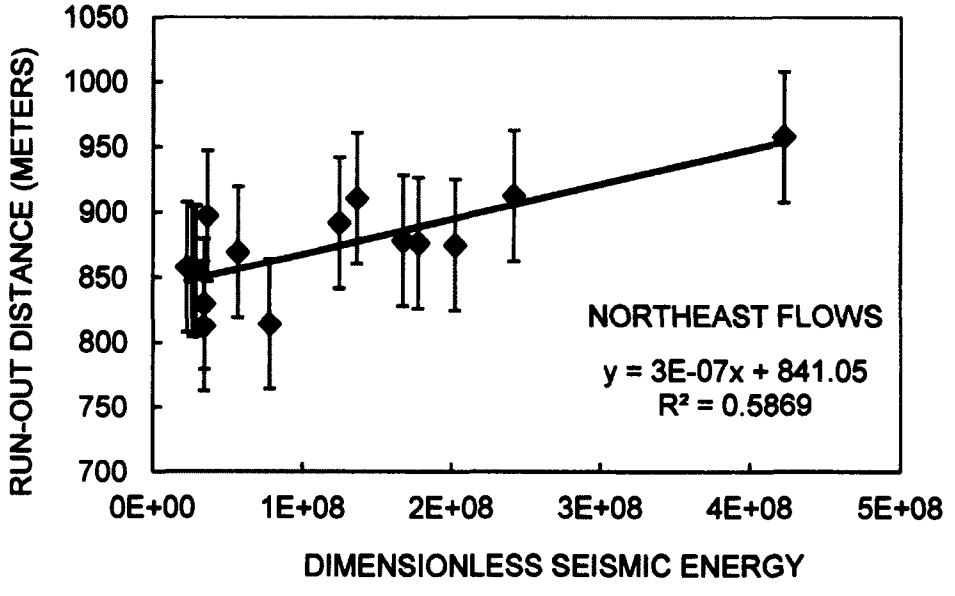

C

Figure 4.11 continued

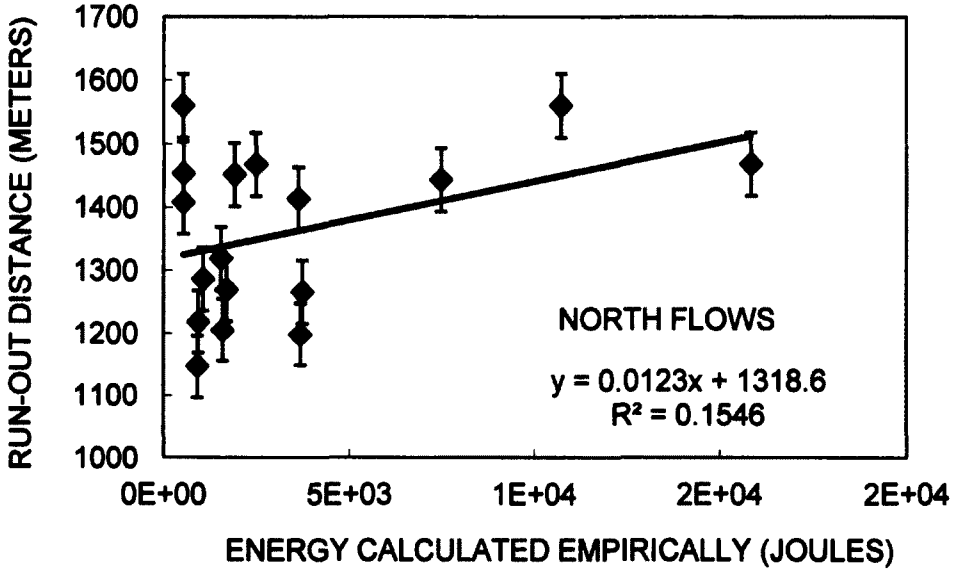

D

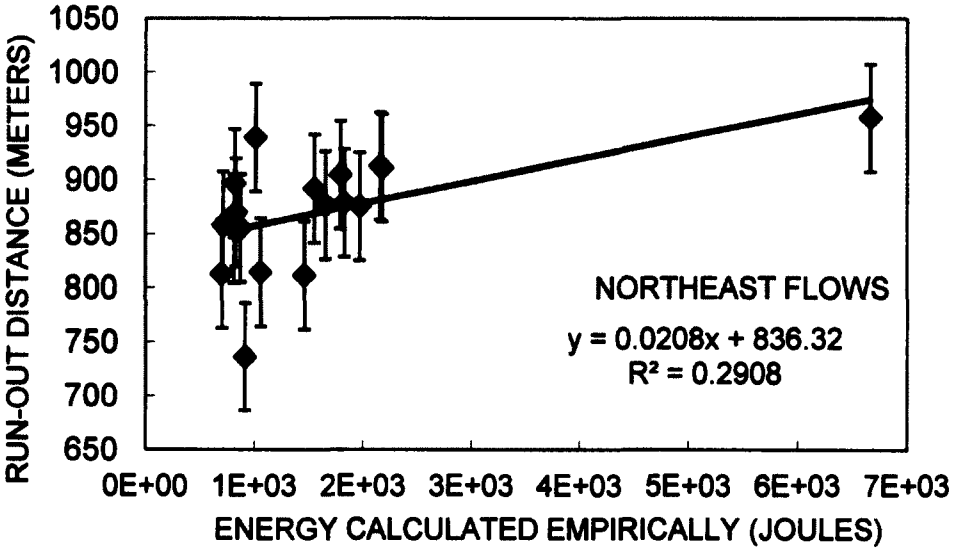

E

Figure 4.11 continued

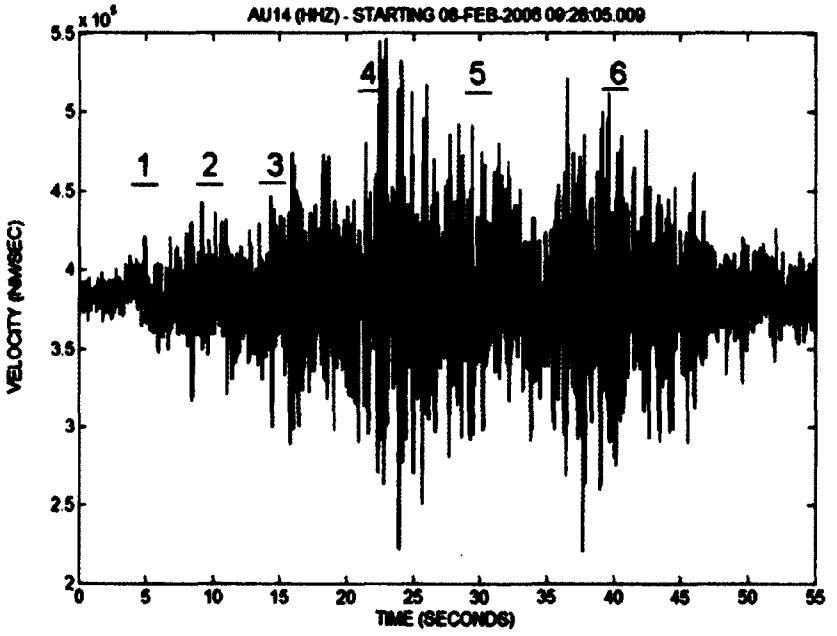

A

Figure 4.12

Particle motions for seismic data from a block-and-ash flow. A) Seismogram for the block and ash flow used in the particle motion analysis. Each number refers to a plot shown in B). B) Horizontal (N-S and E-W) components of particle motions from the segments of seismic data shown in A) plotted against one another. Each plot contains 2 or more series of data consisting of 30 data points each (1 point = .01 s). The plots show motion towards and away from the station AU14 and suggest that some waves are arriving with varying azimuths, and that the event is acting as a moving source. The slopes with dotted lines are shown in figure 4.13A and B as azimuths.

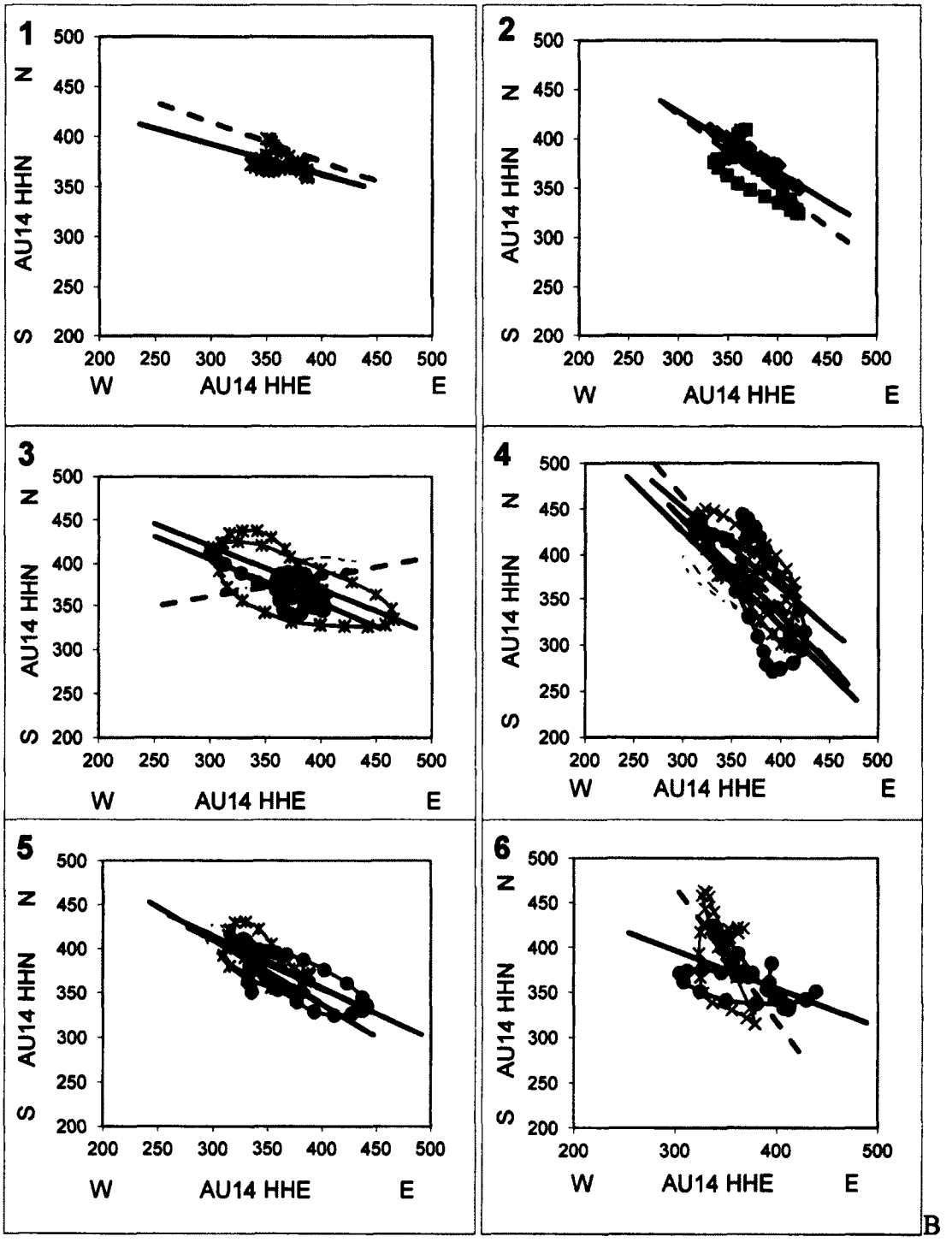

B

Figure 4.12 continued

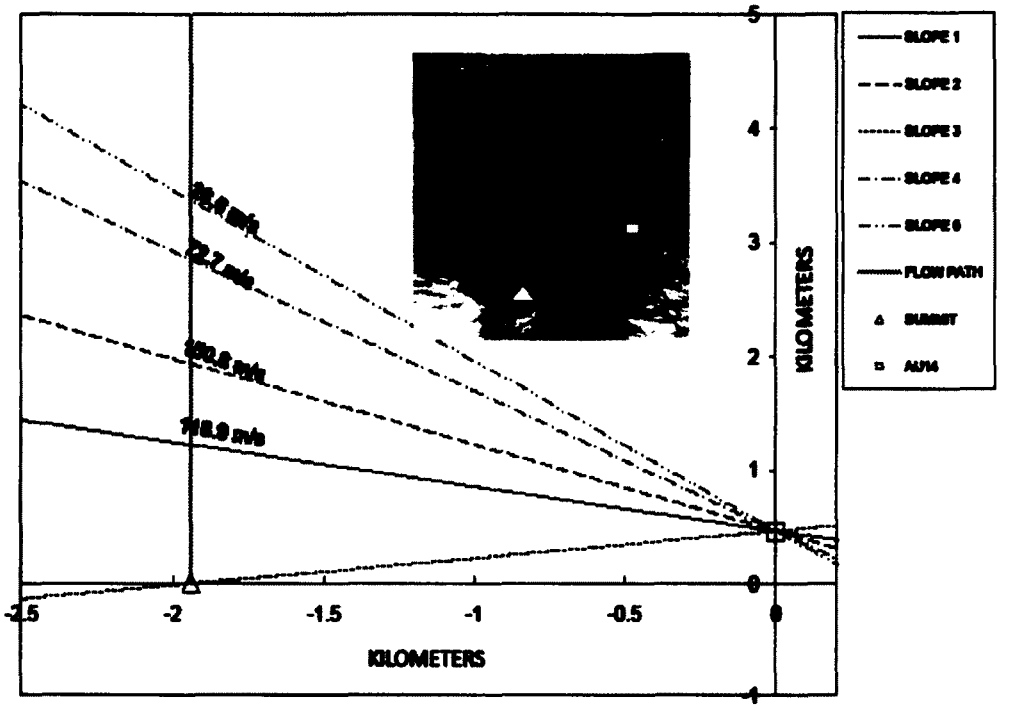

Figure 4.13

Azimuths of arrival determined from particle motions. The plot shows the azimuths of the particle motions at AU14 at different times extrapolated to show their intersection with the flow event (represented by the vertical line). The azimuths were calculated with linear least squares analysis and the steepest azimuth from times 1, 2, 4 and 6, and one from time 3 were used The azimuths from time 5 were similar to ones already used. The azimuths used were: 1) -.39, 2) -0.76, 3) 0.24, 4) -1.23, 6) -1.5. Velocities of the flow at those points were then calculated and show that the flow was decreasing in velocity as it descended. Note that the chart is not to scale. The inset shows the same azimuths overlying a map of Augustine generated with Google Earth, which shows visible block and ash flow deposits, for context.

4.8. References

Battaglia, J., Aki, K., 2003. Location of seismic events and eruptive fissures on the Piton de la Fournaise volcano using seismic amplitudes. Journal of Geophysical Research, 108, B8, 2364, doi:10.1029/2002JB002193.

Brodscholl, A., Kirbani, S.B., Voight, B., 2000. Sequential dome-collapse nuees ardentes analyzed from broadband seismic data, Merapi Volcano, Indonesia. Journal of Volcanology and Geothermal Research, 100, p. 363-369.

Buurman, H.,West, M., 2010. Seismic precursors to volcanic explosions during the 2006 eruption of Augustine Volcano. U.S. Geological Survey Professional Paper 1769.

Calder, E.S., Cole, P.D., Dade, W.B., Druitt, T.H., Hoblitt, R.P., Huppert, H.E., Ritche, L., Sparks, R.S.J., Young, S.R., 1999. Mobility of pyroclastic flows and surges at the Soufriere Hills Volcano, Montserrat. Geophysical Research Letters, 26, p. 537-540.

Cervelli, P.F., Fournier,T.F., Freymueller, J.T., Power, J.A, Lisowski, M., Pauk, B.A., 2010. Geodetic constraints on magma movement and withdrawal during the 2006 eruption of Augustine Volcano. U.S. Geological Survey Professional Paper 1769.

Cole, S.E., Cronin, S.J., Sherburn, S., Manville, V., 2009. Seismic signals of snow-slurry lahars in motion: 25 September 2007, Mt. Ruapehu, New Zealand. Geophysical Research Letters, 36, L09405.

Coombs, M.L., Bull, K.F., Vallance, J.W., Schneider, D.J., Thoms, E.E., Wessels, R.L., McGimsey, R.G., 2010. Timing, distribution, and character of proximal products of the 2006 eruption of Augustine Volcano, Alaska. U.S. Geological Survey Professional Paper 1769.

Dehn, J., Dean, K.G., Engle, K., Izbekov, P., 2002. Thermal precursors in satellite images of the 1999 eruption of Shishaldin Volcano: Bulletin of Volcanology, 64, p. 525-534.

Deparis, J., Jongmans, D., 2008. Analysis of rock-fall and rock-fall avalanche seismograms in the French Alps. Bulletin of the Seismological Society of America, 98, p. 1781-1796.

DeRoin, N., McNutt, S.R., 2011. Rockfalls at Augustine Volcano, Alaska: The influence of eruption precursors and seasonal factors on occurrence patterns: 1997-2009. Journal of Volcanology and Geothermal Research, 211-212, p. 61-75.

Dixon, J.P., Stihler, S.D., Power, J.A., Tytgat, G., Moran, S.C., Sanchez, J., Estes, S., McNutt, S.R., Paskievitch, J., 2003. Catalog of earthquake hypocenters at Alaskan volcanoes: January 1 through December 31, 2002. U.S. Geological Survey Open-File Report 03-267. 58 p.

Dixon, J.P., Stihler, S.D., Power, J.A., and Searcy, C.K., 2010. Catalog of earthquake hypocenters at Alaskan volcanoes: January 1 through December 31, 2009. U.S. Geological Survey Data Series 531, 84 p.

Harris, A. J. L., Butterworth, A.L., Carlton, R.W., Downey, I., Miller, P., Navarro,

P., Rothery, D.A., 1997. Low-cost volcano surveillance from space: case studies from Etna, Krafla, Cerro Negro, Fogo, Lascar and Erebus. Bulletin of Volcanology, 59, p. 49-64.

Johnson, C.E., Bittenbinder, A., Bogaert, D., Dietz, L., Kohler, W., 1995. EARTHWORM: A flexible approach to seismograph network processing. Incorporated Research Institutions for Seismology Newsletter, 14, no.2, p. 1-4.

Jolly, A.D., Thompson, G., Norton, G.E., 2002. Locating pyroclastic flows on Soufriere Hills volcano, Montserrat, West Indies, using amplitude signals from high dynamic range instruments. Journal of Volcanology and Geothermal Research, 118, p. 299-317.

Kumagai, H., Palacios, P., Maeda, T., Castillo, D.B., Nakano, M., 2009. Seismic tracking of lahars using tremor signals. Journal of Volcanology and Geothermal Research, 183, p.112-121.

Lahr, J.C., 1999. HYPOELLIPSE: A computer program for determining local earthquake hypocentral parameters, magnitude, and first motion pattern. U.S. Geological Survey Open-File Report 99-23, 116 p.

Lee, W. H. K., Bennet, R.E., Meagher, K.L., 1972. A method of estimating magnitude of local earthquakes from signal duration. U.S. Geological Survey Open File Report.

Norris, R.D., 1994. Seismicity of rockfalls and avalanches at three Cascades Range

volcanoes: Implication for seismic detection for hazardous mass movements. Bulletin of the Seismological Society of America, 84, p. 1925-1939.

Power, J.A., Lalla, D.J., 2010. Seismic observations of Augustine Volcano, Alaska; 1970 – 2007. U.S. Geological Survey Professional Paper 1769.

Power, J.A, Nye, C.J., Coombs, M.L., Wessels, R.L., Cervelli, P.F., Dehn, J., Wallace, K.L., Freymueller, J.T., Doukas, M.P., 2006. The reawakening of Alaska's Augustine Volcano. Eos, 87, no. 37, p. 373-377.

Richter, C.F., 1958. Elementary Seismology. Freeman and Company, Inc., San Francisco. 768 p.

Robinson, M., 1990. XPICK user's manual, version 2.7. Seismology Lab, Geophysical Institute, University of Alaska at Fairbanks, 93 p.

Scholz, C. H., 1990. The Mechanics of Earthquakes and Faulting: Cambridge University Press, New York, 439 p.

Sentman, D.D., McNutt, S.R., Stenbaek-Nielsen, H.C., Tytgat, G., DeRoin, N., 2010. Imaging observations of thermal emissions from Augustine volcano using a small astronomical camera. U.S. Geological Survey Professional Paper 1769.

Uhira, K., Tamasoto, H., Takeo, M., 1994. Source mechanism of seismic waves excited by pyroclastic flows observed at Unzen volcano. Japan. Journal of Geophysical Research, 99, p. 17757-17773.

Ui, T., Matsuwo, N., Sumita, M., Fujinawa A., 1999. Generation of block and ash flows during the 1990-1995 eruption of Unzen Volcano, Japan. Journal of Volcanology and Geothermal Research, 89, p. 123-137.

Vallance, J.W., Bull, K.F., Coombs, M.L., 2010. Pyroclastic flows, lahars and mixed avalanches generated during the 2006 eruption of Augustine Volcano. U.S. Geological Survey Professional Paper 1769.

Vilajosana, I., Surinach, E., Abellan, A., Khazaradze, G., Garcia, D., Llosa, J., 2008. Rockfall induced seismic signals: case study in Montserrat, Catalonia. Natural Hazards and Earth System Sciences, 8, p. 805-812.

Weichart D., Horner, R. B., Evans, S.G., 1994. Seismic signatures of landslides- the 1990 Brenda Mine collapse and the 1965 Hope rockslides. Bulletin of the Seismological Society of America, 112, p. 75-85.

Chapter 5

Relation of Seismic Signal, Noise and Station Distance to Reduced Displacement Measurements[4]

Abstract

Observations of strongly varying reduced displacements (D_R) in 3-day D_R monitoring plots prompted this study. D_R measurements from seismically monitored volcanoes in the AVO network were compared with magnitude residuals and station distance to vent in an attempt to determine the source of strongly varying D_R data at some seismic recording stations. No correlation between magnitude residuals and reduced displacements was observed, but D_R values did tend to increase with station distance from the vent. This is a result of an artifact of the D_R calculations, which take distance from vent into account. When noise signals occur at the recording site, the D_R calculations assume the signals come from the vent and amplify them accordingly, resulting in the widely spaced D_R measurements that are sometimes seen in monitoring plots. When a signal originating at the volcanoes is recorded, the wide spacings between different stations D_R values usually disappear, resulting in accurate recording of the signal strength.

[4] DeRoin, N. and McNutt, S.R. 2012. Relation of Seismic Signal Noise, and Station Distance to Reduced Displacement Measurements. Prepared for submission.

5.1. Introduction

In volcano monitoring, reduced displacements (D_R) are a useful tool for routine volcano monitoring. D_R is a measure of the amplitude of volcanic tremor, corrected for geometrical spreading. It is an absolute measure, suitable for comparison with data from other volcanoes, similar to magnitude calculations for earthquakes. In the seismology laboratory at the UAF Geophysical Institute, reduced displacements are commonly used in routine monitoring of the seismically instrumented active volcanoes. For example, D_R plots consisting of the last three days worth of D_R measurements can be viewed for each seismically monitored volcano (see fig. 5.1). In such plots, each point represents the maximum D_R in a ten minute window. Observations of strongly varying reduced displacements (D_R) in 3-day D_R monitoring plots prompted this study. In plots such as figure 5.1B, widely varying D_R values are seen from different stations. Differences of up to two orders of magnitude of D_R data are seen, such as between stations DRR3 and DTN. The instances of widely varying D_R data may be a result of site effects. Site effects are geologic or weather features that act near the seismic recording stations and cause significant differences. Factors such as scattering, attenuation, reflections, geometric spreading, materials, and topographic variations in the seismic wave's path will affect the recorded seismogram (Lay and Wallace, 1995). Geologic features or irregularities near the recording station such as frozen versus thawed ground, and loose soil versus solid rock may also be sources of site effects.

Magnitude residuals are another measurement made from routine seismic monitoring of volcanoes that may be related to site effects. Earthquakes are located on a daily basis as a part of routine monitoring of volcanoes at the Alaska Volcano Observatory (AVO). When an earthquake is located, magnitudes for the events are calculated at various stations. Due to different radiation patterns or site effects near the stations slight differences in magnitude may result. The magnitudes from each station are averaged to give the assigned magnitude of the earthquake. The difference between the magnitude given by a particular station and the average magnitude is that station's magnitude residual. One motivation for this study was to test whether both magnitude residuals and varying reduced displacements were related to site effects affecting that particular station that recorded the data. If both phenomena are related to site effects at a particular station, then stations with highly anomalous D_R measurements should show high magnitude residuals as well.

5.2. Methods

5.2.1. Reduced displacement

Reduced displacement is a common measurement made for volcanic tremor that takes into account distance from the station, instrument magnification and corrects for geometrical spreading, making it possible to compare tremor at different volcanoes. Reduced displacement can be calculated with body waves or surface waves and is usually expressed as units of cm^2 (McNutt, 1992). Original formulations for reduced displacements were done by Aki and Koyanagi (1981) for

body waves and Fehler (1983) for surface waves. For body waves, the equation to calculate reduced displacement (D_R) is:

$$(1) \quad D_R = Ar$$

where A is the RMS amplitude of the displacement seismogram (peak divided by $2\sqrt{2}$) and r is the source-to-station distance (Aki and Koyanagi, 1981). For surface waves, the equation is:

$$(2) \quad D_R = = A\sqrt{r\lambda}$$

where A is the RMS amplitude of the ground displacement and λ = wavelength (Fehler, 1983). In routine AVO monitoring, reduced displacement is determined in a slightly different way. As described in van Manen et al. (2010), seismic amplitudes are measured is a narrow band around the dominant frequency of the recorded signal, and a geometrical spreading term is included so that data from more distant stations can be used. Because of these differences, reduced displacement measurements determined by AVO may vary slightly from those determined from the standard methodologies. Reduced displacement data for this project were taken from near-real time reduced displacement plots generated from three days of data for monitoring, ranging from January to February 2005. Each D_R value represents a measurement of reduced displacement at a single time (the same time for each station at a particular volcano). Then $\log_{10}$ of the measurements were

taken. Figure 5.1 shows two of the three day reduced displacement plots from which D_R data was obtained. The triangle at the bottom of each figure denotes the times at which the D_R values for each station was found.

5.2.2. Magnitudes and magnitude residuals

For earthquakes occurring at or near volcanoes monitored by the Alaska Volcano Observatory (AVO) phase arrival times are picked with the seismic data analysis program XPICK (Robinson, 1990) and magnitudes are calculated with the location program HYPOELLIPSE using the maximum trace amplitude and/or signal duration (Lahr, 1999). From Lahr (1999) the local Richter magnitude (XMAG) is calculated by HYPOELLIPSE with the following equation:

$$(3) \quad XMAG = \log_{10}\frac{A}{2} + [-B_1 + B_2 log X^2] + G$$

where A is the maximum amplitude (peak-to-peak, in millimeters), X is the square root of the sum of the squares of the epicentral distance and the focal depth (in kilometers), and G is the station correction factor. B_1 and B_2 are determined from the slopes of a plot comparing the term $\log(A_0)$ from Richter (1958) with HYPOELLIPSE. The plot of $-\text{LOG}(A_0)$ versus distance has two slopes, and therefore two sets of B_1 and B_2 values are used; one for distances between $1\text{km} \leq D < 200\text{km}$ and one for $200\text{km} \leq D \leq 600\text{km}$ (Lahr, 1999). Due to different radiation patterns or site effects near the station slight differences in magnitude may

results. The magnitudes from each station are averaged to give the assigned magnitude of the earthquake. The difference between the magnitude given by a particular station and the average magnitude is that station's magnitude residual. By convention, a positive residual is a magnitude higher than the average, and a negative residual is lower than the average. The magnitude residuals used here come from the average of magnitude residuals calculated from August 1, 2004 to January 21, 2005. These residuals were determined from varying numbers of earthquake picks (locations) in this time period, ranging from ~10 to > 1000 picks at a particular station.

5.3. Results and discussion

Both magnitude residuals and reduced displacement measurements are affected by site effects. To test whether the same site effects that lead to magnitude residuals also lead to differences in reduced displacements, both were compared for stations at multiple volcanoes in the AVO network. For each volcano, the magnitude residuals and reduced displacements for each station were plotted against one another (fig. 5.2). Note that while the magnitude residuals are average values, the reduced displacement values were single data points, representing a snapshot of reduced displacement behavior in time. Plots were made for each seismically monitored volcano in the AVO network and similar results were found for all. No correlations were found between magnitude residuals and reduced displacements for any network, suggesting that site effects are not the cause. Next, magnitude

residuals (same data as used previously) for each station in a network were plotted against the station's distance to the source vent. The same was done for reduced displacement (again using the same "snapshot" DR values) and distance to the vent. Magnitude residuals did not vary with distance from the source. Reduced displacements, however, did show systematic correlation with the stations' distance to the source. Apparent increases in D_R occurred with increasing distance from the vent (fig. 5.3).

This effect is likely occurring because the calculation of reduced displacement takes distance of the station from the volcano into account explicitly. In other words, the source is assumed to be at the vent. Because tremor attenuates over distance, it will be weaker at farther stations than closer ones. The D_R calculation will therefore amplify the signal according to their distance from the vent. When the signal being recorded is not actually tremor at the vent, but rather a local effect such as wind occurring near the station, the D_R calculation will still magnify the signal as if it were coming from the vent. Figure 5.4 shows a D_R plot from Westdahl volcano. D_R values at the six stations at Westdahl volcano show very different types of behavior. Stations WECS (red) and WESP (aqua) tracked one another most of the time. Station WTUG (yellow) was not functioning at the time. Station WESE (green) was far off from the other stations most of the time, but began to track stations WECS and WESP around 09:00 UT June 15th. Spectrograms show that up until this point (~09:00 UT), station WESE had been recording mainly noise (fig. 5.4B) but then began recording a real signal (fig. 5.4c). When WESE began

recording the signal, the D_R values began to match those of the WECS and WESP, which recorded the same signal.

5.4. Conclusions

When interpreting reduced displacements and other seismic measurements from volcanoes, it is important to keep in mind the effects that other factors besides the volcanic signal, such as site effects, can have. This study, while simple, reveals that an artifact of computing reduced displacement, that of taking station distance from source vent into account, can skew D_R measurements in the absence of a sufficiently strong signal from the source. This fact must be taken into account during everyday volcano monitoring as well as with studies involving reduced displacement.

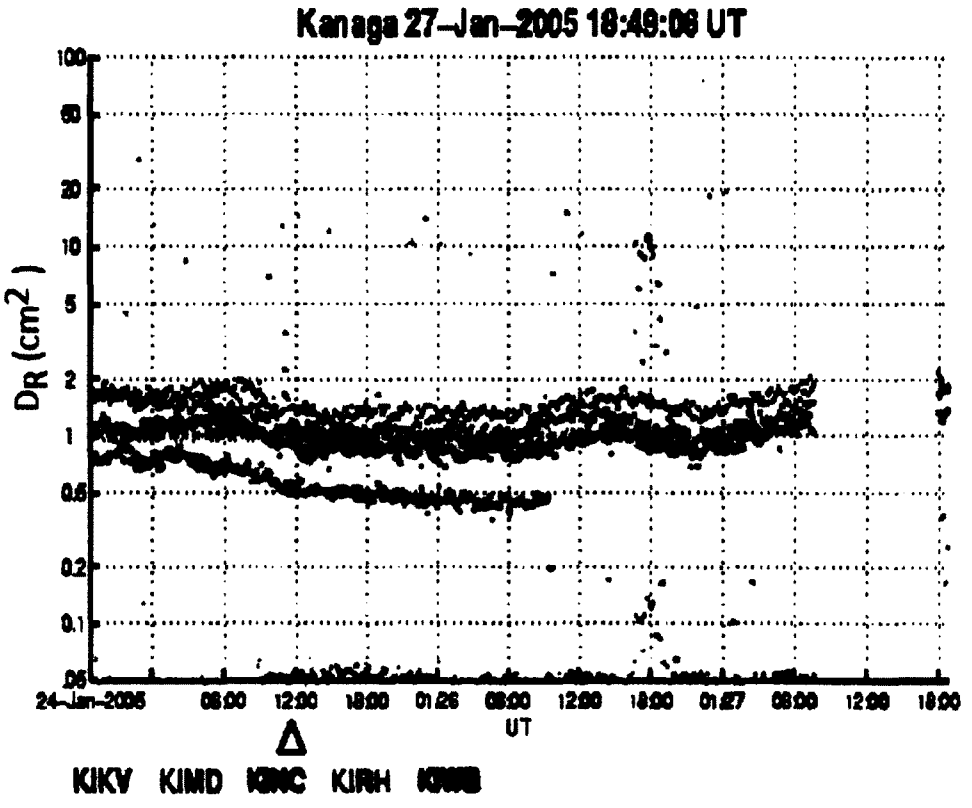

A

Figure 5.1

Two plots of reduced displacement monitoring plots. The plots are three days duration each. Values are determined every ten minutes and the strongest D_R in the ten-minute window is used. A) shows measurements for which data from different stations are very close together, although at several points the values diverge slightly. B) shows measurements that are very far apart, with differences of up to two orders of magnitude, such as between stations DRR3 and DTN. The black triangle in the pictures show the times at which reduced displacement measurements were made for the plots in figures 5.2 and 5.3.

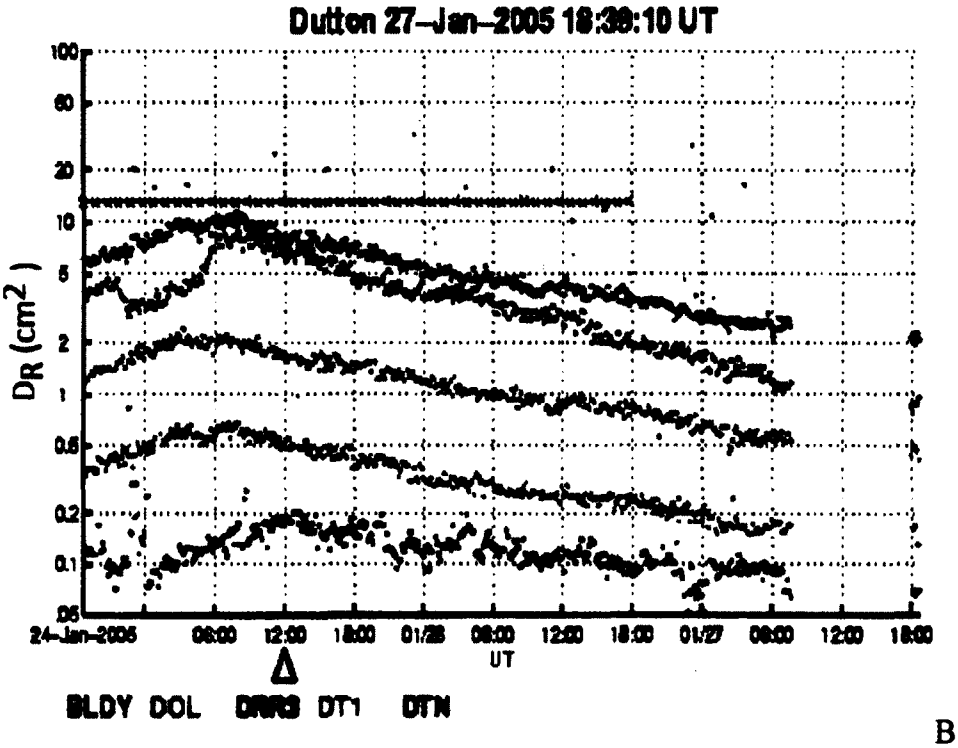

B

Figure 5.1 continued

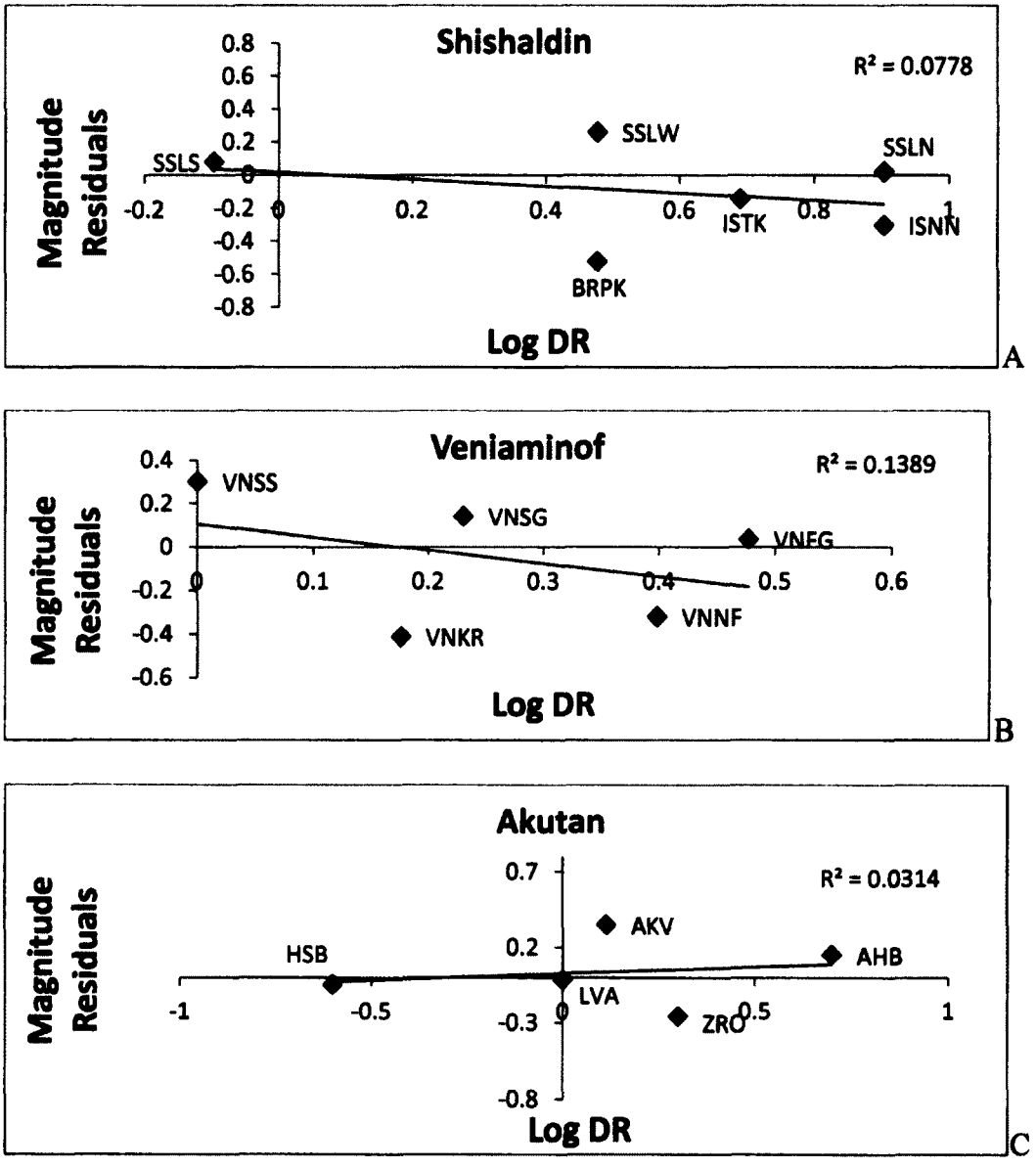

Figure 5.2

Plots of the magnitude residuals vs. $\log_{10}$ of reduced displacement. The plots do not show correlation of increasing magnitude residuals with reduced displacement and the low r^2 values of the linear fits confirm this.

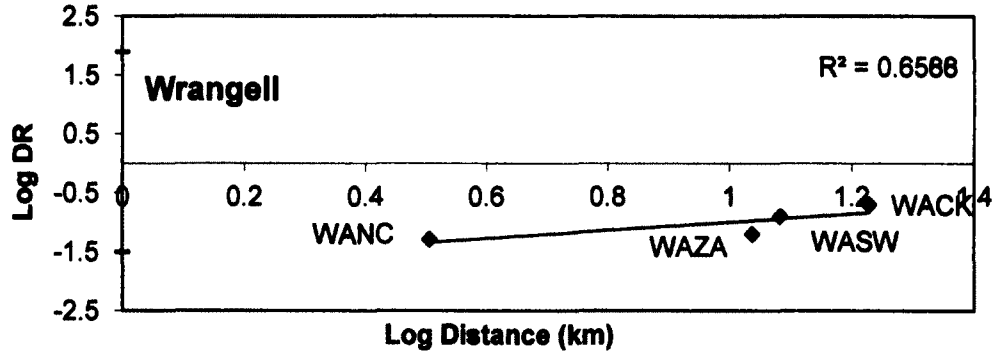

A

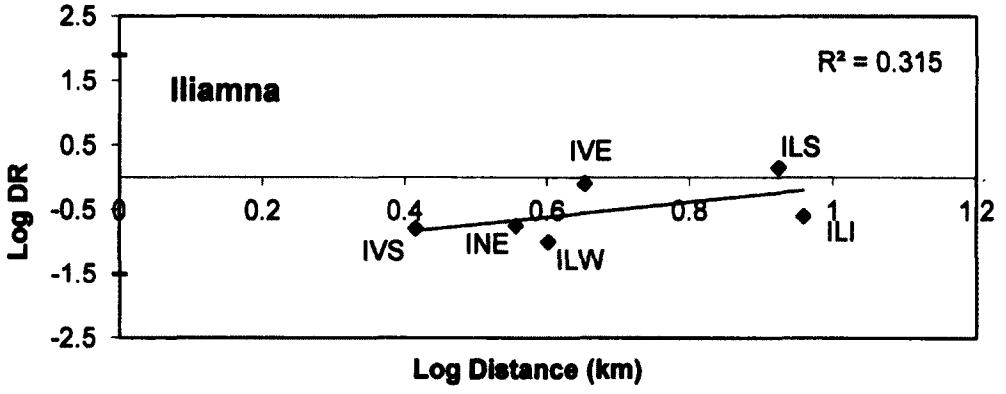

B

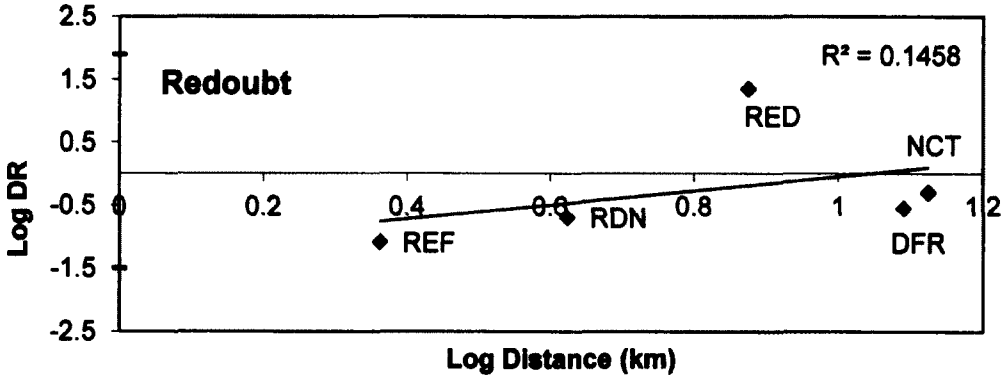

C

Figure 5.3

Log_{10} reduced displacement vs. log_{10} of distance. The plots all show correlation of increasing reduced displacement with increasing distance (positive slopes). The strengths of the correlations varied, as shown by the r^2 values of the linear fits.

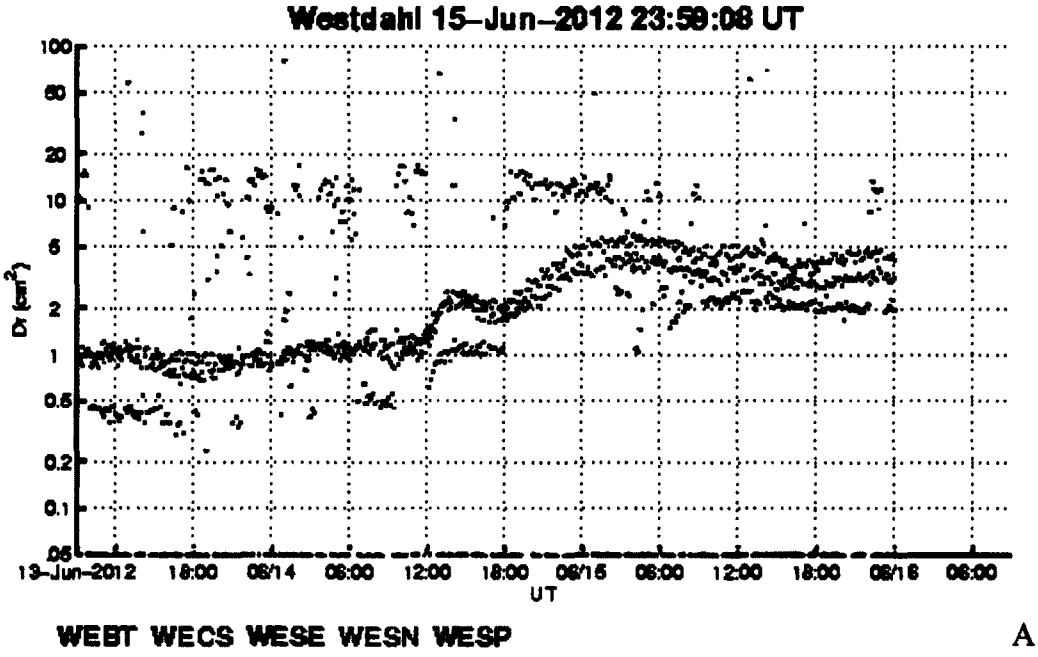

Figure 5.4

Reduced displacement plot and corresponding spectrograms. These plots are of Westdahl volcano. A) D_R measurements of six stations at Westdahl volcano. Stations WECS (red) and WESP (aqua) track one another most of the time. Station WESE (green) is far off from the other stations most of the time, but begins to track stations WECS and WESP around 12:00 UT June 15th. Spectrograms from this time show that up until this point, station WESE had been recording noise but then began recording a signal. B) shows the spectrograms for WECS, WESE, and WESP at a point before 6/15/2005 12:00 UT, when WESE was only recording noise, and C) shows the same three stations after WESE begins tracking WECS and WESP.

Westdahl 2012/06/15 05:00 - 05:10

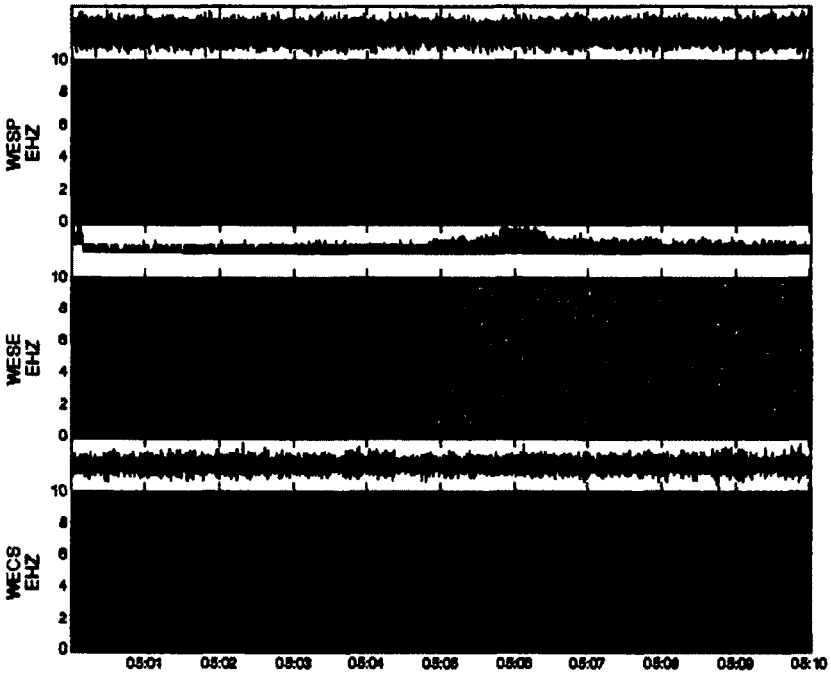

B

Westdahl 2012/06/15 10:50 - 11:00

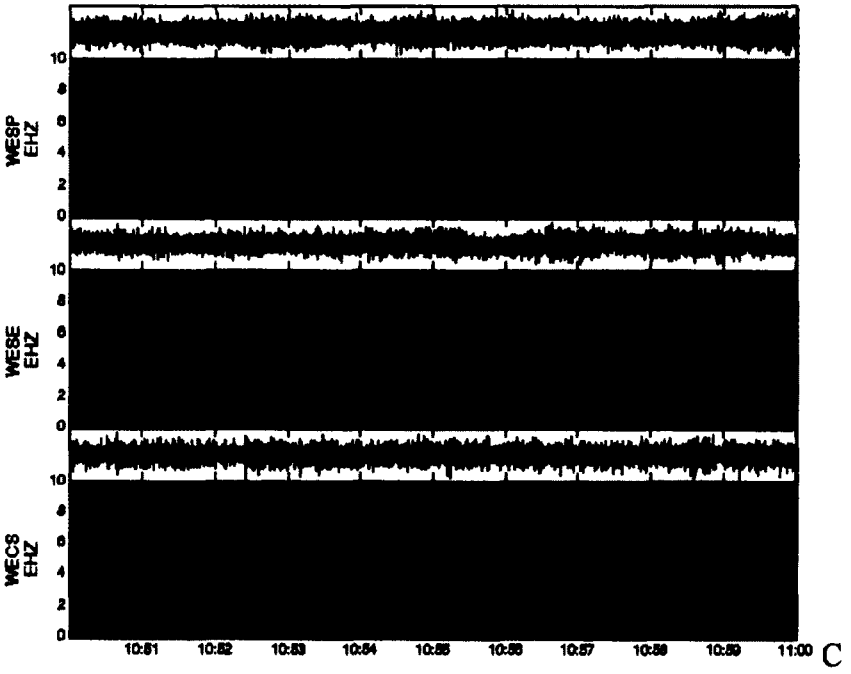

C

Figure 5.4 continued

5.5. References

Aki, K., Koyanagi, R. Y., 1981. Deep volcanic tremor and magma ascent mechanism under Kilauea, Hawaii. Journal of Geophysical Research, 86, p. 7095-7110.

Fehler, M., 1983. Observations of volcanic tremor at Mount St. Helens volcano. Journal of Geophysical Research, 88, p. 3476-3484.

Lahr, J.C., 1999. HYPOELLIPSE: A computer program for determining local earthquake hypocentral parameters, magnitude, and first motion pattern. U.S. Geological Survey Open-File Report 99-23, 116 p.

Lay, T., Wallace, T.C., 1995. Modern Global Seismology. Academic Press, 521 p.

McNutt, S.R., 1992. Volcanic Tremor: Encyclopedia of Earth System Science, 4, p. 417-425.

Richter, C.F., 1958. Elementary Seismology. Freeman and Company, Inc., San Francisco. 768 p.

Robinson, M., 1990. XPICK user's manual, version 2.7. Seismology Lab, Geophysical Institute, University of Alaska at Fairbanks, 93 p.

van Manen, S.M., Dehn, J., West, M.E., Blake, S., Rothery, D.A., 2010. The 2006 eruption of Augustine Volcano – Combined analyses of thermal satellite data and reduced displacement. U.S. Geological Survey Professional Paper 1769.

Chapter 6

Duration-Amplitude Relationships of Volcanic Tremor and Earthquake Swarms Preceding and During the 2009 Eruption of Redoubt Volcano, Alaska[5]

Abstract

Duration-amplitude relationships were studied for tremor episodes and earthquake swarms occurring during the 2009 eruption of Redoubt Volcano, Alaska. Duration-amplitude distribution plots were generated daily January 1 through May 31 and fit with both an exponential law and power law. Comparing r^2 values of the fit for both laws showed that the exponential law gave better fits for the duration-amplitude relationships for days in which volcanic tremor and earthquake swarms occurred, while the power law gave better fits for other days. Fitting segments of seismic data with both an exponential and a power law leads to a metric that has potential for volcano monitoring: r^2_{exp} / r^2_{pow}, the ratio of the r^2 fits using the exponential law over the power law. The ratio r^2_{exp} / r^2_{pow} tended to be greater than 1 when volcanic activity or precursory seismic activity was occuring, and less than 1 when no volcanic seismic activity was occuring. Duration-amplitude plots were generated for episodes of volcanic tremor that were identified by the $r^2_{exp} / r^2_{pow} \geq 1$ method and compared to one another in an attempt to identify changes that may have occurred during the eruption. Stronger episodes of volcanic tremor showed higher

[5] DeRoin, N., McNutt, S.R., and Thompson, G. 2012. Duration-Amplitude Relationships of Volcanic Tremor and Earthquake Swarms Preceding and During the 2009 Eruption of Redoubt Volcano, Alaska. Prepared for submission.

characteristic amplitudes. Maximum heights of the plumes generated by the explosions showed a positive correlation with the characteristic amplitude of the concurrent tremor.

6.1. Introduction

6.1.1. Duration amplitude relationships

In studies of earthquakes, frequency-size (or frequency-magnitude) relationships are often studied. For example, variations in b-values, derived from the power-law relationship relating the number of earthquakes vs. magnitude, have been attributed to material heterogeneity (Mogi, 1962), shear stress (Scholtz, 1968), pore pressure and effective stress (Wyss, 1973) and thermal gradients (Warren and Latham, 1970). For volcanic tremor, the corresponding frequency-size relationship is duration-amplitude (DA). In a duration-amplitude distribution the equivalent of the b-value is the characteristic amplitude. In a previous study on the duration-amplitude relationship of volcanic tremor, Benoit et al. (2003) showed that the characteristic amplitude for volcanic tremor during eruptions at 8 volcanoes was higher than that of non-eruptive tremor.

The frequency-size distribution for earthquakes obeys a power law (e.g., Gutenberg and Richter, 1956), while there is good evidence that duration-amplitude distributions for volcanic tremor obey an exponential law (Benoit et al., 2003). Exponential distributions describe processes that are scale-bound, whereas power law distributions describe processes that are scale invariant. The difference between

these fundamental processes may be useful in understanding the relationship between low-frequency earthquake swarms and volcanic tremor, both of which commonly occur before and during volcanic eruptions. In some cases, volcanic tremor is observed to be composed of numerous low-frequency earthquakes (e.g. Fehler, 1983). In Benoit et al. (2003) volcanic tremor is thought to be driven by variable pressures acting on a fixed source geometry, and characteristic amplitudes are therefore proportional to a geometric source dimension, such as crack or conduit lengths. In Benoit et al. (2003) the case is made that because earthquakes show power-law scaling, and because volcanic tremor amplitudes exhibit exponential scaling, the two processes are fundamentally different.

Benoit et al. (2003) compared the characteristic amplitudes of eruptive and non-eruptive tremor at several volcanoes. In that case, each eruption was considered as a whole (i.e. one determination for the eruption sequence). Redoubt Volcano, which was one of the volcanoes studied in Benoit et al. (2003) erupted again in 2009. The well monitored eruption lasted several months and produced ash columns up to 18,000m. Because tremor occurred before and throughout most of the 2009 eruption of Redoubt, this eruption is a good subject for a further study of duration-amplitude relationships of tremor and characteristic amplitudes, and also the relationship between low-frequency earthquake swarms and volcanic tremor. In this study, characteristic amplitudes of eruption tremor, as well as precursory tremor and earthquake swarms will be calculated throughout the 2009 Redoubt eruption.

6.1.2. Redoubt seismic monitoring

Redoubt Volcano (60.48°N, 152.74°W) is a 3108 m stratovolcano located in southern Alaska, approximately 180 km southwest of the city of Anchorage, Alaska. Figure 6.1 shows a map of Mt. Redoubt and the seismic stations monitoring it. Stations DFR, NCT, RDN, RDT, RDE, RSO are single component short period vertical stations, REF and RED are three component short period stations, and analog telemetry is used to send these data to the Alaska Volcano Observatory (AVO). A significant drawback of the analog telemetry utilized for the short-period stations is that it offers poor dynamic range, with the result that stations close to the volcano clipped at various times during the eruption. RDJH and RDWB are broadband stations that utilize modern high-dynamic-range digital telemetry (these stations did not clip), however these were not operational throughout the whole unrest sequence. Redoubt has erupted several times in the last century, most recently 1966, 1989, and 2009. The 2009 eruption produced ash columns of up to 18,000m and was very well monitored by seismic, geodetic, radar, geologic and visual observations (Schaefer, 2012).

6.1.3. Eruption chronology

Redoubt began showing signs of activity in 2008, when weak precursory tremor was observed beginning in September 2008 (Buurman et al., 2012; Schaefer. 2012). Gas emissions were also observed to have increased (Werner et al., 2009;

Schaefer, 2012). In January 2009, activity appeared to increase as volcanic tremor began occurring (fig. 6.2). Two tremor episodes occurred in January, one starting Jan. 25 and lasting roughly two days; the other occurring on Jan. 30th. The seismic activity corresponded with high SO_2 levels (Werner et al., 2009; Schaefer, 2012). In early February, lower amplitude tremor began occurring and continued throughout February. The first explosion of the eruption sequence was a phreatic explosion which occurred on March 15. The first magmatic explosion occurred March 22, following a strong earthquake swarm that began approximately two days earlier. The first six explosions occurred within 9 hours of one another beginning March 23. Two more occurred March 26, and then 10 more occurred from March 27-29. The final explosion occurred April 4. The explosions were accompanied by numerous pyroclastic flows. After the final explosion, the volcano began a phase of dome building, which ended by July 1, 2009 (Buurman et al., 2012). Figure 6.2 shows a time series of the seismicity of the eruption from January 2009 to mid May 2009, and concurrent volcanic activity, with episodes of tremor labeled as identified in Buurman et al. (2012) and Schaefer (2012).

6.2. Methods

6.2.1. Data

The "Tremor Monitoring in Real-time" (TreMoR) system at AVO loads continuous segments of waveform data from Antelope (usually either 10-minutes or 1-hour at a time), and produces spectrograms, which have long been a vital

monitoring tool for AVO scientists. TreMoR also produces various timeseries sampled once per minute, modeled on real-time seismic-amplitude measurement (RSAM) data (Endo and Murray, 1991) and stored in the same format. These time series include the peak, median and root-mean-square (RMS) of each 1-minute time window, for instrument corrected velocity and displacement seismograms. A calibration correction is applied to convert from counts to a velocity seismogram. A non-overlapping 1-minute window is passed along the continuous raw seismogram. The 1-minute seismogram is then detrended, and the appropriate instrument correction is applied from the Antelope database to convert the raw seismogram (measured in counts) to velocity (measured in nm/s), resulting in a 1-minute velocity seismogram. This is high-pass filtered (at 0.5 Hz) and integrated to a displacement seismogram. The maximum, median, mean and RMS amplitude of each 1-window velocity and displacement seismogram are archived to an RSAM-format binary file. The summed square of the velocity seismogram is also archived, as a proxy for seismic energy.

In this study, the dataset we examined were the RMS displacement RSAM-format files produced by the TreMoR system. The TreMoR system also includes a MATLAB toolbox which provides graphical tools to enable a user to produce duration-amplitude plots, and fit exponential and power law distributions to these data, as discussed below.

6.2.2. Duration-amplitude plots

Duration-amplitude plots (fig. 6.3) compare the total (cumulative) duration of a signal at or above a particular amplitude (reduced displacement). Amplitudes are measured from the envelope of the seismograms. Benoit et al. (2003) found that the duration-amplitude distribution of volcanic tremor episodes at 8 volcanoes were best fit by an exponential law, rather than a power law. The exponential law used to fit the data is given by:

$$(2) \qquad d = d_t e^{-A\lambda}$$

This can be linearized as:

$$(3) \qquad log_{10}\left(\frac{d}{d_t}\right) = -\frac{\lambda A}{log_e(10)}$$

This is a probability density function where d is the duration of tremor greater than or equal to the displacement amplitude A, and d_t is the total duration of tremor. When the $\log_{10}$ of the fractional duration d/dt is plotted against displacements, d, the rate parameter is λ, which is proportional to the negative of the slope. The power law is given by:

$$(4) \qquad d = d_t A^{\gamma}$$

where γ is the slope of the line. This can be linearised as:

$$(5) \qquad log_{10}\left(\frac{d}{d_t}\right) = \gamma log_{10}(A)$$

Duration-amplitude plots were generated using TreMoR and fit with both laws. Clipping of the signal at high amplitudes, as well as poor signal to noise ratio at low amplitudes, mean that we would not expect the plots to be linear throughout the entire amplitude range shown, so it was necessary to identify the linear section of each plot by eye. MATLAB's polyfit function is then used to fit the line, yielding λ or γ (see equations above). These are inversely proportional to the characteristic amplitude. Figure 6.3 shows the relationship of a seismogram envelope to a generated duration-amplitude plot.

6.3. Exponential vs. power law distributions

6.3.1. Volcanic seismic activity and r^2_{exp} / r^2_{pow}

Daily duration-amplitude plots were generated for the various tremor episodes of the 2009 Redoubt eruption sequence. Duration-amplitude plots were generated for one day's worth of data at a time, from January 1 to May 31, using seismic data from stations REF and RSO. The data were then modeled with an exponential law and a power law (fig. 6.4). The exponential law is fit to log (d_t) vs

displacement while the power law is fir to log (d_t) vs log (displacement). A linear fit was applied to each plot, and a rate parameter and r^2 value were calculated. Plotting the daily value of r^2_{exp} / r^2_{pow} shows that the majority of the time, the power law distribution gave a better fit ($r^2_{exp} / r^2_{pow} \leq 1$). However, days in which the exponential law had higher r^2 values than the power law ($r^2_{exp} / r^2_{pow} \geq 1$) generally coincided with days in which tremor or other volcanic related seismicity had occurred. Figure 6.5 shows plots of r^2_{exp} / r^2_{pow} from January 1 until the end of the magmatic explosions, with the periods of seismic and volcanic activity numbered as shown in figure 6.2. These results show that the r^2_{exp} / r^2_{pow} method successfully identifies many tremor episode. The comparison of r^2_{exp} / r^2_{pow} with the volcanic activity throughout the rest of the eruption is discussed further in the next section.

6.4. Duration amplitude plots

The results presented in the above section show that an exponential distribution of duration-amplitudes fits periods of volcanic activity during the Redoubt 2009 eruption, while the power law better fit seismic periods of little or no activity or those dominated by stray high amplitude spikes. It should be noted that both signals and noise are measured at the seismic stations and therefore the duration-amplitudes include both as well. [For good discussion of seismic noise and spectra see Peterson (1993) and Peck (2008).] From this point on, the paper uses exponential fits of the data. Note that when slopes (the negative of the rate

parameter λ) are discussed, the absolute value is implied, i.e., a lower slope is a flatter slope, as all the slopes are negative.

6.4.1. Episodes detected by r^2_{exp} / r^2_{pow}

Figure 6.6(A-I) shows the episodes of tremor that were identified in the previous section, plotted to the scale of the longest episode. Duration-amplitude plots of the same episodes are shown in figure 6.7(A-I). Many of the plots show a similar form with two bends and the flattest slope in the middle. The first segment usually has the steepest slope, and is probably related to noise. Noise is defined here as low-amplitude signals (<50 nm) that are present under the actual seismic signals. DA plots from different stations all show characteristic amplitudes for the low amplitude noise segments that are dramatically different, and therefore apparently non-systematic. The middle segment usually has the flattest slope, and therefore the strongest characteristic amplitude. The third segment, when present, usually reflects high amplitude noise spikes, resulting in a flattening out of the slope (see fig. 6.7A), or clipping (saturating), resulting in a curve, concave downward (see fig. 6.7B). Table 1 summarizes the tremor and swarm episodes shown in the figures 6.6 and 6.7. In general, the flattest slopes tended to occur with stronger activity and therefore higher seismic displacements (fig. 6.8).

6.4.2. Limitations to the r^2_{exp} / r^2_{pow} method

The $r^2_{exp} / r^2_{pow} \geq 1$ tends to work best for identifying the start and/or the high amplitude peaks of a tremor episode, and does have some limitations that appear to be caused by either the choice of time over which the modeling is done, or the presence of large amplitude spikes within a lower amplitude tremor episode. The first date identified by $r^2_{exp} / r^2_{pow} \geq 1$ was January 25. This corresponds with the beginning of the first tremor episode of January 25-27. January 26-27, however, fit a power law better, and this is likely due to high amplitude peaks dominating the tremor signal. RSO does show $r^2_{exp} / r^2_{pow} \geq 1$ for the 26th, but was affected by saturation/ data clipping during this episode, making the data unreliable.

The second date in which $r^2_{exp} / r^2_{pow} \geq 1$, is January 30, the start of the second precursory tremor episode. The next dates with $r^2_{exp} / r^2_{pow} \geq 1$ are February 7 and 8, which are near the start of the sustained tremor of February 2009, which began February 5. The sustained tremor continued throughout February, but an initial high amplitude phase lasted from February 5-10 (fig. 6.2). Only February 7th and 8th, however show $r^2_{exp} / r^2_{pow} \geq 1$. Here the choice of time over which to model the data is the likely cause of the poorer exponential fit. The fitting is done over 24 hours of data, but in actuality, the tremor only occurred in the final hours of February 5, and then only in the first and last few hours of February 6. By February 7, however, the tremor is continuously occurring, thus triggering $r^2_{exp} / r^2_{pow} \geq 1$.

The first explosion of the eruption was a phreatic explosion that occurred on March 15, that also was not detected by the r^2_{exp} / r^2_{pow} method. Most likely the

presence of higher amplitude spikes, with much greater amplitude than the underlying tremor, results in the poor fit with the exponential law. This is an effect of choosing an arbitrary time over which to calculate r^2_{exp} / r^2_{pow} when used for detecting episodes. High amplitude spikes not related to the tremor signal can be left out when studying the characteristic amplitude of the seismic episode, but for monitoring purposes, volcanic signal length vs. non-volcanic signal length will likely be a factor in determination of $r^2_{exp} > r^2_{pow}$.

6.4.3. DA plots at other stations

Because the characteristic amplitude is thought be related to a fundamental length or scale of the phenomenon it describes, different stations recording the same tremor episode should show similar characteristic amplitudes. Although station REF is primarily used in the analyses here, other stations were examined for comparison as well. Figure 6.9 shows duration-amplitude plots for the April 4 explosion for four stations. Each one displays $\lambda < 0.01$. This result was seen during the other magmatic eruptions as well. Figure 6.10 shows examples of duration-amplitude plots at several stations during the February 26-28 earthquake swarm. After an initial (low amplitude) steep slope, all three stations display a flat section with $\lambda =$ 0.02 up to 75nm (RDN), 150 nm (REF) and 200nm (RSO). The end (high amplitude) sections differ slightly from one another. Data from RSO show possible effects of clipping, by curving downward with $\lambda = 0.04$, while data from RDN and REF flatten out, displaying $\lambda = 0.01$ over the higher displacements. Thus, although

site effects and distance to the station may cause variations in the duration-amplitude plots, i.e., clipping/saturation at nearby stations and stronger regional signals overshadowing local activity at distant stations, the characteristic amplitudes are nearly the same from station to station. This supports the idea that the different stations record the same fundamental feature that is related to the source process.

6.5. Plume heights and characteristic amplitudes

The 2009 eruption of Redoubt produced 1 phreatic explosion and 19 magmatic explosions. These explosions produced ash clouds ranging from 4 to 19 km in height. Since tremor amplitude has been previously correlated with ash plume height (McNutt, 1994), it seemed likely that the slopes of the DA plots and the corresponding characteristic amplitudes would also correlate with maximum plume heights. Duration-amplitude plots were generated for each of the explosions and the slopes were calculated (using the entire plot, not just the flattest slope). The slopes of the DA plots and their inverses were both plotted against the heights of the plumes (fig. 6.11). Maximum plume heights were reported by Webley et al. (2012) and Schaefer (2012), and were determined by either USGS radar or FAA NEXRAD radar (Webley et al., 2012). Although scatter exists, the plume heights and slopes/characteristic amplitudes show good correlation in most cases. Specifically, fig. 6.11B shows a tight grouping for plumes above 7 km with three outliers

6.6. Discussion

6.6.1. Potential for r^2_{exp} / r^2_{pow} as monitoring tool

Because volcanic tremor is best described by an exponential law, the characteristic amplitude of the tremor refers to a fixed characteristic length or scale that is acted upon by varying forces to produce tremor amplitudes (Benoit et al., 2003). The characteristic amplitude is proportional to the inverse of the rate parameter (negative of slope) of the exponential distribution of volcanic tremor durations and amplitudes. Analysis of the duration-amplitude relationships for the main seismic episodes of the 2009 Redoubt eruption showed that stronger tremor episodes and earthquake swarms had stronger characteristic amplitudes. The slopes of the duration amplitude plots are also related to strength of volcanic activity. Figure 6.12 shows daily plots of slopes (fitting the whole plot) throughout the eruption for stations REF and RSO. Strong signals (low λ) predominated during the eruption; there are very few cases where $\lambda > 0.1$ from the period of mid-January until the end of April. The lowest λ values of the duration-amplitude plots (and therefore highest characteristic amplitudes) occurred during the magmatic explosions, which also had the highest reduced displacements. Earthquake swarms and tremor both give strong characteristic amplitudes that show $r^2_{exp} / r^2_{pow} \geq 1$. Maximum amplitudes do not seem to matter in determining whether $r^2_{exp} / r^2_{pow} \geq 1$; an overall continuous distribution of tremor amplitudes was more important. Characteristic amplitudes also showed a positive correlation with maximum plume heights. Higher characteristic amplitudes are associated with stronger volcanic tremor (Benoit et al.,

2003) and higher tremor amplitudes are associated with high ash column heights (McNutt, 1994); therefore, it is not surprising that characteristic amplitudes would also show positive correlation with maximum plume heights. Because the fits of the exponential law vs. the fits of the power law and the slopes of the duration-amplitude plots appear to vary with the presence of volcanic activity, possibilities exist for the use of r^2_{exp} vs. r^2_{pow} and characteristic amplitudes in volcano forecasting and monitoring.

Fitting of the duration-amplitude plots is related to other factors besides the actual volcano-seismic signal itself, however. The length of time chosen for calculating the fit will affect the results. If the duration of the actual tremor signal is very short compared to the overall time, the fit may be poor (e.g. January 27 and February 5-6 were not detected by this method). The presence of higher amplitude spikes with much greater amplitude than the underlying tremor, also affects the shapes of the curves and was more likely to result in a poor fit with the exponential law. Station distance from the source can affect curve-fitting also. A strong regional signal that is recorded on multiple stations near in time to a local volcanic signal may overshadow the volcanic signal at stations more distant from the vent, causing a greater relative difference in amplitudes between the volcanic and regional event and resulting in poorer curve fitting at the distant stations.

6.6.2. Types of events

Benoit et al. (2003) attempted to answer the question of whether volcanic tremor is a distinct process with a different source mechanism than low-frequency earthquakes, or merely the superposition of many low-frequency events. If volcanic tremor obeys an exponential law, while earthquakes obey a power law, then tremor is probably a distinct process from low-frequency earthquakes (Benoit et al., 2003). However, duration-amplitude plots of the Redoubt 1989 eruption were studied and the exponential law was found to be a better fit to pre-eruptive low-frequency earthquakes than the power law ($r^2_{exp} = .95$ compared to $r^2_{pow} = .88$, Benoit et al., 2003). During this eruption, low frequency earthquakes were observed to increase in rate until they merged into volcanic tremor (Power et al., 1994), therefore, in the case of Redoubt 1989-1990, at least, tremor and low-frequency earthquakes are more closely related.

This paper is largely an extension of Benoit et al. (2003), however, similar research has been done on slow earthquakes, or non-volcanic tremor. Slow earthquakes which accompany slow-slip events have also been shown to obey a power law (Ide et al., 2007). Tremor due to slow earthquakes also appears to be due to numerous low frequency earthquakes (Shelly et al., 2006). This result appear to be in contrast with the above reported results from Redoubt, in which the volcanic tremor, which is made up of low-frequency events, obeys an exponential law. Although the results are different from one another, it is likely that because the

earthquakes and tremor in both cases were most likely sharing a source process it is logical that they would also share similar scaling.

6.6.3. Transitions in exponential law fitting

A change in exponential fitting occurred after onset of the magmatic eruptions. Early in the eruption, dates for which $r^2_{exp} / r^2_{pow} \geq 1$, were less frequent even during strong tremor episodes, i.e., January 25, but not January 26 or 27, and February 7-8 but not February 6, 9, etc. However, following the onset of magmatic eruptions (March 23), more dates showed $r^2_{exp} / r^2_{pow} \geq 1$, despite the fact that tremor amplitudes were often low (<400 nm, see figs. 6.2 and 6.6I, for example). Other times after this point in which $r^2_{exp} / r^2_{pow} \geq 1$ do correspond with higher seismic amplitudes, but not tremor. Interestingly, between April 7 and May 4, the r^2 values of all the daily duration-amplitude plots using the exponential law are very high and do not drop below $r^2 = 0.8$ (fig. 6.13). The only other long period during which this is the case is January 24 to February 11, when three different tremor episodes occurred. Fee et al. (2011) note that after the March 26 explosions, the character of the eruption changed from subplinian to vulcanian, based on changes in infrasonic signals. Finer-grained tephra was observed beginning at this time as well (Wallace et al., 2011). These changes indicate a shift to more explosive activity (Buurman et al., 2012; Wallace et al., 2011; Fee et al., 2011). This change could be responsible for the shift in r^2 fits to the data. The exponential fitting, which first helped to identify the early changing conditions at the volcano that lead to the onset of tremor,

has also apparently identified this transition. As the underlying seismicity changes systematically, it is also reflected in the scaling

6.7. Conclusions

A better understanding of duration-amplitude relationships for volcanic tremor can be helpful for monitoring purposes and for a better understanding of the systematic changes of volcanic tremor. This study shows that duration-amplitude relationships for episodes of volcanic tremor and low-frequency earthquakes fit an exponential law. Background noise or low-level volcanic activity fit a power law distribution better in most cases, judging by r^2 values. Using the r^2_{exp} / r^2_{pow} method to detect volcanic seismic activity was most effective before the first magmatic eruptions occurred, suggesting that this method has potential for forecasting. Overall, the duration-amplitude plots generated during periods of tremor show a more continuous distribution of displacements, which makes for a better fit with the exponential law. When seismic signals overall are low, with a few sporadic high amplitude peaks occurring, the plots often show strong bends which makes for poorer fitting of an exponential law. Finally, maximum plume heights show correlation with characteristic amplitudes, albeit with some scatter. The low amplitude portion is usually noise and could be omitted from automated analysis.

Table 6.1. Main seismic episodes of the 2009 Redoubt eruption

Start date (UT)	Dur. (hrs)	Max D_{rms} (nm)	Low λ (1/nm)	Range λ (nm)	r^2_{exp}/r^2_{pow}
1/25/09 9:00	44	400†/300	0.008	50-145	1.14
1/30/09 0:00	24	375	0.009	75 - 325	1.1
2/5/09 19:00	100	225	0.023	55-110	1.05
2/16/09 12:00	42	225†/100	0.020	80-140	1.05
2/26/09 0:00*	36	600	0.008††	30-195	1.03
3/15/09 18:00	15	180	0.015	40-180	1.00
3/21/09 0:00*	48	150	0.049	0-150	1.11
3/23/09 0:00	48	800	0.004	300-500	1.14
3/26/09 12:00	108	600	0.011	50-560	1.14
4/1/09 00:00*	24	400†/300	0.022	45-175	1.05
4/4/09 12:00	9	550	0.003	180-425	1.14

*earthquake swarm

†isolated peaks

†† 2 distinct slopes, lower is shown

The data shown here includes precursory tremor episodes, two earthquake swarms, phreatic and magmatic eruptions. Columns 1 and 2 give the start date and duration of the episode, respectively. Columns 3 gives the maximum RMS displacement in nm. Columns 4, 5, and 6 give the flattest slopes (corresponding to strongest characteristic amplitude) as seen in figure 6.5, the range over which those slopes occurred (in nm), and the r^2 fit for the slopes, respectively.

Table 6.2. Data for 19 magmatic explosions in 2009 Redoubt eruption

Event[1]	Day[2]	Time[3] (UT)	DA span[4] (UT)	λ[5] (1/nm)	[1/λ][6] (nm)	[r^2][7]	Max Ht[8] (ft)	Max Ht[9] (km)
0	3/15/2009	21:05	21:00-22:00	0.021	48.08	0.84	15000	4.57
1	3/23/2009	6:34	06:00-07:00	0.010	104.17	0.98	18000	5.49
2	3/23/2009	7:02	06:59-07:30	0.005	204.08	0.95	44000	13.41
3	3/23/2009	8:14	08:00-09:00	0.004	285.71	0.83	48000	14.63
4	3/23/2009	9:38	09:30-12:00	0.005	188.68	0.96	43000	13.11
5	3/23/2009	12:30	12:15-13:30	0.005	204.08	0.95	60000	18.29
6	3/24/2009	3:40	03:30-04:30	0.005	200.00	0.88	60000	18.29
7	3/26/2009	16:34	16:00-17:00	0.018	55.25	0.98	27000	8.23
8	3/26/2009	17:24	17:00-18:00	0.004	227.27	0.95	62000	18.90
9	3/27/2009	7:47	07:00-08:00	0.014	70.42	0.9	41000	12.50
10	3/27/2009	8:28	08:10-09:10	0.009	116.28	0.97	49000	14.94
11	3/27/2009	16:39	16:00-17:00	0.006	166.67	0.91	51000	15.54
12	3/28/2009	1:34	01:00-02:00	0.007	138.89	0.93	48000	14.63
13	3/28/2009	3:24	03:00-04:00	0.007	147.06	0.91	50000	15.24
14	3/28/2009	7:19	07:00-08:00	0.010	104.17	0.97	48000	14.63
15	3/28/2009	9:19	09:00-10:00	0.007	142.86	0.93	48000	14.63
16	3/28/2009	21:40	21:00-22:00	0.006	175.44	0.94	17000	5.18
17	3/28/2009	23:29	23:10-00:10	0.010	101.01	0.93	41000	12.50
18	3/29/2012	3:23	03:20-04:20	0.010	102.04	0.93	48000	14.63
19	4/4/2009	13:58	13:50-14:50	0.005	222.22	0.84	50000	15.24

1,2,3: Event numbers, dates and times are from Webley (2012) and Schaefer (2012)

4: Time span over which DA plots were generated (typically 1 hr, shorter if multiple events occurred closely together; longer if the event lasted longer than 1 hour)

5: Slope of whole plot

6: Inverse of λ from 5.

7: r2 of slope fitting from 5

8: Maximum plume height in ft, determined by USGS radar and FAA NEXRAD radar, as reported in Webley (2012) and Schaefer (2012)

9: Maximum plume height converted to km

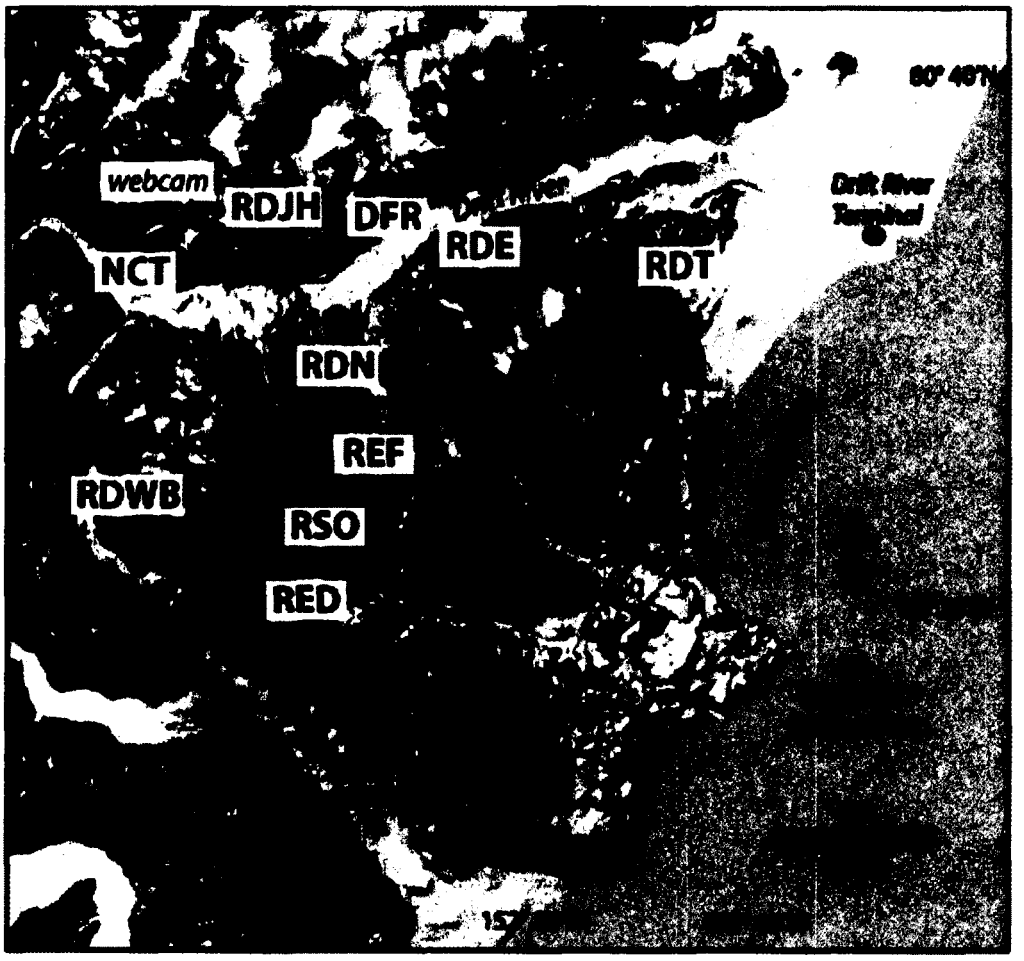

Figure 6.1

Map of Redoubt volcano showing seismic stations. Seismic stations are depicted by squares. Of the stations, RDJH and RDWB are broadband; RED and REF are three-component short period, the rest are single component short period. The short period stations are analog telemetered and digitized at 100 samples per second in the AVO seismology laboratory. Redoubt is located in Cook Inlet, in south central Alaska. Image courtesy of the AVO/ADGGS and J. Schaefer.

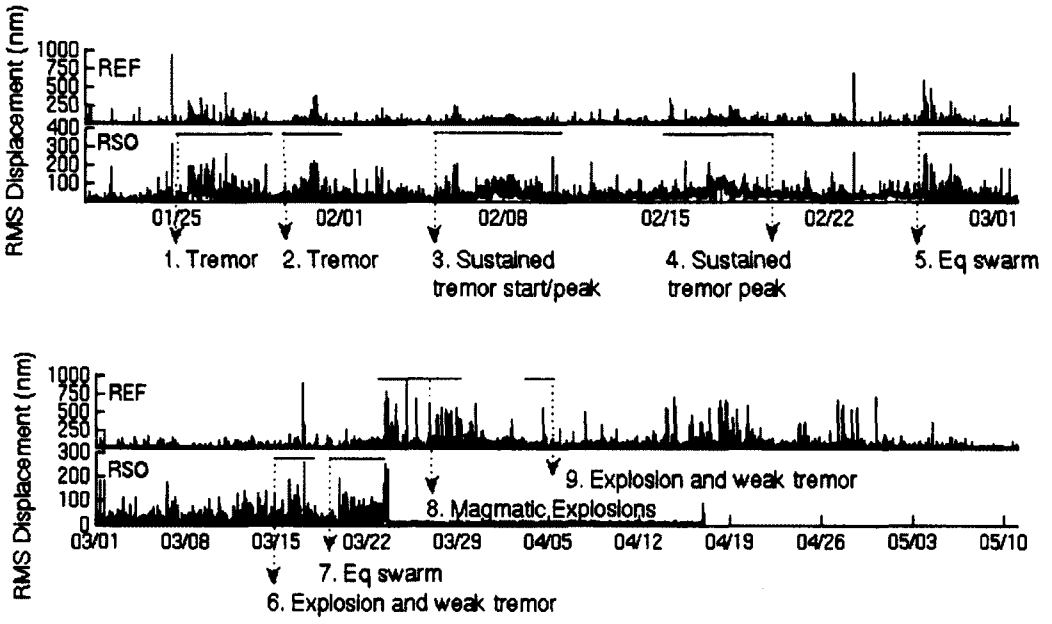

Figure 6.2

Seismic amplitude displacements of 2009 Redoubt eruption sequence. The seismic data was recorded on stations RSO and REF, with the tremor episodes labeled. Tremor began to occur in late January. The first explosion occurred March 15, 2009. Note that station RSO stopped functioning soon after the first magmatic eruptions on March 23, 2009.

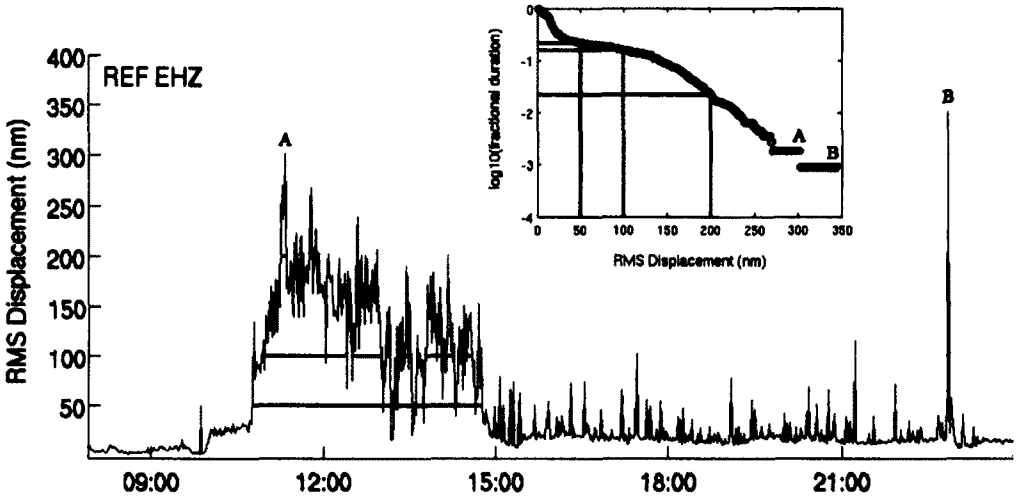

Figure 6.3

Generation of duration-amplitude plots from seismic data. Each point on the inset plot is the cumulative duration (log 10 fractional duration) at or above a specific amplitude (green = 50 nm, blue = 100 nm, red = 200 nm). The inset figure shows the duration amplitude distribution generated. Note the relation of the two highest peaks and their appearance on the inset plot as well.

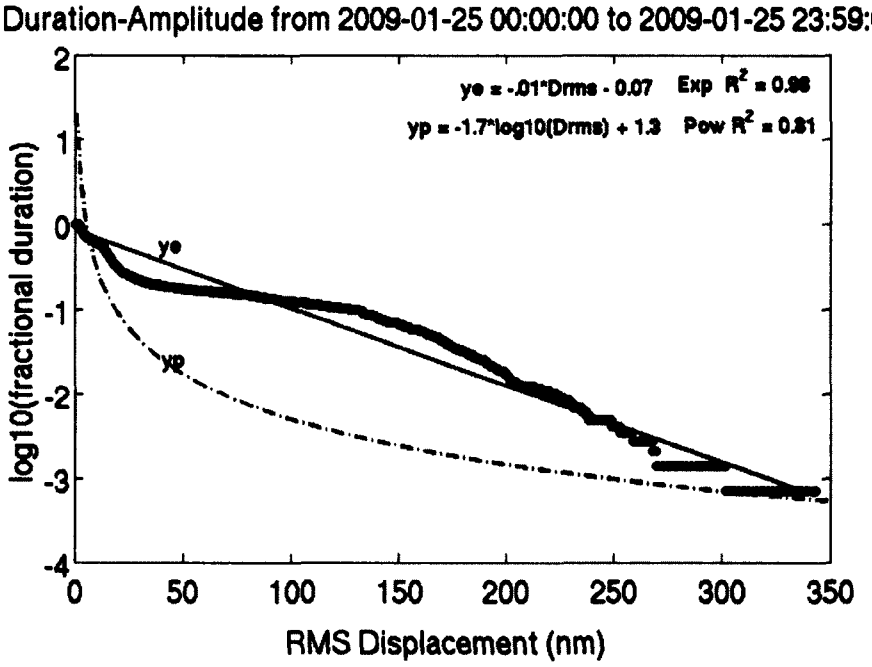

Figure 6.4

Comparison of exponential and power law fits. Duration amplitude distribution of a duration of 1 day of seismic data (during which volcanic tremor occurred) shown with lines fit with an exponential law (y_e) and a power law (y_p). The r^2 fits for the exponential law and power law are 0.98 and 0.81, respectively, making r^2_{exp} / r^2_{pow} = 1.21. Note that power law fits are estimated from a log-log plot, but are shown here on a semi-log plot.

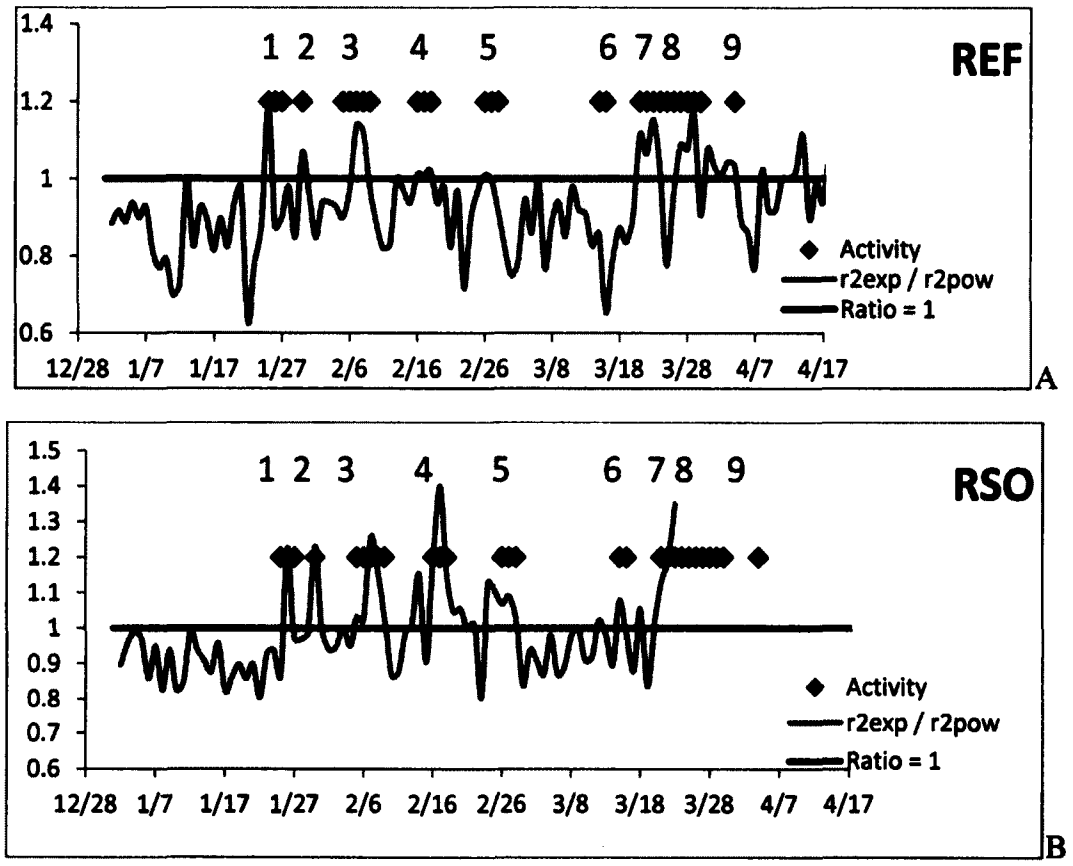

Figure 6.5

Plot of r^2_{exp} / r^2_{pow} by day, for stations REF and RSO. A) shows REF and B) shows RSO. Periods of volcanic activity generally correspond with periods on this plot when the r^2 of the exponential law is greater than that of the power law. Note that station RSO stopped working March 23, 2009. The black line shows the marks where $r^2_{exp} / r^2_{pow} = 1$. The blue markers (whose position on the y-axis is arbitrary) denote days in which volcanic seismic activity was reported to be occuring and are numbered as in figure 6.2.

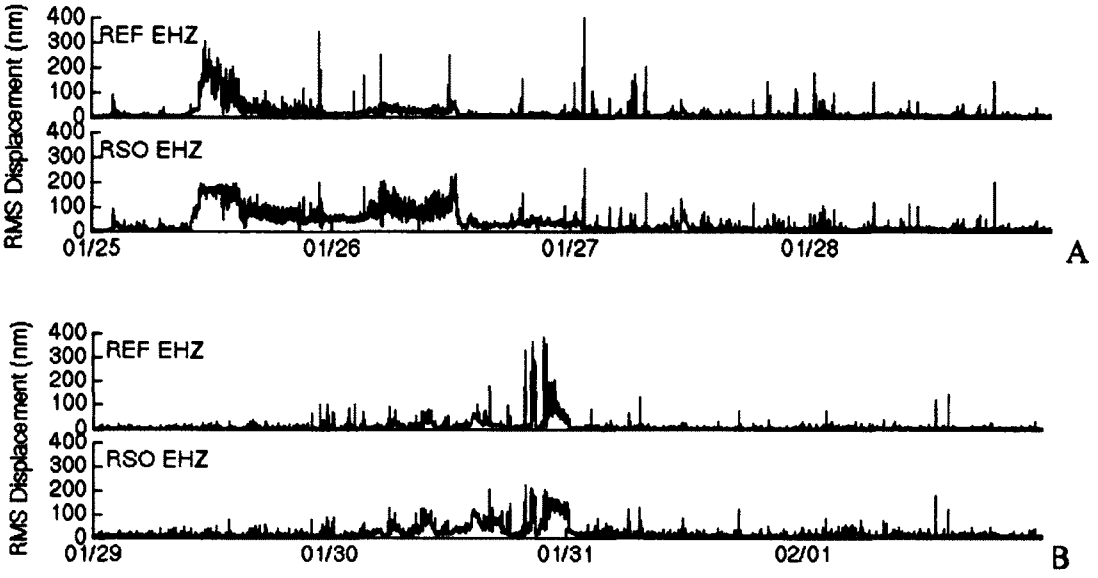

Figure 6.6

Displacement plots of the main tremor and earthquake swarm episodes. The major tremor and earthquake swarm episodes of the 2009 eruption are shown on stations REF and RSO, plotted to the scale of the longest episode. A) shows high-amplitude tremor beginning January 25, B) shows another similar episode beginning January 30 , C) marks the beginning of the sustained tremor phase and D) is a peak within this sustained phase, E) is an earthquake swarm, F) is an episode of weak tremor accompanying the first (phreatic) explosion, and G) and H) shows the magmatic eruptions and their accompanying earthquakes swarms and tremor, and I) shows the final magmatic eruption of April 4, plus weak tremor leading up to it. Note the different scale for station REF in part F and that station RDN has replaced RSO for plots G and H.

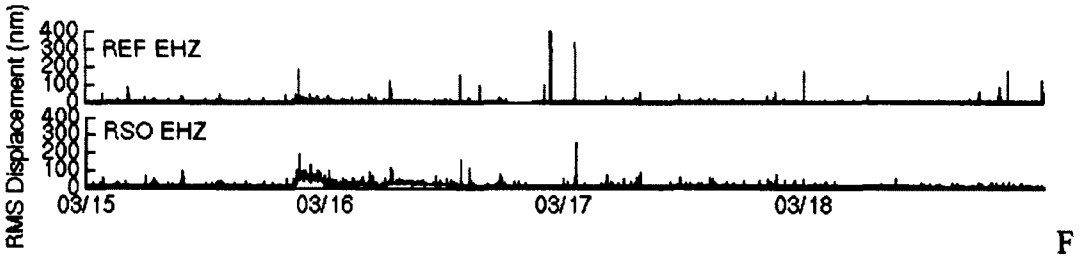

F

Figure 6.6 continued


RMS Displacement (nm)
400
300
200
100
0
REF EHZ
RSO EHZ
02/06
02/07
02/08
02/09

C

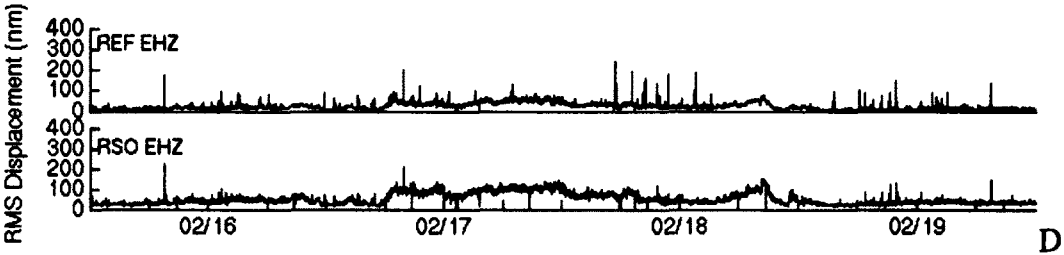
RMS Displacement (nm)
400
300
200
100
0
REF EHZ
RSO EHZ
02/16
02/17
02/18
02/19

D

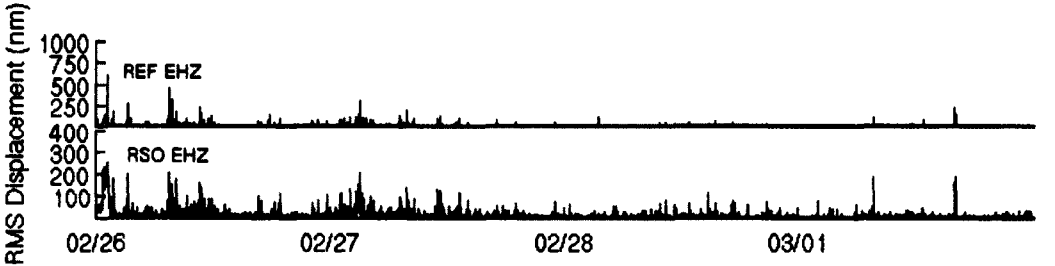
RMS Displacement (nm)
1000
750
500
250
400
300
200
100
REF EHZ
RSO EHZ
02/26
02/27
02/28
03/01

E

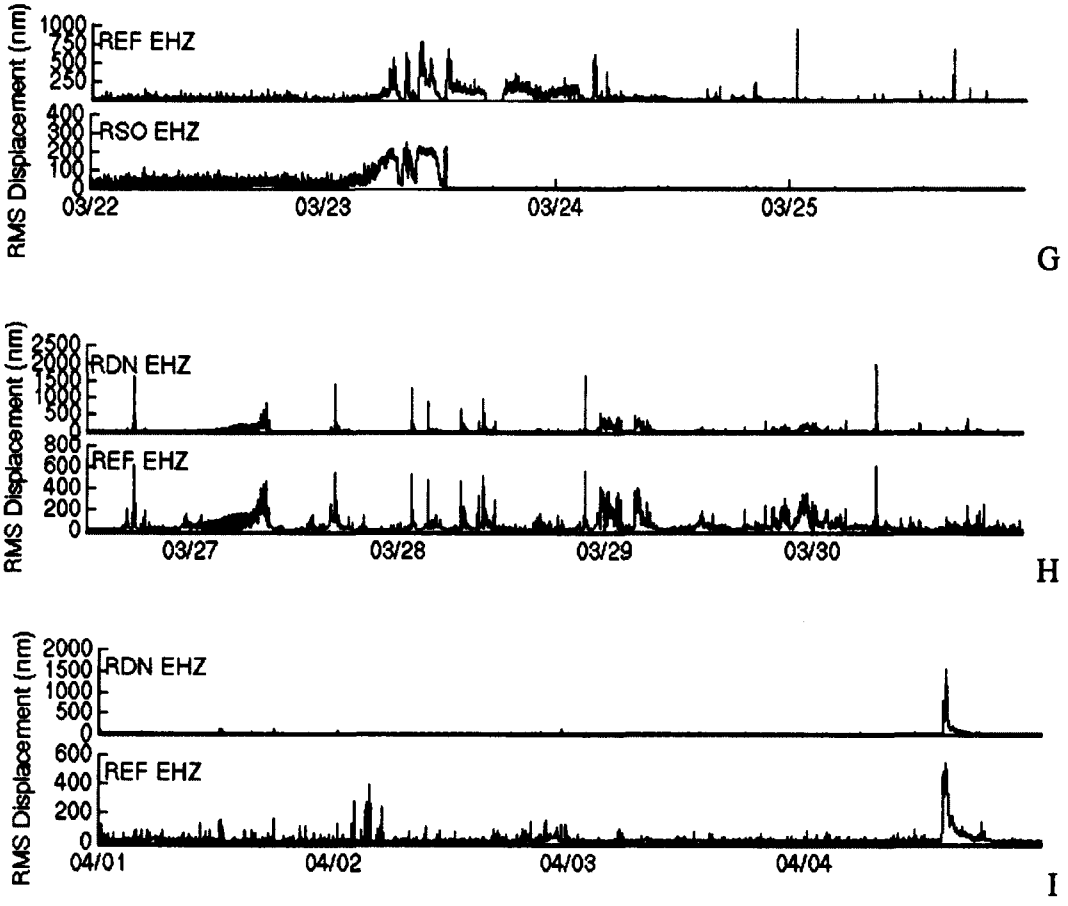

Figure 6.6 continued

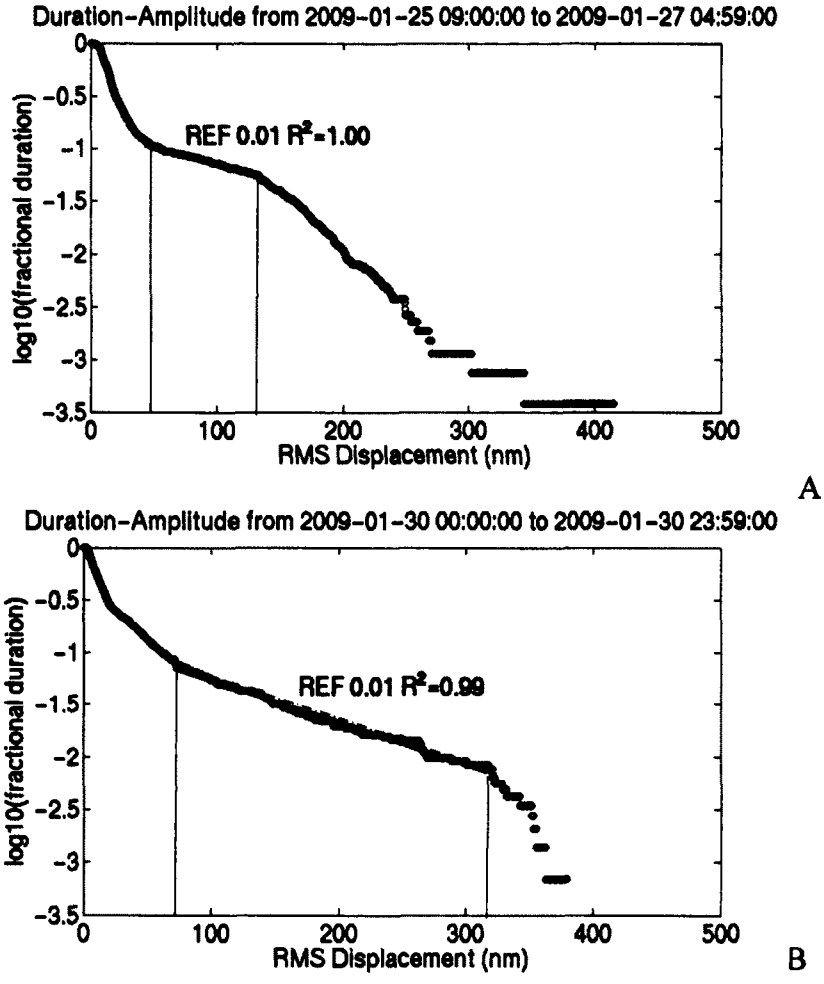

Figure 6.7

Duration-amplitude plots for seismic episodes shown in figure 6.6. The letter labels correspond to those of figure 6.6. The vertical axes show duration of the signal ($\log_{10}$ fractional duration) at the RMS displacement (in nm) shown in the horizontal axes. Note the change in the amplitude scales. A) and B) show the first two precursory January tremor episodes, and both have similar slopes, corresponding to similar characteristic amplitudes.

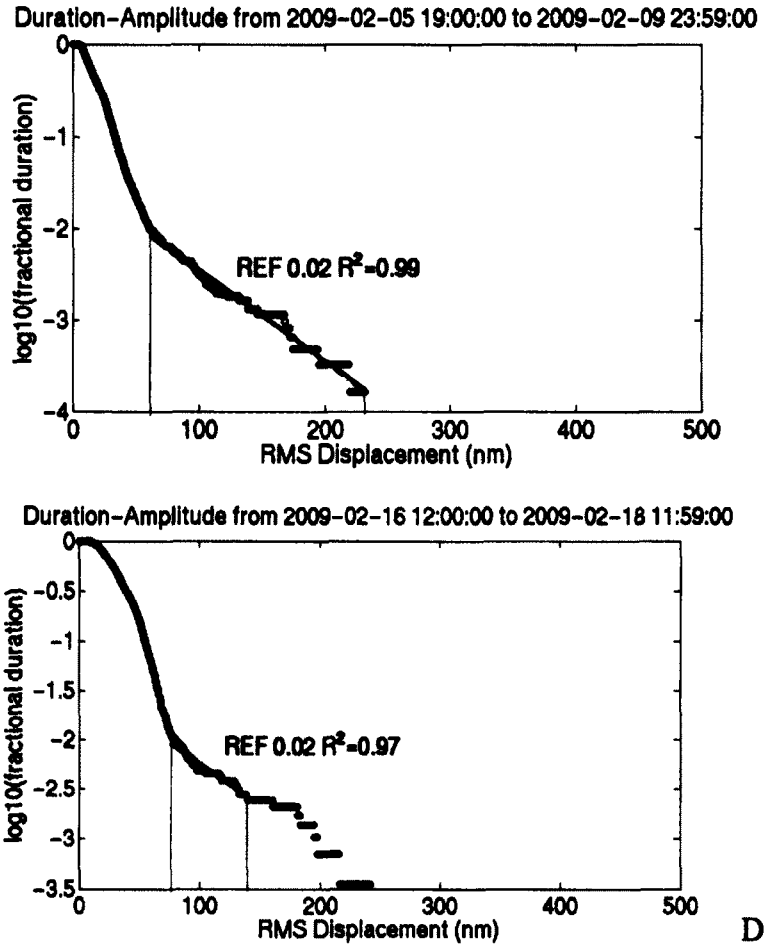

Figure 6.7 continued

C) and D) show two higher amplitude tremor 'peaks' that occurred during the sustained tremor of February and March, both of which $\lambda = 0.02$, for similar characteristic amplitudes.

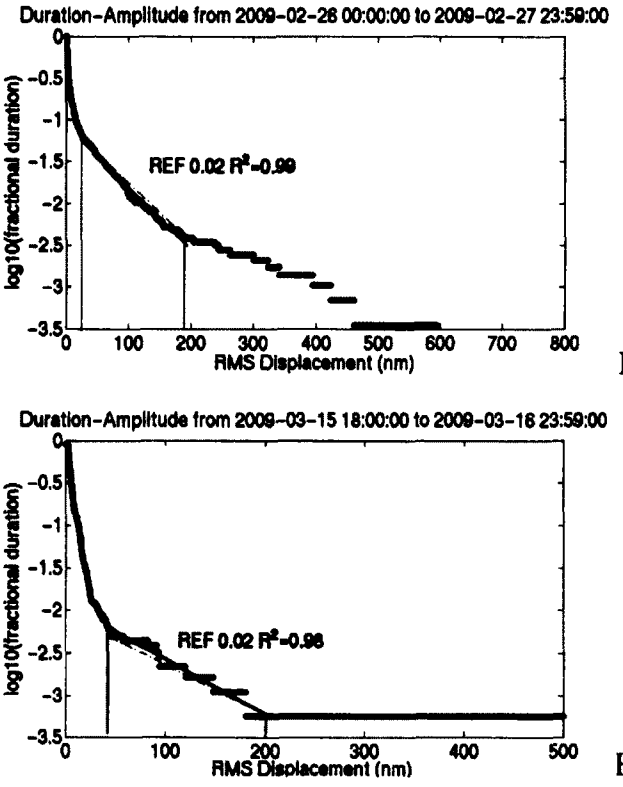

Figure 6.7 continued

E) shows the first of the earthquake swarms. The swarm of Feb. 26 shows two linear segments, the first of which shows $\lambda = 0.02$ (shown here), the second segment has a slope of .008 (see table 1), for a stronger characteristic amplitude. The value of $\lambda = 0$ .02 is similar to that of the two previous tremor episodes. F) shows the phreatic explosion of March 15. (Note that this episode was identified by the r^2_{exp} / r^2_{pow} method on station RSO, but not REF).

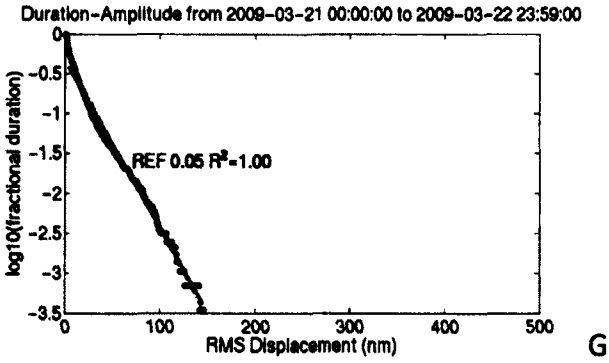

G1

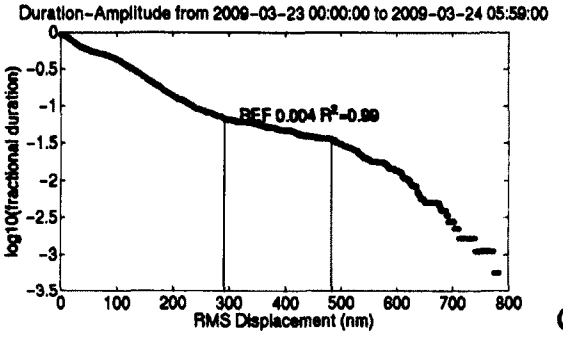

G2

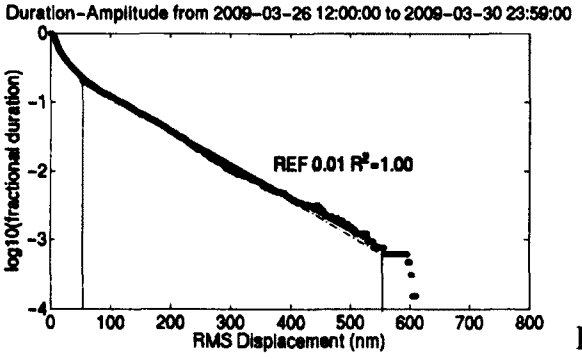

H

Figure 6.7 continued

G1) shows the second earthquake swarm preceeding the magmatic explosions, which has a weaker characteristic amplitude (steeper slope) than E. G2) and H) show the first 18 magmatic explosions. G2) shows the strongest signal so far, with the lowest slope, while H) is closer to that seen in A) and B).

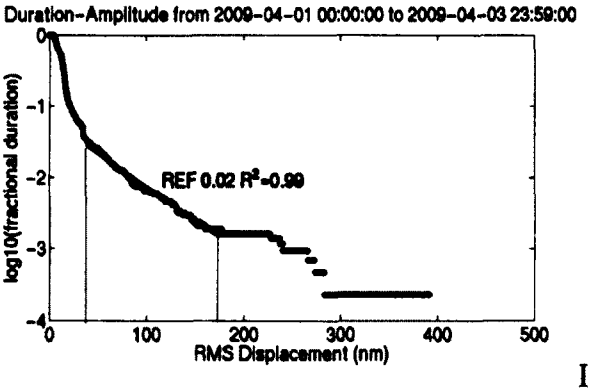

I

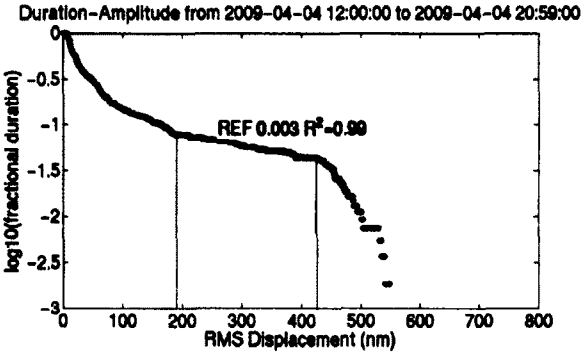

I2

Figure 6.7 continued

I) shows the earthquake swarm and low-level tremor leading up to the final explosion seen in I2). I) has a slope close to the other earthquake swarm from Feb. 26 seen in E. I2) shows a very strong signal, the highest characteristic amplitude (lowest slope) seen.

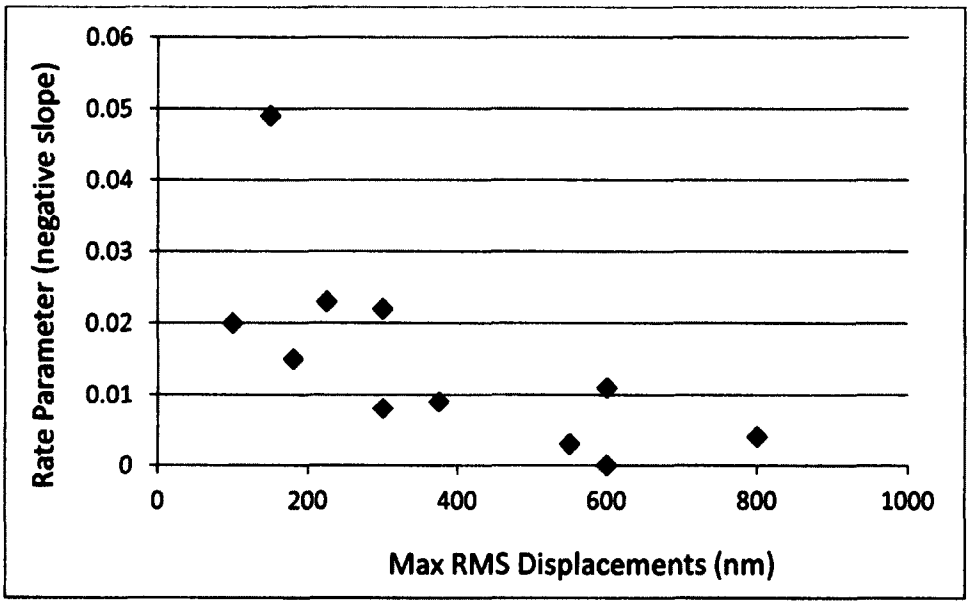

Figure 6.8

Plot of rate parameters vs. maximum displacements. The rate parameters corresponding to the flattest slopes were plotted against the maximum displacements seen in a tremor or earthquake swarm episode and also listed in Table 1. The flattest slopes tend to occur with seismic data with the highest displacements. Although the DA plots in some cases show multiple slopes only the lowest are used.

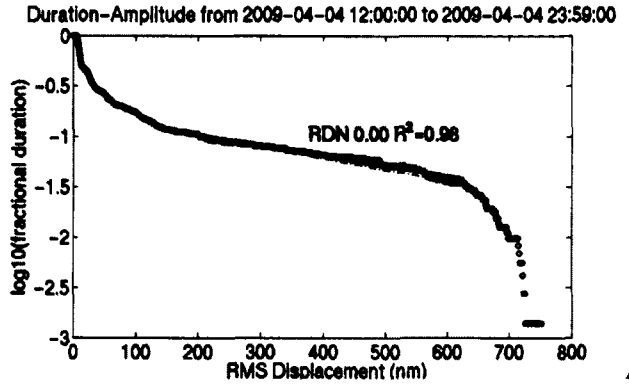

A

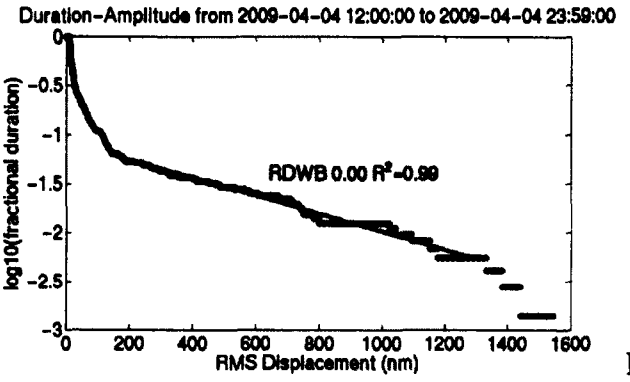

B

Figure 6.9

Comparison of duration-amplitude plots at different stations. The duration-amplitude plots for four different stations were generated for the April 4th explosion, for stations A) RDN, B) RDWB, C), RED and D) REF. Although variations exist in the shape of the curves between stations, all stations have very low slopes of $\lambda <$ 0.01 (RDN: $\lambda = 0.002$, RDWB: $\lambda = 0.002$, RED: $\lambda = 0.003$, REF: $\lambda = 0.003$). This is an example of a very strong signal having the same or nearly the same characteristic amplitude at different stations.

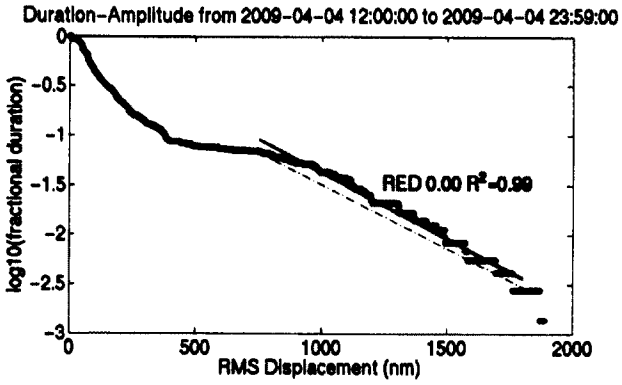

C

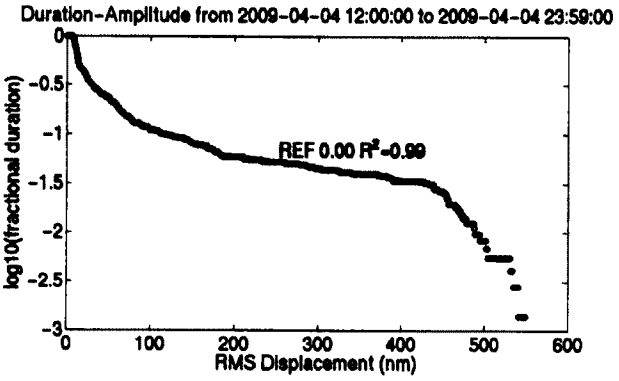

D

Figure 6.9 continued

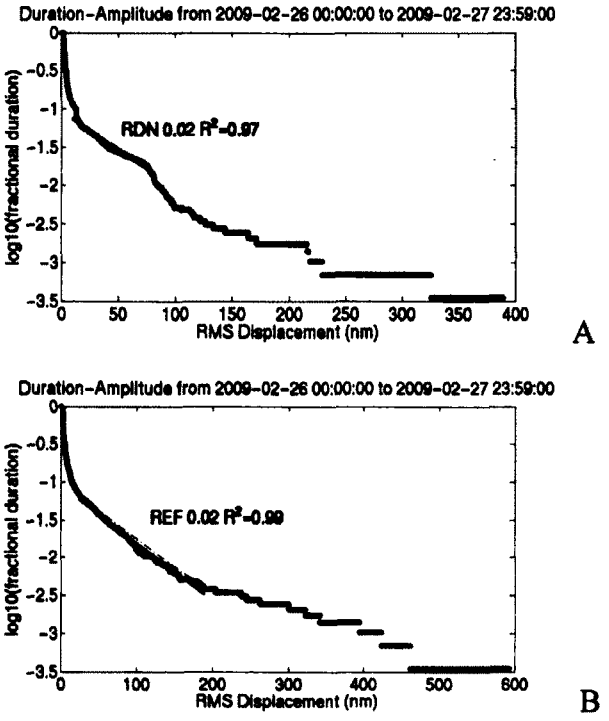

Figure 6.10

Comparison of duration-amplitude plots at different stations . These examples of duration-amplitude plots for seismic episodes are from three different stations: A) RDN, B) REF, and C) RSO. The event shown here is the earthquake swarm of Feb. 26-28. Amplitudes are lower than in figure 6.9. Station RSO is closest to the vent. Each station shows a slope at some part of the plot that is equal to $\lambda = 0.02$, although variations that are likely due to noise and/or site effects change the shape of each plot slightly. RDN and REF show flattening of the curve at higher displacements, while RSO shows saturation at the high displacements. Distance of the station from the vent also effects the amplitudes.

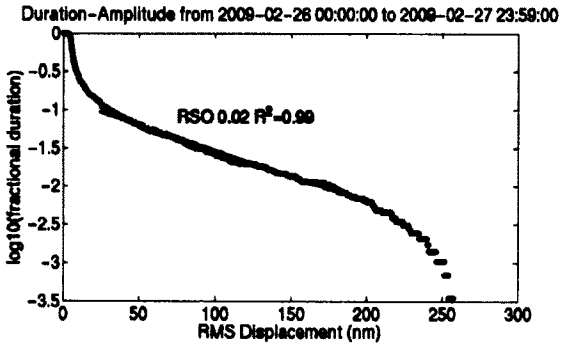

C

Figure 6.10 continued

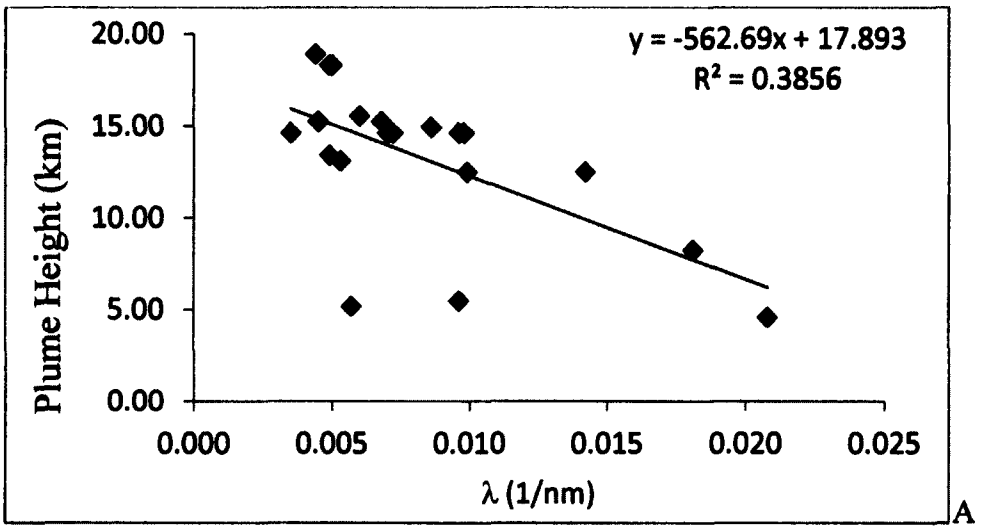

Figure 6.11

Maximum plume heights vs. rate parameter and inverse rate parameter. Maximum plume heights were determined by Webley et al. (2012) and are also reported in Schaefer (2012). 1 phreatic explosion and 19 magmatic explosions are plotted against A) the duration-amplitude rate parameter and B) the inverse of λ as determined by an exponential duration-amplitude distribution. The inverse of λ is proportional to the characteristic amplitude of the volcanic tremor. The plots show a correlation between plume heights and slopes of DA plots and characteristic amplitude. The duration-amplitude plots were generated for about 1 hour of data for each explosion unless shorter times were needed when multiple explosions occurred closely together within a short time. Although the plots show scatter, the correlation between plume heights and low slopes, and therefore stronger average signals, exists.

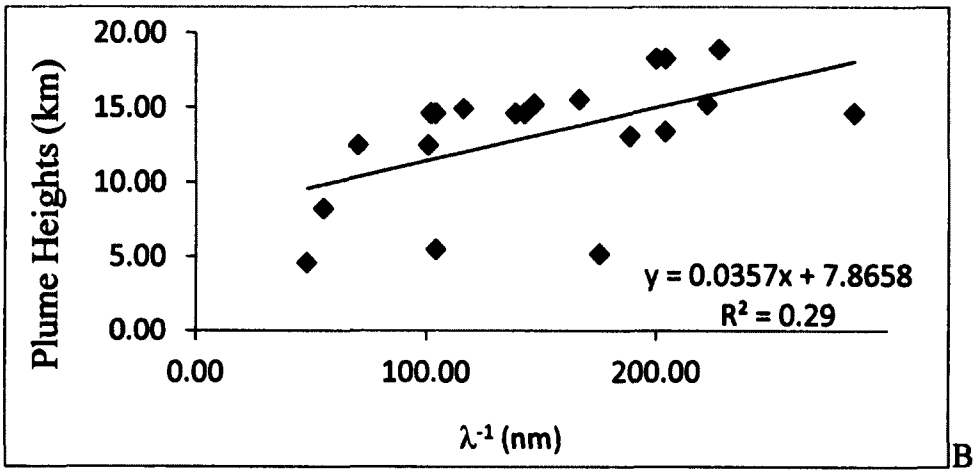

B

Figure 6.11 continued

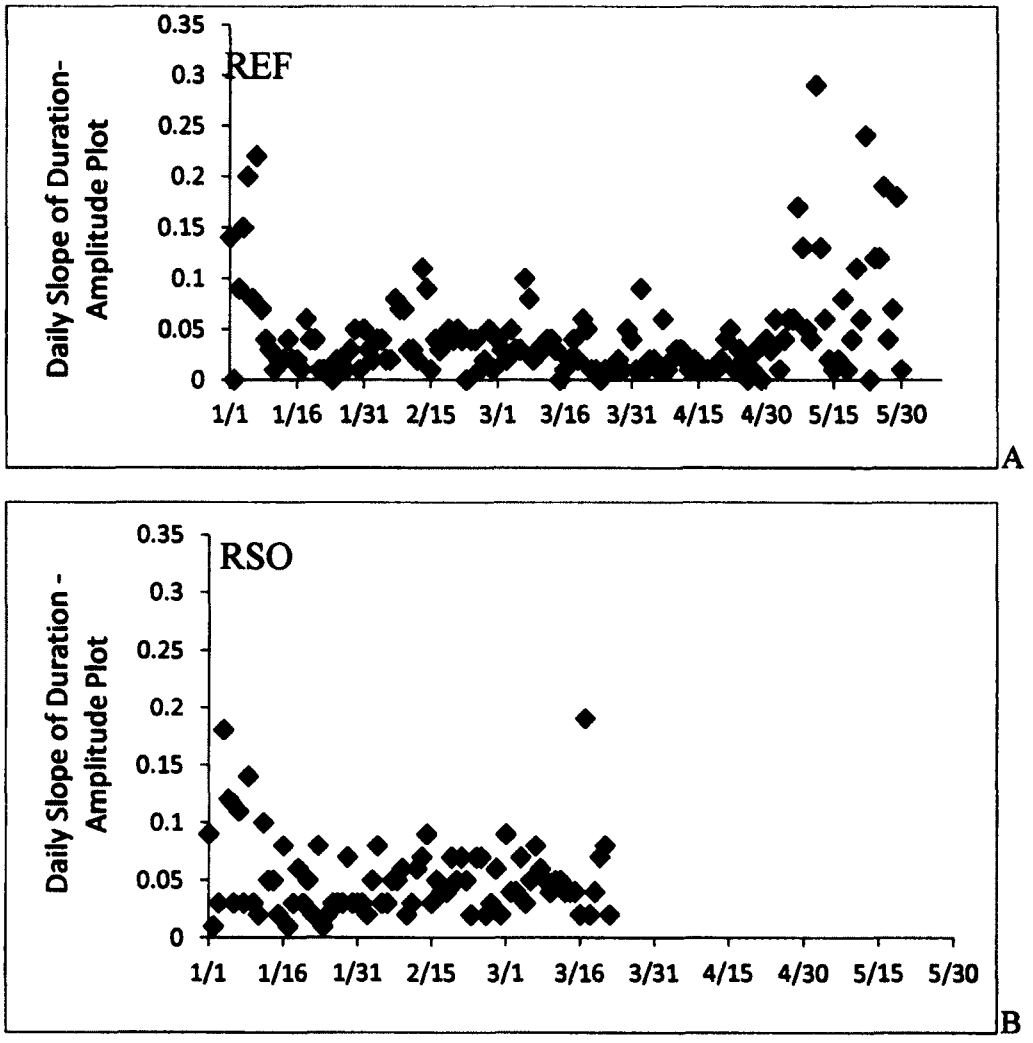

Figure 6.12

Daily slopes of duration-amplitude plots at stations REF and RSO. The slope, or inverse characteristic amplitude, of the duration-amplitude are plotted for 1 day at a time for stations A) REF and B) RSO. Lower slopes (λ) correspond to stronger signals (higher characteristic amplitudes (λ^{-1})). Note the persistently low values during the main explosive phase from March 22 to April 4, 2009.

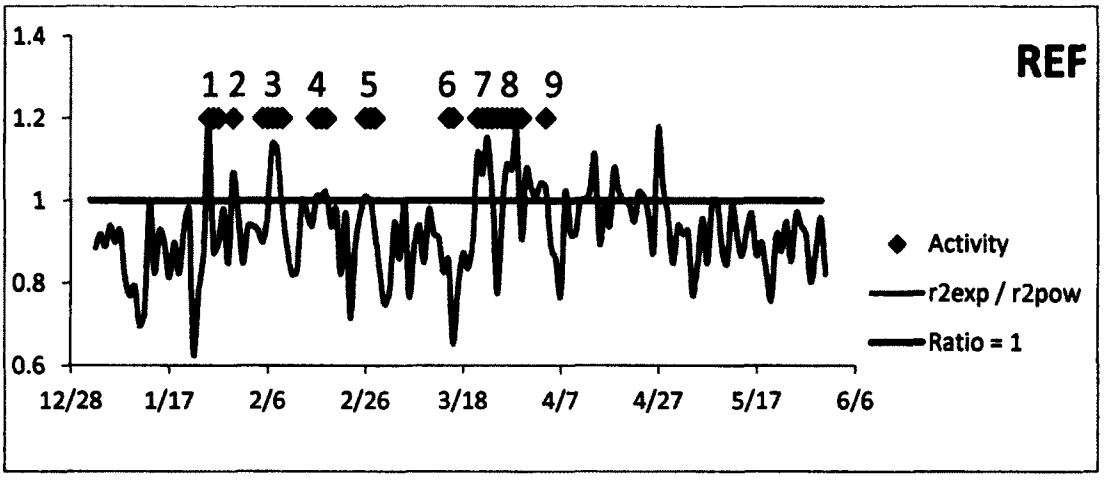

Figure 6.13

Plot of r^2_{exp} / r^2_{pow} for station REF extended to the end of May. The plot is figure 6.4, extended to the end of May, to show a change in the exponential fitting. Many more days show $r^2_{exp} / r^2_{pow} \geq 1$ after the end of March, although they do not obviously correlate with tremor episodes or earthquake swarms. Dates which showed $r^2_{exp} / r^2_{pow} \geq 1$ occurred on April 8, 13-14, 23, 28, and May 8-9, and these dates sometimes correspond with higher amplitudes of seismic activity. On April 13, seismic amplitudes reached 250 nm, 700 nm on April 14, and 550 nm on April 28. Seismic amplitudes only reached 100 nm on both April 8 and 23, however, and on May 8-9, the amplitudes are lower, less than 50 nm. The change in exponential fitting may reflect a systematic in underlying seismicity associated with the changing conditions at the volcano related to the transition from before to after the pre-magmatic explosions.

6.8. References

Benoit, J. P., McNutt, S.R., Barboza, V., 2003. Duration-amplitude distribution of volcanic tremor. Journal of Geophysical Research, 108, B3, 2146, doi:10.1029/2001JB001520.

Buurman, H., West, M., Thompson, G., 2012. The Seismicity of the 2009 Redoubt Eruption. Journal of Volcanology and Geothermal Research, Special Issue on the 2009 Redoubt Eruption. http://dx.doi.org/10.1016/j.jvolgeores.2012.04.024

Endo, E. T., Murray, T., 1991. Real-time seismic amplitude measurement (RSAM): a volcano monitoring and prediction tool. Bulletin of Volcanology, 53, p. 533-545.

Fee, D., McNutt, S.R., Lopez, T.M., Arnoult, K.M., Szuberla, C.A.L., Olson, J.V., 2011. Combining Local and Remote Infrasound Recordings from the 2009 Redoubt Volcano Eruption. Journal of Volcanology and Geothermal Research, Special Issue on the 2009 Redoubt Eruption. DOI: http://www.dx.doi.org/10.1016/j.jvolgeores.2011.09.012.

Fehler, M., 1983. Observations of volcanic tremor at Mount St. Helens volcano. Journal of Geophysical Research, 88, p. 3476-3484.

Gutenberg, B., Richter, C.F., 1956. Magnitude and energy of earthquakes. Annali di Geofisica, 9, p. 1-15.

Ide, S., Beroza, G.C., Shelly, D.R., Uchide, T., 2007. A scaling law for slow earthquakes. Nature, 447, p. 76-79.

McNutt, S. R., 1994. Volcanic tremor amplitude correlated with Volcanic Explosivity Index and its potential use in determining ash hazards to aviation. Acta Vulcanologica, 5, p.193-196.

Mogi, K., 1962. Study of elastic shocks caused by the fracture of heterogeneous materials and its relations to earthquake phenomena. Bulletin of Earthquake Research Institute, University of Tokyo, 40, p. 125-173.

Peck, L., 2008. Overview of seismic noise and its relevance to personnel detection. ERDC/CRREL TR-08-5. Hanover, NH. U.S. Army Engineer Research and Development Center.

Peterson, J. 1993. Observations and modeling of seismic background noise. Open-file report 93-322. Washington, D.C., U.S. Geological Survey.

Power, J.A., Lahr, J.C., Page, R.A., Chouet, B.A., Stephens, C.D., Harlow, D.H., Murray, T.L., Davies, J.N., 1994. Seismic evolution of the 1989-1990 eruption sequence of Redoubt Volcano, Alaska. Journal of Volcanology and Geothermal Research, 62, p. 69-94.

Schaefer, J.R., ed., 2012. The 2009 eruption of Redoubt Volcano, Alaska. Contributing authors: Bull, K., Cameron, C., Coombs, M., Diefenbach, A., Lopez, T., McNutt, S.R., Neal, C., Payne, A., Power, J., Schneider, D., Scott, W., Snedigar, S., Thompson, G., Wallace, K., Waythomas, C., Webley, P.,

Werner, C., Alaska Division of Geological & Geophysical Surveys Report of Investigation 2011-5, 45 p.

Scholtz, C., 1968. The frequency-magnitude relation of microfracturing in rock and its relation to earthquakes. Bulletin of the Seismological Society of America, 58, p. 399-415.

Shelly, D.R., Beroza, G.C., Ide, S., Nakamula, S., 2006. Low-frequency earthquakes in Shikoku, Japan, and their relationship to episodic tremor and slip. Nature, 442, p. 188-191.

Wallace, K., Schaefer, J., Coombs, M., 2011. Character, mass, distribution, and origin of tephra-fall deposits from the 2009 eruption of Redoubt Volcano, Alaska. Journal of Volcanology and Geothermal Research, Special Issue on the 2009 Redoubt Eruption. In review.

Warren, N.W., Latham, G.V., 1970. An experimental study of thermally induced microfracturing and its relation to volcanic seismicity. Journal of Geophysical Research, 75, p. 4455-4464.

Webley, P.W., Lopez, T.M., Ekstrand, A.L., Dean, K.G., Rinkleff, R., Dehn, J., Cahill, C.F., Wessels, R.L., Bailey, J.E., Izbekov, P., Worden, A., 2012. Remote observations of eruptive clouds and surface thermal activity during the 2009 eruption of Redoubt Volcano. Journal of Volcanology and Geothermal Research. http://dx.doi.org/10.1016/j.jvolgeores.2012.06.023

Werner, C.A, Kelly, P.J., Doukas, M.P., Pfeffer, M.A., Evans, W.C., McGimsey,

R.G., Neal, C.A., 2009. Airborne measurements of gas emissions during the 2009 eruption of Redoubt Volcano, Alaska. American Geophysical Union, Fall Meeting 2009, abstract #V43A-2218.

Wyss, M., 1973. Towards a physical understanding of the earthquake frequency distribution. Geophysical Journal of the Royal Astronomical Society, 31, p. 341-359.

Chapter 7

Conclusions

Eruptions at three Alaskan volcanoes were studied in this thesis in an attempt to deepen understanding of the relationship between volcanic activity and seismicity. The relationship of the physical characteristics of volcanic hazards and their accompanying seismic waves is a recurring theme in this thesis. Tracking rockfall paths, rockfall sizes, and plume heights with seismicity is useful, because seismic monitoring can be done in real time, 24 hours a day, regardless of weather, dangerous conditions or distance. To this end, the eruptions of Veniaminof in 2005, Augustine Volcano in 2006, and Redoubt Volcano in 2009, have been studied with the focus on understanding how seismic recordings and measurements are related to physical characteristics of eruption manifestations.

In Chapter 2, the focus of the 2005 eruption of Veniaminof was the relationship of the ash plumes to the explosion earthquakes that accompanied them. Results showed that the Veniaminof ash plumes were small enough to be modeled by kinetic energy considerations, which may also be determined from seismicity to an extent, and showed a positive correlation with seismic amplitudes and magnitudes. These results, combined with the fact that virtually every plume was accompanied by an earthquake shows that the Veniaminof eruption can be accurately tracked by seismicity in real-time. The importance of seismic monitoring at volcanoes such as

Veniaminof, which have frequent small eruptions (VEI 1 to 2) can be seen from these results.

Chapters 3 and 4 dealt with the 2006 eruption at Augustine Volcano and the rockfalls and block-and-ash flows it produced. In Chapter 3, the large number of rockfalls occurring prior to the eruption were initially unrecognized as an eruption precursor. If increase in rockfall occurrence is to be seen as an eruption precursor, then understanding the relation of weather and seasons to the occurrence patterns of rockfalls is necessary, so that anomalies may more easily be detected. The events that occurred in the background, pre-eruptive, eruptive, and post-eruptive periods at Augustine show that a combination of seasonal effects and instability due to heating and lubrication due to gases and steam, as well as lava dome growth, may be responsible for the changing patterns and numbers of rockfalls. In Chapter 4 the block-and-ash flows and their seismicity is studied. Similar to the visual and seismic recordings of ash plumes discussed in Chapter 2, at Augustine, numerous ash plumes and their accompanying seismicity were recorded. Again the size of the rockfalls showed a correlation with the amplitudes and magnitudes of the seismic recordings. Also, the AUE/AUW seismic amplitude ratios of block-and-ash flows showed a correlation with the paths of the block-and-ash flows down the volcano. Seismic analysis of flow events can provide hazard monitoring information on directions, durations, sizes and run-out distances. Although the seismic energies of the flow events were low, the low seismic efficiencies but high event numbers mean that a tremendous amount of volcanic energy was released through the flow events. Again

the results from this chapter show that visual data provides confirmation that seismic data alone can track the course of the eruption.

Chapters 5 and 6 deal with reduced displacements, a measurement frequently made for volcanic tremor. When interpreting reduced displacements and other seismic measurements from volcanoes, it is important to keep in mind the effects that other factors besides the volcanic signal, such as site effects, can have. Chapter 5, while simple, shows how an artifact of computing reduced displacement can skew DR measurements in the absence of a sufficiently strong signal from the source. This fact should be taken into account during everyday volcano monitoring as well as with studies involving reduced displacement. A better understanding of duration-amplitude relationships of volcanic tremor can be helpful for monitoring purposes and for a better understanding of the systematic changes of volcanic tremor. The results of chapter 6 show that duration-amplitude relationships of volcanic tremor and low-frequency earthquakes fit an exponential law. Background noise or low-level volcanic activity fit a power law distribution better in most cases, judging by r^2 values. Using the $r^2_{exp} > r^2_{pow}$ method to detect volcanic seismic activity was most effective before the first magmatic eruptions occurred, suggesting that this method has potential for forecasting.

Each part of this thesis contributes something unique to the fields of volcano monitoring and volcano seismology. Opportunities for further study are present in all topics. The installation of more webcameras at volcanoes with higher resolution and high sampling rates would allow for more opportunities for comparisons of

visual observations of volcanic hazards and activity and their seismicity. Duration-amplitude relationships may be able to give more insight into the source processes of volcanic tremor. Further analyses in conjunction with in depth modeling of source processes of volcanic tremor and low frequency events could prove useful. Further analyses of duration-amplitude relationships in conjunction with in depth modeling of source processes of volcanic tremor and low frequency events could provide insight into the source processes of volcanic tremor.

Appendix A

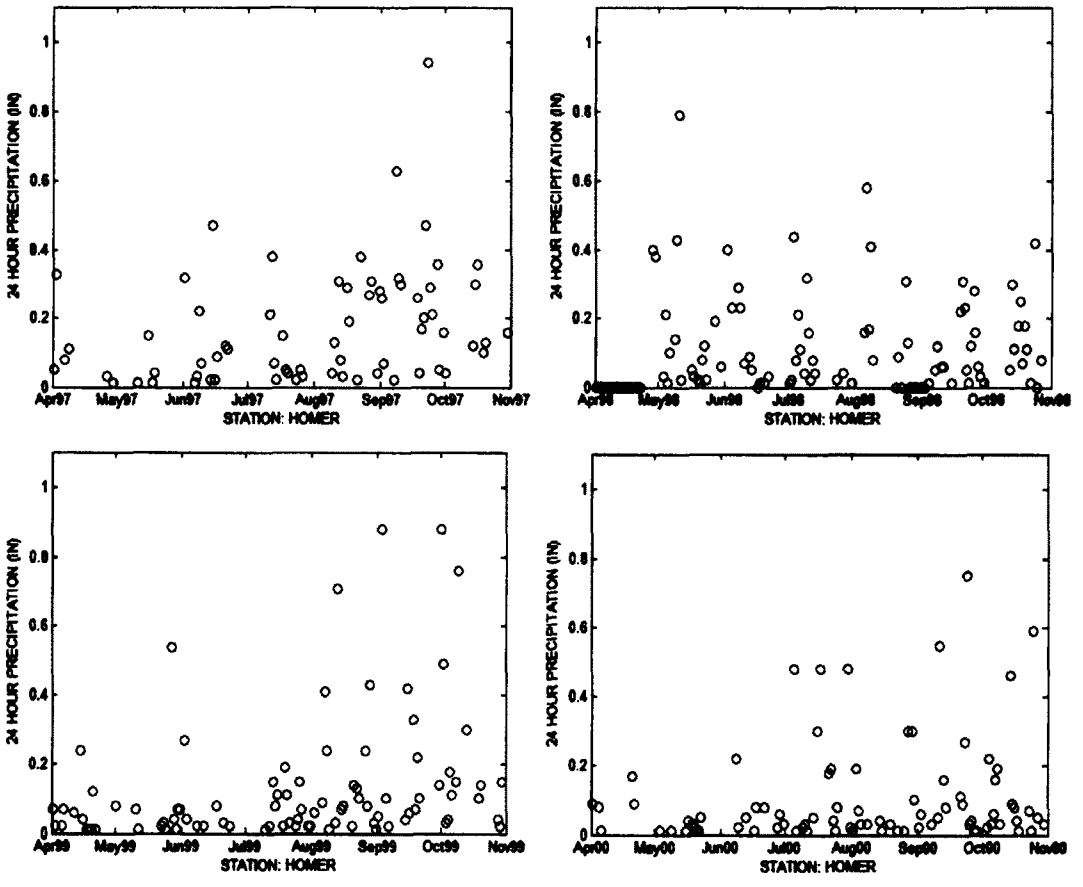

Figure A1

Rainfall data from Homer, AK for 1997-2009. Data is from the National Climate Data Center. Seven months data are shown for each year. The recorded rainfall in inches per 24 h at Air Force Catalog Station Number (USAF) 703604- station located in Homer, AK, 112 km from Augustine Island. Note that 2002 is omitted, because only one rockfall was recorded that year.

Figure A1 continued

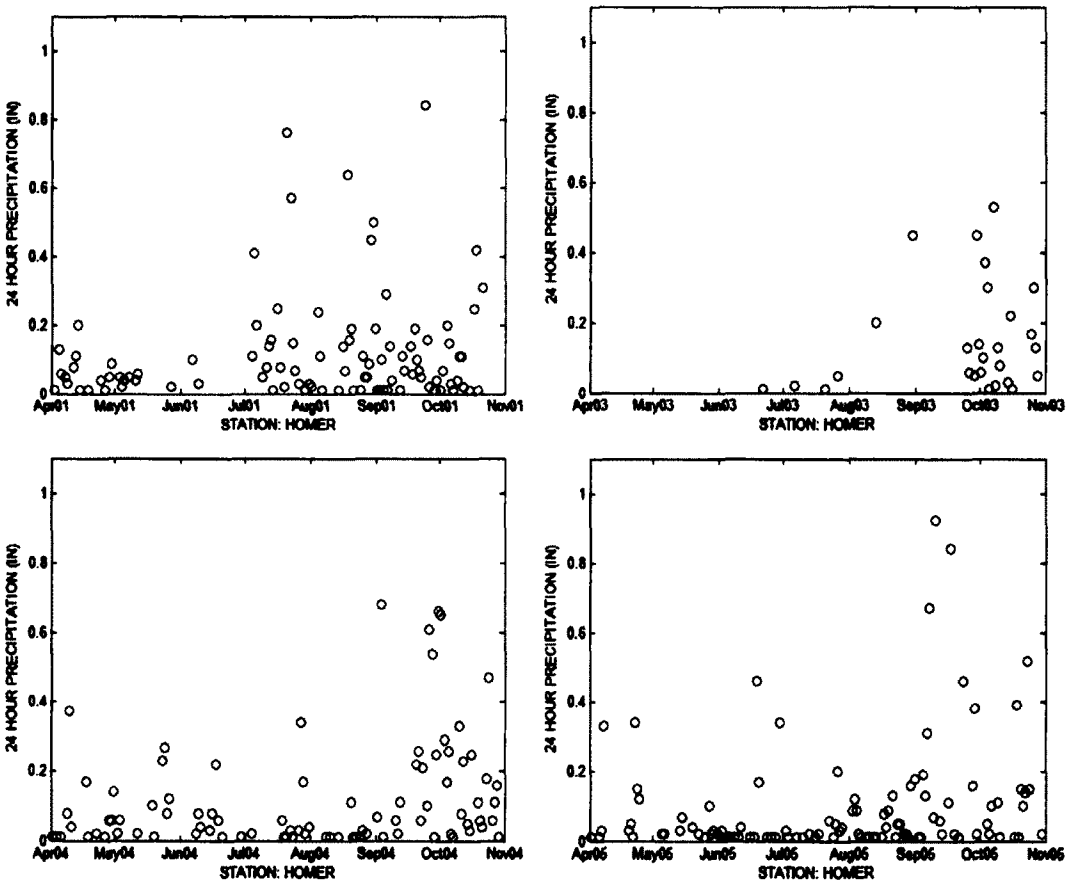
24 HOUR PRECIPITATION (IN)
0
0.2
0.4
0.6
0.8
1
Apr01 May01 Jun01 Jul01 Aug01 Sep01 Oct01 Nov01
STATION: HOMER
24 HOUR PRECIPITATION (IN)
Apr03 May03 Jun03 Jul03 Aug03 Sep03 Oct03 Nov03
STATION: HOMER
24 HOUR PRECIPITATION (IN)
Apr04 May04 Jun04 Jul04 Aug04 Sep04 Oct04 Nov04
STATION: HOMER
24 HOUR PRECIPITATION (IN)
Apr05 May05 Jun05 Jul05 Aug05 Sep05 Oct05 Nov05
STATION: HOMER

Figure A1 continued

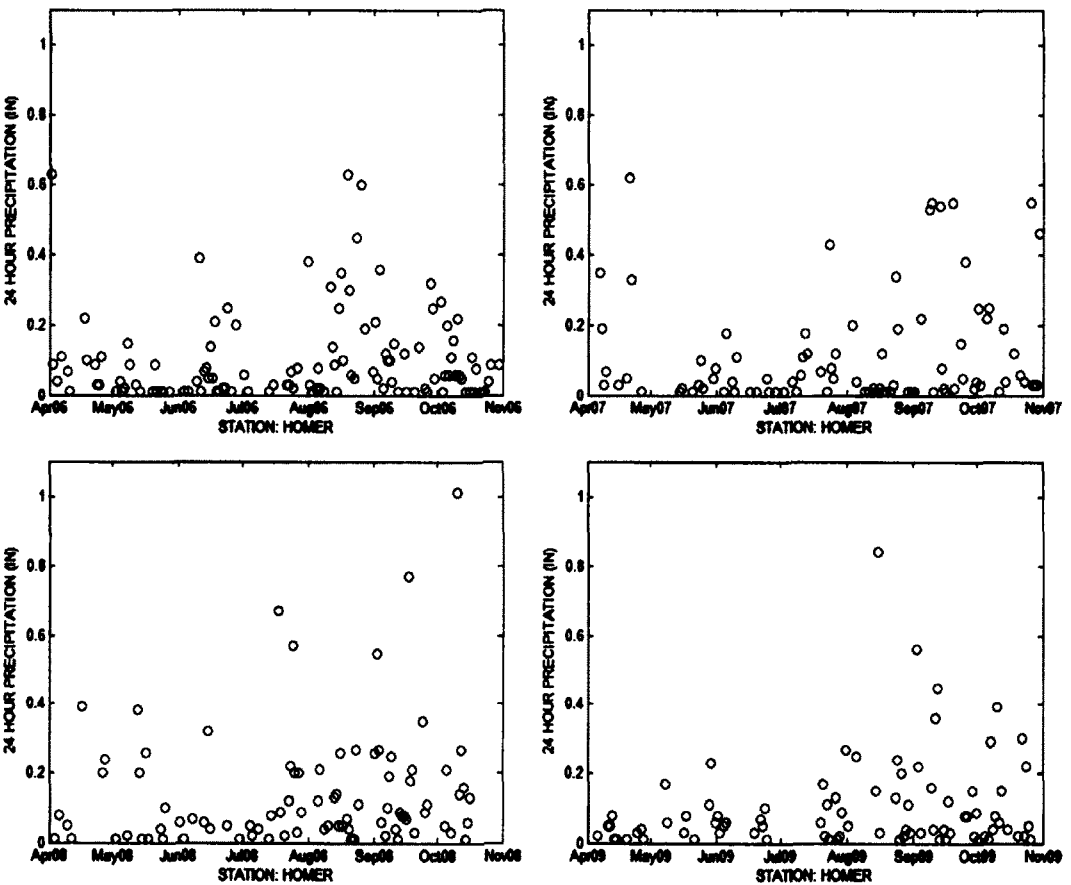
24 HOUR PRECIPITATION (IN)
0
0.2
0.4
0.6
0.8
1
Apr06 May06 Jun06 Jul06 Aug06 Sep06 Oct06 Nov06
STATION: HOMER
24 HOUR PRECIPITATION (IN)
Apr07 May07 Jun07 Jul07 Aug07 Sep07 Oct07 Nov07
STATION: HOMER
24 HOUR PRECIPITATION (IN)
Apr08 May08 Jun08 Jul08 Aug08 Sep08 Oct08 Nov08
STATION: HOMER
24 HOUR PRECIPITATION (IN)
Apr09 May09 Jun09 Jul09 Aug09 Sep09 Oct09 Nov09
STATION: HOMER

Appendix B

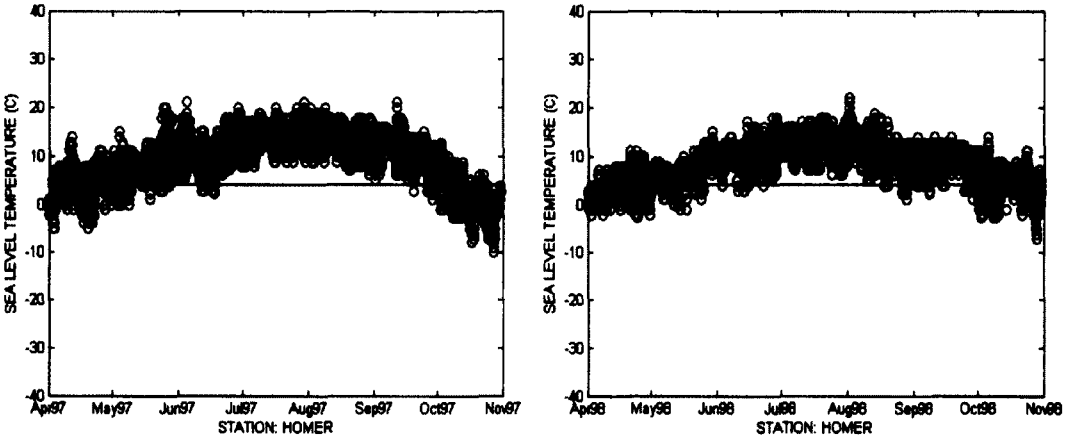

Figure B1

Temperature data from Homer, AK for 1997-2009. Data is from National Climate Data Center. Seven months data are shown for each year. (2002 is again omitted.) Daily temperatures in Celsius at a NCDC station located in Homer, AK, 112 km from Augustine Island. For the appendix all the data was taken from one station in Homer (USAF 703604); for uniformity, because no data for Augustine station (USAF 994700) are available before 2002. However, data from the Augustine station were considered when available. The line at 4°C shows the temperature plot from the perspective of the summit of Augustine, which is 4°C cooler than sea level.

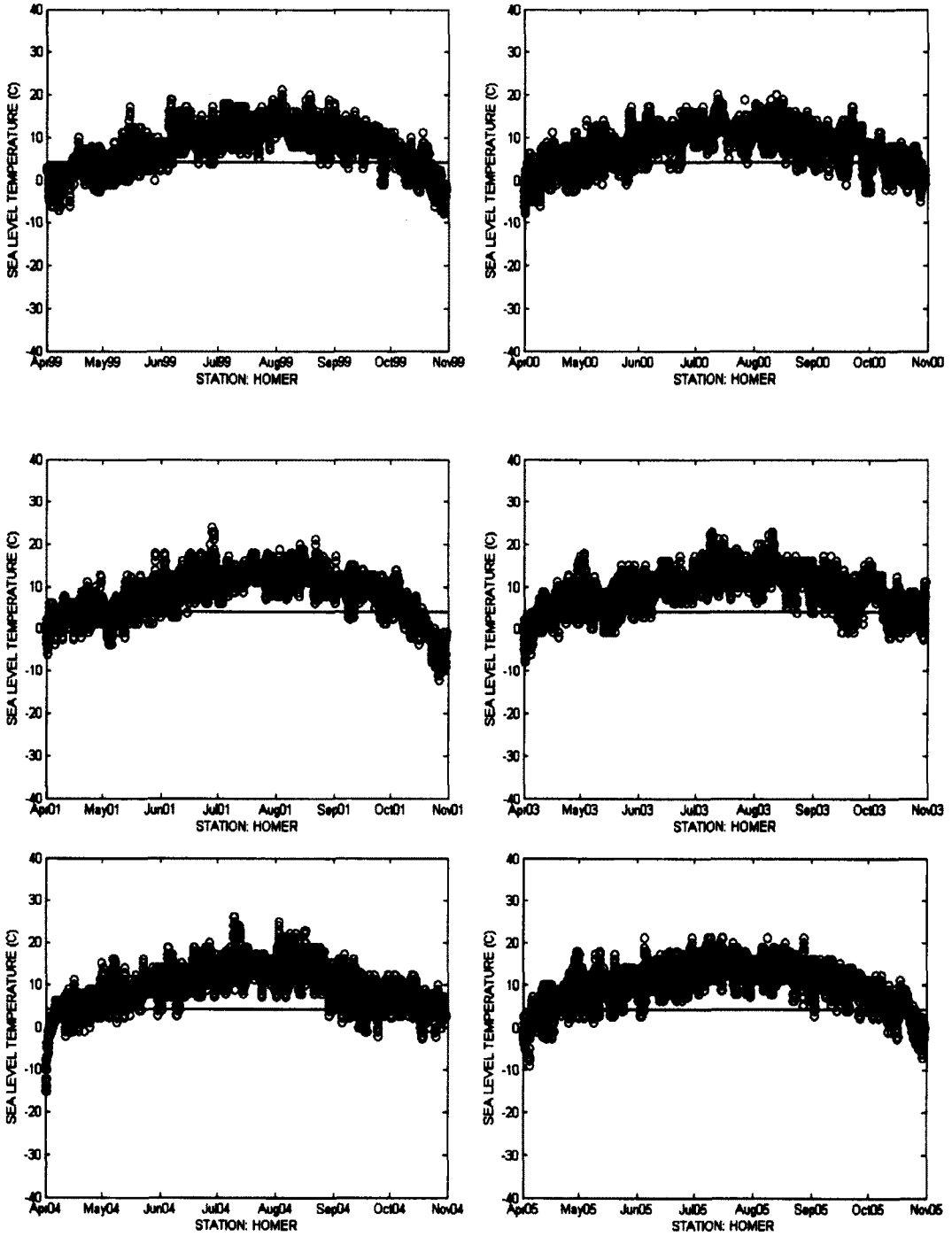

Figure B1 continued

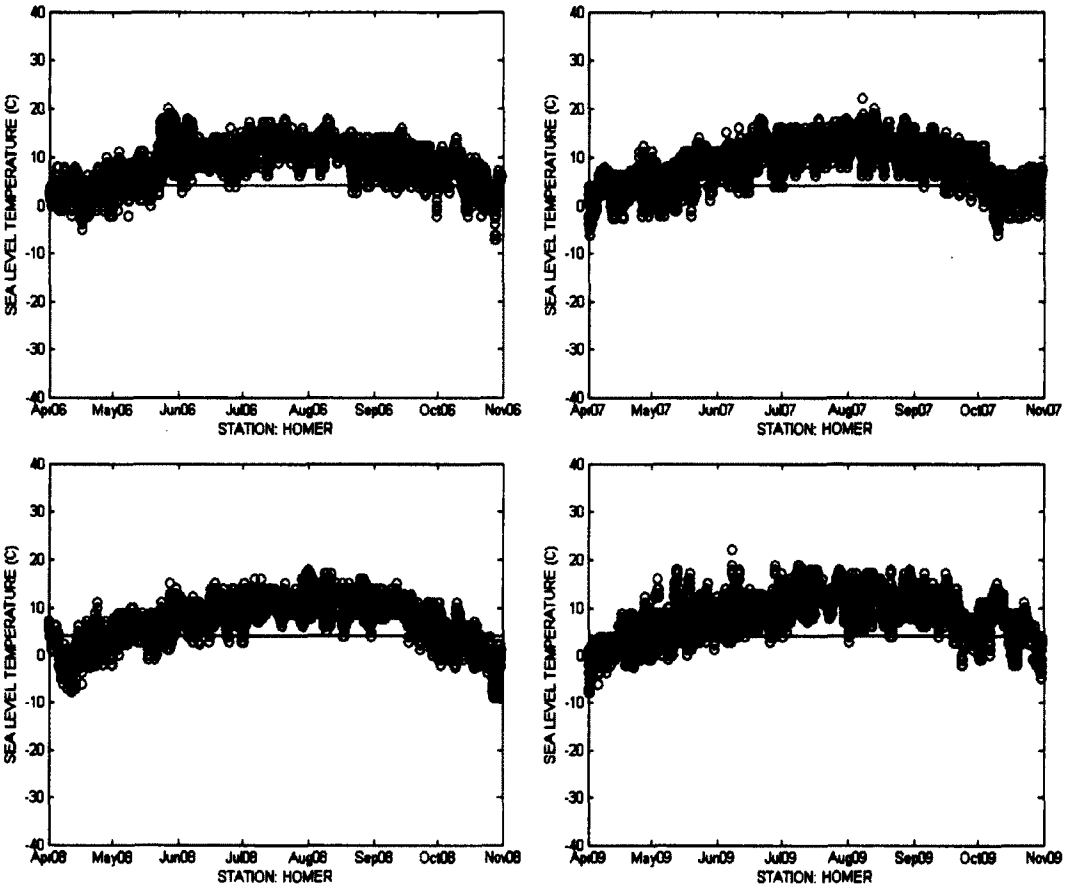

Figure B1 continued